Ministry of Energy and Water Resources
Geological Survey of Israel

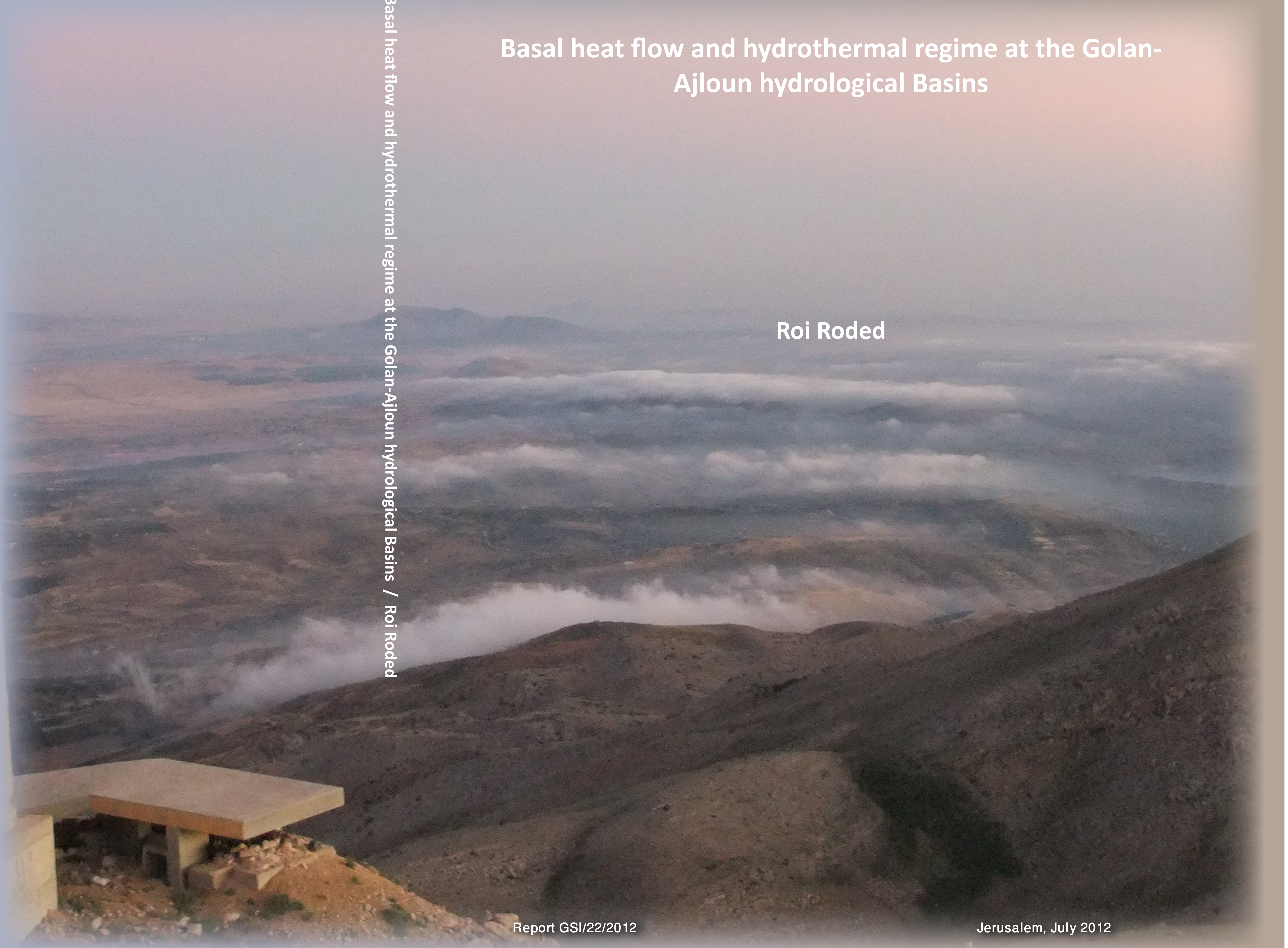

Basal heat flow and hydrothermal regime at the Golan-Ajloun hydrological Basins

Roi Roded

Report GSI/22/2012

Jerusalem, July 2012

Basal heat flow and hydrothermal regime at the Golan-Ajloun hydrological Basins / Roi Roded

©Published by the Geological Survey of Israel
30 Malkhe Israel St., Jerusalem 95501, Israel

Cover design: Nili Almog

Front cover: Golan-Heights view from Mitzpe Shlagim (Hemon Mount)

Ministry of Energy and Water Resources
Geological Survey of Israel

Basal heat flow and hydrothermal regime at the Golan-Ajloun hydrological Basins

Roi Roded

This thesis was submitted for the degree "M.Sc degree" to the senate of Ben-Gurion University of the Negev, Israel.

The study was carried out under the supervision of:
Prof. Katoshevski David, Unit of Environmental Engineering, Ben-Gurion University of the Negev, Israel
Dr. Shalev Eyal, Geological Survey of Israel

Report GSI/22/2012 Jerusalem, July 2012

Abstract

A shallow heat anomaly in the form of heated groundwater is detected in the Lower Yarmouk Gorge (LYG), where a series of thermal springs discharges, at Northern Israel and Jordan. Results of numerical simulations of groundwater flow and heat transfer, conducted for the Golan-Ajloun area, indicate that satisfying the hydrothermal field observations requires: a) existence of an exceptional source of deep geothermal heat below the Golan Heights (GH); b) existence of a few MCM/yr, deep flow path (~3 km), forced convection flow component, originating at Hermon Ridge and discharging at the LYG outlets.

This flow component serves as a fundamental heat convection component, which transports heat from great depth and significantly affects the hydrothermal pattern. This deep circulation is causing a considerable part of the basin's elevated basal heat flow to be transported to the LYG outlets, and prevents shallow thermal expression at the GH. Said flow component is expected to be small- only a few MCM/yr- compared with overall groundwater discharge through the LYG outlets (45 MCM/yr), where the main water source of the LYG outlets is the shallow flow components of Ajloun origin, as suggested by most previous hydrological studies. Model results indicate that the regional mean basal heat flow value at the GH is 100 mW/m^2, and the shallow thermal anomaly of the LYG is an expression of a deep crust geothermal anomaly.

Additional possible hydrothermal configurations, involving an eastern exceptional heat source and deep heat transportation or, alternatively, deep heat transportation that is larger by area magnitude (~3,600 km^2), including Eastern Hauran, the GH and the Ajloun Ridge under regionally average basal heat flow (50 mW/m^2). But lack of any basic geological and hydrothermal information is prevents a detailed study of those possibilities.

The combination of high temperatures at a relatively shallow depth (~130^{o}C at 3 km) and a large artesian groundwater reservoir existing below LYG may be adequate for geothermal utilization, which may also take place within the green line.

Analysis of the geothermal system of the Golan-Ajloun area indicated conclusively that deep groundwater transportation takes place. While this transport collects heat from a vast area, it constitutes a rather minor component of overall flow flux. As in other studies, analysis of heat patterns proved to be a good groundwater tracer.

The geothermal Peclet (Pe) number is found to be a good measure for rough assessment of ratio of heat transfer by the various mechanisms, but only as long as it's not relying on hydraulic conductivity estimations. The Rayleigh-Darcy (Ra) number was found to be impractical for an actual estimation of convection regimes, though the different natural convection regimes described in literature were identified in model scenarios.

COMSOL multyphysics commercial software package was tested, and was found to be inadequate for numerical analysis of basin-scale geothermal systems, while the FEFLOW software package, as indicated in previous studies, exemplified greater stability and solution consistency throughout all work stages.

Acknowledgments

I wish to thank my supervisors: Eyal Shalev and David Katoshevski. Additionally I would like to thank for: Avihu Burg, Vladimir Lyakhovsky, Dubi Levitte, Stuart Wollman, Zvi Ben-Avraham from Tel-Aviv University, Roee Orland from Ben-Gurion University, and Amos Bein for fruitful discussions.

CONTENTS

LIST OF FIGURES

LIST OF TABLES

Table 1. Nomenclature

A	GH-Ajloun estimated involved deep convection area, km^2	$\delta^{18}O$	Measure of the ratio of oxygen stable isotopes- ^{18}O:^{16}O, 1
$\bar{a}$	Anisotropy factor of thermal conductivity, 1	θ	Porosity, void space, 1
c (c_v), c_p	Specific heat capacity at constant volume and at constant pressure, respectively. m^2 sec^{-2} ^{o}C^{-1}	θ^s	Volume fraction of solid phase, 1
D_m	Tensor of mechanical dispersion, m^2 sec^{-1}	λ	Thermal conductivity, kg m sec^{-3} ^{o}C^{-1}
E, E^s	Internal (thermal) energy density of fluid and solid phases, respectively, m^2 sec^{-2}	λ_c	Conductive part of the thermodispersion tensor, kg m sec^{-3} ^{o}C^{-1}
g	Gravitational acceleration, m sec^{-2}	λ_m	Mechanical part of the thermodispersion tensor, kg m sec^{-3} ^{o}C^{-1}
H_e,H_e^s	Energy (heat) sink/source term of fluid and solid phases, respectively, kg m^{-1} sec^{-3}	λ_{td}	Hydrodynamic thermodispersion tensor, kg m sec^{-3} ^{o}C^{-1}
h	Hydraulic head, m	λ□, $\lambda^{\perp}$	Thermal conductivity parallel and normal to bedding, respectively. kg m sec^{-3} ^{o}C^{-1}
I	Unit tensor, 1	μ	Dynamic viscosity, kg m^{-1} sec^{-1}
J	Average Basal Heat flow below GH-Ajloun area, kg sec^{-3}	ρ	Density function, kg m^{-3}
j, j^s	Non-advective heat flux of fluid and solid phases, respectively, kg sec^{-3}	ρ_r	Relative density, 1
K	Hydraulic conductivity, m sec^{-1}	Y	Coefficient of skeleton compressibility, m^{-1} or kg^{-1} m sec^2
k	Porous medium permeability tensor, m^2	υ	Specific volume 1/ρ, kg^{-1} m^3
L	Characteristic flow path length, m	ψ	Stream function, m^2 sec^{-1}
p	Pressure, kg m^{-1} sec^{-2}	***Subscripts***	
Pe	Peclet number	0	Reference
Q	Mass Sink/source term, kg m^{-3} sec^{-1}	$1,2,3.$	Boundariy Γ section index
Q_{EB}	Extended Boussinesq approximation term (head related), sec^{-1}	i	Vector component index
Q_T	Historical discharge of the LYG springs, m^3 sec^{-1}	n	Normal
q	Darcy velocity, m sec^{-1}	RT	Room temperature
Ra, Ra_{c1}, Ra_{c2}	Rayleigh number, critical 1 and 2	***Superscripts***	
Re	Porous medium Reynolds number	s	Solid phase
S	Specific storage coefficient, m^{-1}	R	Value on boundary
T	Temperature in Celsius, ^{o}C	***Abbreviations***	
t	Time, sec	DST	Dead Sea Transform
U	Thermal energy released by the LYG springs, kg m^2 sec^{-3}	EOS	Equation Of State
v	Macroscopic phase (pore) velocity, m sec^{-1}	FEM	Finite Element Method
$\|\|v\|\|$	Magnitude of vector v , m sec^{-1}	Fm.	Formation
x	Horizontal coordinate, m	GH	Golan Heights
z	Vertical coordinate, m	Gr.	Group
Z	Characteristic vertical length, m	LYG	Lower Yarmouk Gorge
Greek		MCM	Milion cubic meter, m3
β	Thermal expansion constant, ^{o}C^{-1}	OB	Oberbeck–Boussinesq approximation
β_L, β_T	Longitudinal and transverse dispersivity, Respectively, m	REV	Representative Elementary Volume
Γ	Boundary	TD	Total Depth
γ	Fluid compressibility , m^{-1} or kg^{-1} m sec^2	TDS	Total dissolved solids
Δ	Increment or difference		

1. Introduction

The shallow heat anomaly of the Lower Yarmouk Gorge (LYG), in Northern Israel and Jordan (see Fig.1), makes that area a place for potential production of electricity in the conventional geothermal method. In addition, knowledge concerning the deep (few km down the crust) geothermal state may provide useful insight into deep geodynamics processes, specifically in the Western part of the recent volcanically-active Harrat-Ash-Shaam Field and in the vicinity of the tectonically active Dead Sea Transform (DST).

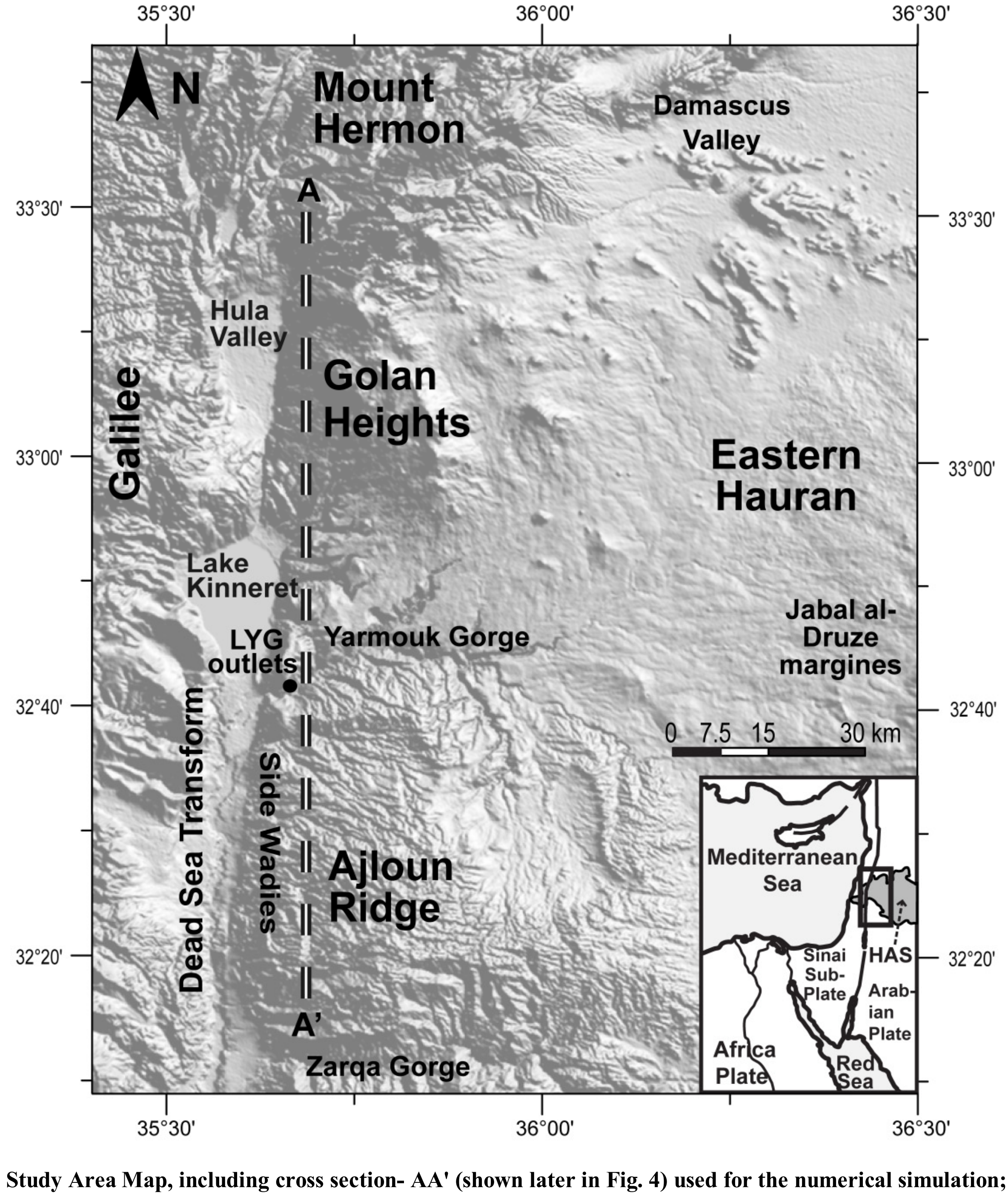

Figure 1. Study Area Map, including cross section- AA' (shown later in Fig. 4) used for the numerical simulation; HAS- Harrat-Ash Shaam-volcanic field.

The hot springs at the LYG are grouped in two areas, Hammat Gader and Mukhebeh Springs, about 2 km apart. Prior to pumping, these springs had a large primary outflow estimated at 45.5 MCM/yr (Levitte et al., 1978). In the early 1980's, a series of wells that were drilled within the LYG from both sides of the border revealed artesian pressures and high temperatures at relatively shallow depth (e.g. in the Mezar-1 well, a temperature of 79.2°C was recorded at a depth of 1,230 m; Michelson, 1981).

Previous studies considered mainly geochemical and hydrological aspects of the springs (Arad and Bein, 1986; Arad et al., 1986; Bajjali et al., 1997; Eckstein, 1976; El-Naser, 1991; Levitte and Eckstein, 1978; Mazor et al., 1973, 1980; Starinsky et al., 1979), most of them invoke a mixture of a cold-fresh component of shallow origin and more salty hot groundwater of deep origin. However, the magnitude, temperature, flow path and source of heat of the deep, high temperature component remained unknown.

In the present study the geothermal state of the Golan-Ajloun region is examined using a computational analysis for groundwater flow and heat transfer. In the framework of the present study a 2-D scheme is employed, with a cross section from Hermon Ridge Southeastern Slopes to Wadi Zarqa Gorge (North Jordan) that includes the geological section down to Triassic strata.

The source of the shallow heat anomaly at the LYG is being examined with several representative scenarios. Two hypotheses were considered: 1) the encountered heat is related to hydrological conditions and significant transportation of heat. 2) The encountered heat is of magmatic origin or due to deep crust conditions (exceptional source of geothermal heat).

2. Geological and hydrothermal settings

2.1. Geological settings

2.1.1. Tectonics and structure

The Golan Heights (GH) is a vast sedimentary syncline covered by Plio-Pleistocene basalts that erupted mainly from volcanic cones located in the eastern part of the GH, and created an elevated plateau (Mor, 1993). The GH comprises the western continuation of an extensive Jebel Al-Druze region- a broad and flat volcanic province that extends eastward into Syria and is a part of the Harrat-Ash-Shaam Volcanic-field. The GH Plateau lies between the large anticline structures of the Hermon in north and the Ajloun in the south. Westward, the GH is bounded by the Dead Sea Transform (DST) (Hirsch et al., 2002; Meiler et al., 2011).

The Hermon Ridge (2,814 m) is a long, continuous anticline. Its axis is in the NE-SW direction. It constitutes the south-western continuation of the Palmyra transpressive Fold-belt (Picard, 1943), as well as the right bend of the DST (Freund, 1965; 1980).The ridge is a complex structure comprising of intensive internal deformation, including faults and folds; the faults are mostly strike-slip faults in NNE-SSW to E-W directions, and the major faults are Serjaya and Rechaya (Fig. 2) (Heimann et al., 1990). The Ajloun Ridge (1,239 m) is a dome-shaped structure, consisting of structural basement high, that plunges in a northern direction from the Amman area to the Yarmouk River, and further in a NNE direction into Syria. It's characterized by intensive faulting, and its Northern area features a gentle undulation (Hirsch et al., 2002). Northern to the Ajloun Ridge flanks is located a major tectonic feature- the Ramtha-Wadi Sirhan (Sirhan) strike-slip Fault. The Sirhan Fault begins in Saudi Arabia and continues north western to the Ramtha area where its exact point of termination is unknown. The fault related structural configuration is of hydrological importance (see section 2.3) (Bein et al., 2003).

The GH and the Ajloun Ridge are bounded by the DST to the west. The DST is an active plate boundary separating the Arabian Plate to the east from the African Plate (Sinai sub-Plate) to the west (Freund, 1965; Garfunkel et al., 1981). In the South, the DST is a weak transtensional fault with a fairly established ~100 km left-lateral offset (Bartov, 1974; Garfunkel et al., 1981; Freund et al., 1970; Quennell, 1958). The central section of the DST, from the north -western part of the Hulla Valley along the Lebanese segment, consists primarily of a broad restraining bend where the deformation is distributed among several major strike-slip faults- Serjaya, Rechaya, Hasbaya, Yammunne and Roum. (Walley, 1988, 1998). The main strike-slip fault plane of the DST is accompanied throughout by secondary structures such as the Sea of Galilee and Hulla Valley pull apart.

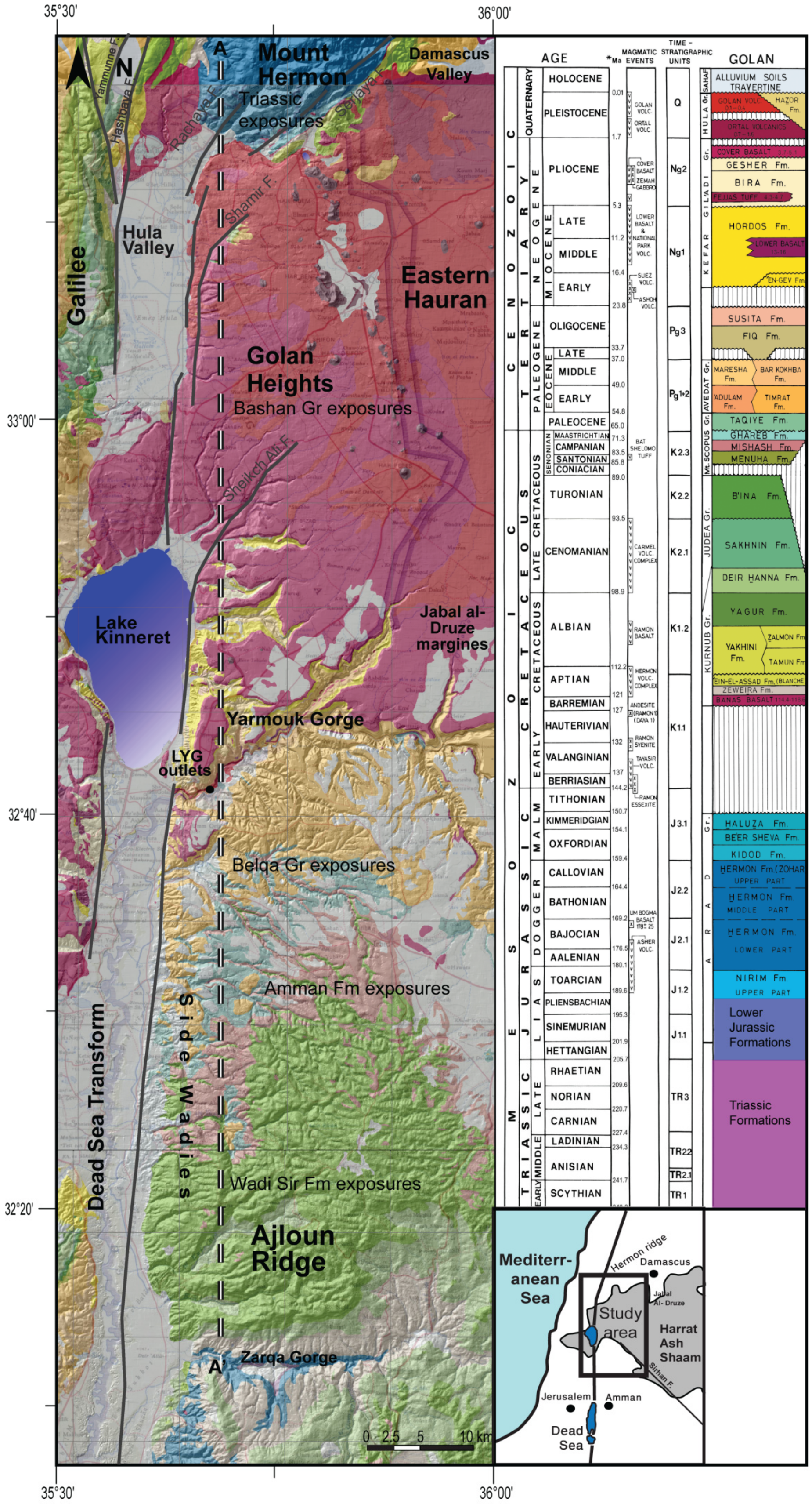

Figure 2. Geological map of study area and stratigraphic table of the GH (Sneh et al., 1998; Fleischer, 2002). Cross section- AA' (Fig. 4), used for the numerical simulation.

The underlying geological structure of the GH and the pre-basaltic strata is mostly enclosed and obscured by the Paleocene-Pleistocene basaltic outflows. Structural studies relying on seismic interpretations, combined with well and surface exposure data (Hirsch et al., 2002; Meiler et al., 2011), allow study of the buried geological structure of the GH, and have confirmed that the GH Plateau covers the large structural depression that constitutes the northern and the deeper part of the extensive Irbid–Golan Syncline that evolved during the Late Cretaceous–Cenozoic. The syncline is delineated by the gentle northward dipping of the Cretaceous and Eocene beds forming the Ajloun Anticline, and by the steep south-eastern dip of the Jurassic sequence exposed on the Hermon Ridge Anticline, which shapes the Irbid–Golan Basin into an asymmetric syncline (Figs. 3 & 4) (Hirsch et al., 2002; Meiler, 2011; Meiler et al., 2011).

The sedimentary succession accumulated within the Golan Depression extends from Late Proterozoic (above the Precambrian basement), attaining a cumulative thickness of at least 8.5 km in the northern part of the plateau. The thickness of the stratigraphic units generally varies by tens to several hundreds of meters. The major exception is the Jurassic succession, which thickens dramatically from ~700 m at the Yarmouk River area in the south to more than 3 km at the foothills of the Hermon Ridge in the north, and is associated with the Sheikh-Ali Deformation-zone. The Senonian-Cenozoic succession present as 1.5-2 km of deposits, said deposition occurring in a structural environment strongly affected by the "Syrian Arc" folding activity and the uplifting of the Hermon Ridge. The thickness of the Plio-Pleistocene basalt cover ranges from tens of meters in the Southern GH, to several hundred meters in the Northern and Central GH (Meiler, 2011; Meiler et al., 2011).

In contrast to its almost undeformed basalt cover, the interior of the GH underlying it is a highly faulted and deformed plateau, which was subject to continuous deformation phases throughout the Paleozoic-Cenozoic. Two pronounced DST related strands penetrate the subsurface of the GH. The Sheikh-Ali Fault, associated on the surface with the eastern boundary fault of the Sea of Galilee, is a major deformation zone penetrating far into the plateau. Further north, another DST strand penetrates into the GH- Shamir Fault. Shamir Fault comprises the eastern marginal fault of the Hulla Rhomb-shaped graben and related to the uplift of the "Shamir Window", from that surface expression, in the subsurface the fault continues eastward as far as 3 km. Northward, towards Hermon Ridge's foothills, an additional two main related DST strands are Kfar Szold and Azaz Faults. The Azaz Fault later becomes Rechaya Fault (Heimann et al., 1990). The Sheikh-Ali and Shamir DST strands penetrate for a considerable distance into the subsurface of the GH Plateau together with the various styles of deformations observable along them, indicating the structural complexity which evolved next to the location of divegence of the DST, where the main fault diverges into five different segments (Hirsch et al., 2002; Meiler, 2011; Meiler et al., 2011).

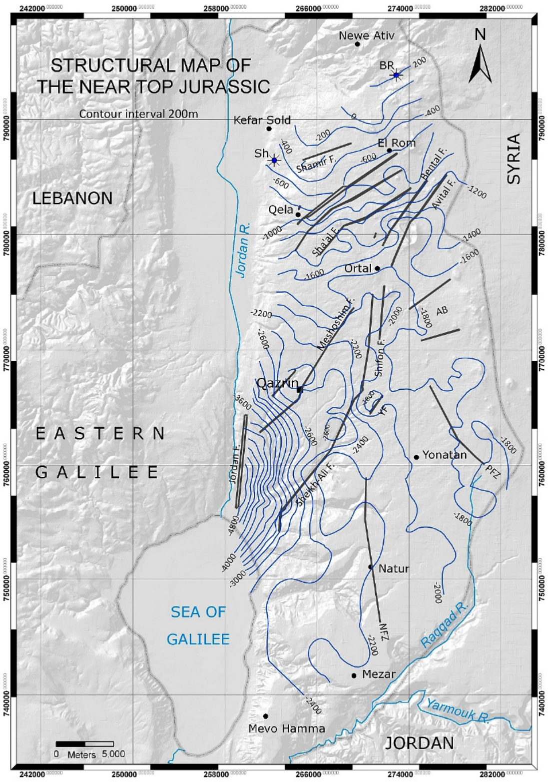

Figure 3. Structural map of the near top Jurassic (Meiler et al., 2011).

East to the GH there is no remarkable geological boundary. The Damascus Basin and the deep structure of Jebel Al-Druze are defined as the east geological boundary of the GH. Jebel Al-Druze Depression is a north westerly trending and possibly a DST related basin. On the surface, the depression is covered by basaltic flows reaching a maximum thickness of approximately 1,500 m. in the Jebel Al-Druze- a volcanic ridge rising up to 1,800 m in the axial zone of the depression. According to drilling data, the base of the basaltic pile beneath the ridge is at 100 m above sea level, i.e. 400 m deeper than at the basaltic plateau margins (Galaktonov, 1989). The basement depth in the Drouz depression is about 7 km or more (Brew et al., 1997; S.P.C., 1986), suggesting that the depression is filled by a thick sequence of Paleogene, Cretaceous and possibly older sediments (Ponikarov, 1967).

2.1.2. Stratigraphy and model units

The exposed geological section in the Hermon-Ajloun region contains a thick sequence from the upper Triassic to the Pleistocene age (Fig. 2 and Table 2). The Triassic to Eocene age are exposed at Hermon Ridge, Northern GH and at the Ajloun Ridge. At the GH area Paleocene-Pleistocene basaltic outflows mostly enclose and obscure the pre-basaltic strata.

According to stratigraphic studies (Hirsch et al., 2002; Michelson, 1982) the sedimentary sequence beneath the Golan-Ajloun area is characterized by sharp facial changes and large thinning of the section at the transition from Northern GH to North Jordan. Exceptionally pronounced thickening is evident in the early Jurassic section appearing north to the Sheikh-Ali deformation zone (Meiler et al., 2011). In addition to the facial changes and thickening a significant erosion event dated to the lower Cretaceous truncated several formations. Kidod and Sa'ar formations appear in the Hermon margins and extend somewhere between North GH and Zarqa Stream, presumably north to the Yarmouk. Eastern to the GH and North Jordan the Jurassic section is completely missing and Cretaceous units lie directly on Triassic rocks (Hirsch et al., 2002). The apparent absence of the clayey Kidod Fm. beneath the lower Yarmouk is of hydrological and geothermal importance since that configuration allows for hypothetical hot groundwater ascent from deeper horizons to the surface in that area. Northward, The Jurassic section at the Hermon Ridge and Northern GH is characterized by developed karst.

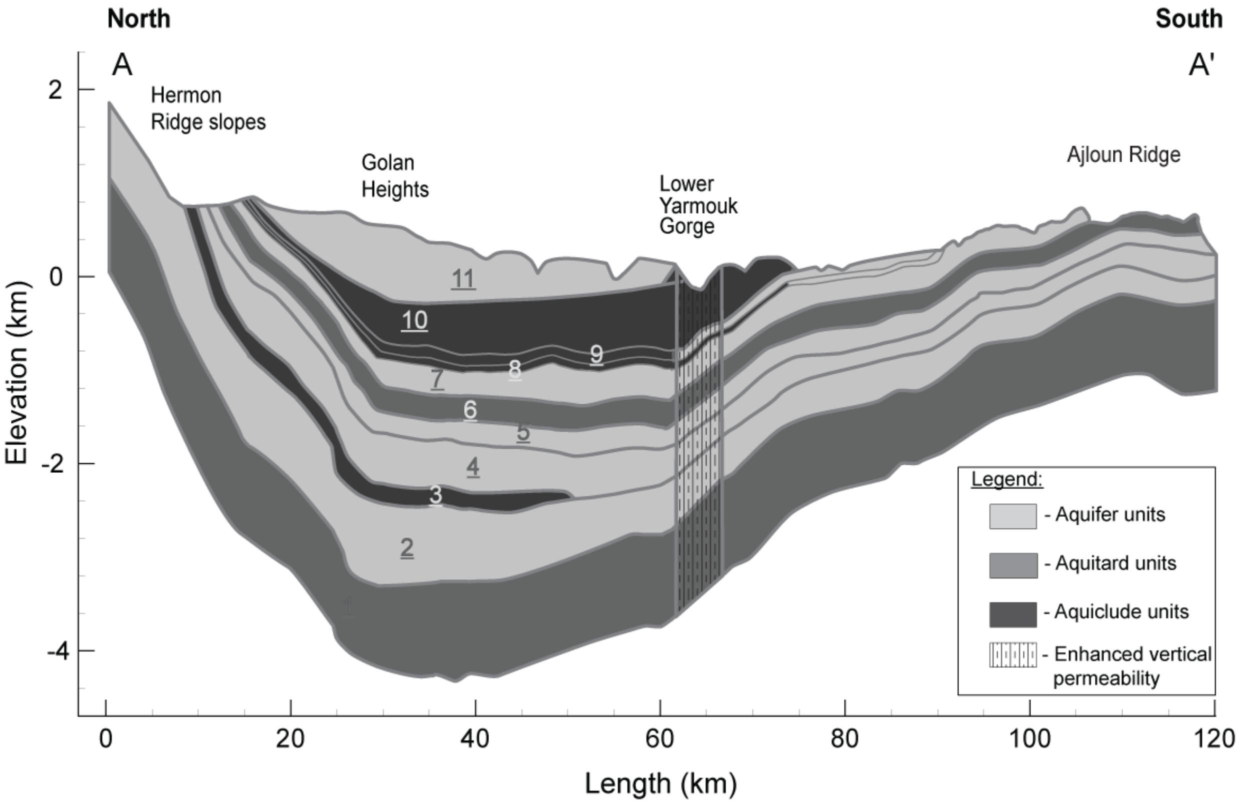

Figure 4. Cross section from the slopes of the Hermon Ridge to Ajloun Ridge (AA' in Figs.1 and 2). Numbers indicating model units (Table 2), shades marking aquifer, aquitard and aquiclude units; cross section is based on Michelson (1983).

Due to the extensive strata facial variations (Table 2) different hydraulic and thermal parameters were assigned to different units, typically divided into northern and southern. The division is meant for modeling purposes and sometime does not coincident with the usual stratigraphic order, i.e. occasionally formations that are not age-equivalent were bounded under one model unit or model units may contain one or several formations, sometimes from different groups.

Table 2- Units model division and stratigraphy; Based on: 1- Bandel and Khoury (1981); 2- Sneh (1998); the rest is modified from Bein et al (2003).

	North				**South**			
unit no.	**Age**	**Lithostratigraphic units**	**Lithological description and estimated permeability.**	**Thick-ness (m)**	**Age**	**Lithostratigraphic units**	**Lithological description and estimated permeability.**	**Thick-ness (m)**
	Upper Triassic	Rimeh (J1) Fm	Dolomite, limestone and some volcanics, aquitard.	1000	Triassic	Triassic sequence, includes 9 Fm[1]	Sedimentary sequence, highly heterogeneous, includes carbonates, clastics and evaporates, Aquitard.	1000
	Lower Jurassic	Arne Fm						
	Middle Jurassic	Kalat Jandal (J2), Beqassem (J3) Fm[1]						
2	Middle Jurassic	Hermon (J4) Fm	Massive and karstic limestone and dolomite, aquifer.	950	Lower-middle Jurassic	Hihi, Nimr, Silal, Dhahab, Hamam, Ramla, Mughanniyya Fm	Heterogenic mainly carbonates and some sands and shales , aquitard.	315
3	Upper Jurassic	Kidod (J5) Fm	Shales and marly limestone stratified thinly, aquiclude.	155-200	-	-	-	-
4	Upper Jurassic	Nhal Saar (J6/7) Fm	limestone, marl, volcanics, sands, aquitard.	720	Lower Cretaceous	Kurnub Gr	Sandy-marly, with conglomerate at the base, Aquifer.	200
	Lower Cretaceous	Tyasir volcanics, Hatira Fm, Galil Gr						
5	Lower-upper Cretaceous	Yagur Fm	Massive dolomite and limestone and marl beds, Aquifer.	150	Lower-upper Cretaceous	Naur (A1-2) Fm	Limestone, dolomite and marl, aquifer.	150
6	upper Cretaceous	Dir-Hanna Fm	Interchanges of thin dolomite, limestone and chalk beds, aquitard.	400	upper Cretaceous	Fuheis (A3), Hummar (A4), Shueib (A5-6) Fm	Mainly limestone, dolomite and marl, aquitard.	250
7	upper Cretaceous	Sakhnin, Bina Fm	Karstic dolomite and Limestone, aquifer.	210	upper Cretaceous	Wadi sir (A7) Fm	Limestone with chert lenses, good aquifer.	200
8	Upper Cretaceous	Menuha Fm	Chalk, marl and limestone, aquiclude	50	upper Cretaceous	Wadi Ghudran (B1) Fm	North to latitude 210 contain chalk, marl and limestone, aquiclude. South to latitude 210 contain limestone, aquifer.	50
9	Upper Cretaceous	Meishash Fm	Limestone with chert and phospharite, aquiclude..	100	upper Cretaceous	Amman (B2) Fm	Limestone with chert and phosphorite, aquifer.	100
10	Upper Cretaceous-Neogene	The rest of Mount Scopus, Avdat Gr, Susita, Fiq, Hordos, Gesher, Bira Fm[2]	Mainly Chalk some marl, phospharite limestone, chert, aquiclude, some perched aquifers.	850	upper Cretaceous-Paleocene	The rest of Belqa Gr	Mainly chalk, some marl, limestone aquiclude, some perched aquifers.	450
11	Pliocene-Pleistocene	Bashan Gr[2]	Basalts	several hundreds	-	-	-	-

2.2. Geothermal background and settings

2.2.1. Literature review

Geothermal research in Israel and the surrounding area

Extensive geothermal surveys in the area of the state of Israel (Eckstein and Simmon, 1978; Levitte and Olshina, 1985; Shalev et al., 2008) have concluded a mean heat flow value of ~45 mW/m^2. Those determinations included measurements of thermal conductivities though analysis of core and loose sediment samples, and temperature gradient measurements in a series of abandoned deep oil and water wells at depths of several hundred to several thousands of meters.

In Jordan, east to Israel, Galanis et al. (1986) either estimated or calculated (depending on which well) heat flow values at 18 sites. They concluded the existence of two areas of heat anomalies; the first, adjacent to the DST near Zarqa Ma'in and Zara, averages heat flow of 133 mW/m^2; and the second, adjacent to Azraq Basin, with heat flow ranging from 70 to 135 mW/m^2. In the rest of the country they estimated a mean heat flow value of 53 mW/m^2 and claimed that it represented the regional "background" heat flow. Somewhat in contrast, Förster et al. (2007, 2010) argued, based on heat-flow measurements in southern Jordan and analysis of samples down to the lithospheric mantle underneath Jordan, for a mean basal heat-flow value of ~60mWm^2. Accordingly, this value is representative for the late Proterozoic-consolidated Arabian Shield, and contradicts the common view of it as a low basal heat-flow province of ~45 mW/m^2. Values mentioned above are higher than the value reported by Erickson et al. (1977) for the Eastern Mediterranean- averaging 31±12.6 mW/m^2, and much lower than the values prevailing in the whole of the Red Sea region, where heat flow was estimated to be 467±116 mW/m^2 over the axial region (Girdler and Evans, 1977).

The relatively low heat flow detected for Israel (Eckstein and Simmon, 1978; Levitte and Olshina, 1985; Shalev et al., 2008) prevails also in the Dead Sea Rift Valley, where elevated heat flow is expected (Mckenzie, 1978). However, no thinning of the lithosphere is evident along the DST (Folkman, 1980) and hence no elevated heat flow is expected. In addition Feinstein (1985) concluded, based on coal-rank measurements and time-temperature-coalification calculations in the Ami'az-I and adjacent boreholes that the same low thermal regime (i.e. 20-23^{o}C/km) has prevailed at least since the Miocene, hence throughout the evolution of the basin.

Geothermal research at the Golan-Ajloun Basin and its surroundings

In the late 1970's, the Institute of Petroleum Research and Geophysics conducted several extensive geothermal explorations of different regions by electrical mapping. Survey results that included areas around Sea of Galilee were negative or inconclusive (Rotstein et al., 1977). Keller, who visited the Institute of Petroleum Research and Geophysics, concluded that the explorations were incomplete, and suggested further exploration and analysis, especially in the GH area (Keller, 1977). However, an additional survey (Rotstein et al., 1978) performed in the vicinity of the volcanic extrusions at the GH, concluded that the area is cold and there is no apparent residual heat.

Vast geochemical explorations were performed on groundwater at the LYG (Arad et al., 1986; Arad and Bein, 1986; Bajjali et al., 1996; Eckstein, 1976; Levitte and Eckstein, 1978; Mazor et al., 1973, 1980; Starinsky et al., 1979). Most of these invoked a mixture of cold-fresh component of shallow origin, and a hot, more salty component of deep origin. However, the magnitude, flow path, temperature and source of heat of the deep hot component remained unknown. The findings of more recent work will be reviewed:

Arad et al. (1986) conducted a hydrochemical study of some trace and minor element composition of groundwater resources in Israel. The Hammat Gader-Mezar system showed geochemical correlation with some geothermal systems in Western U.S, and appears in an area of geothermal gradient larger by a factor of two than the gradient found anywhere else in Israel. Arad and Bein (1986) found very good correlation between $\delta^{18}O$ and temperature in Mezar wells and Hammat Gader Springs, indicating that the higher the temperature the more negative the $\delta^{18}O$ ratio. According to the authors it appears that the observed $\delta^{18}O$-temperature correlation represents a mixing line between two components, a hot and light and cooler and heavier one. They also claimed that the light composition corresponded to values for the Northern GH and the Jordan sources originating at Hermon Ridge, and suggested that a flow component from Hermon Ridge and Northern GH towards the LYG creates deep circulation that might explain the encountered heat at the LYG Springs and wells; however, the authors concluded that considering all the data it is most likely that a higher than normal geothermal gradient extends over parts of the GH related to volcanic activity.

Bajjali et al. (1997), similarly to Arad and Bein (1986), found very isotopically-depleted hot groundwater (in Maqla Spring and JRV1 well on the Jordanian side) but accordingly this hot groundwater recharge occurs in the upper reaches of the Ajloun Highlands and not at the Hermon or Northern GH, and groundwater flow occur in the A1-A6 strata (A1-A7 are the Ajloun Gr. units equivalent to the Israeli Judea Gr.). They also proposed that the elevated temperatures of all groundwater on the Jordanian side of the LYG (30 to 54°C) can be attributed to heating along a local geothermal gradient of 2.5°C per 100 m. Departures from this gradient are due to vertical flow in fault zones and possibly to the local influence of an intrusion.

Ben-Avraham et al. (1978) measured a relatively high mean heat flow of 75 mW/m^2 (range from 70 to 80 mW/m^2) in Sea of Galilee using a special probe designed for determination of heat flow in lakes.

They estimated measurement error to be less than 20%. Levitte and Olshina (1985) analyzed temperature data from oil and water wells. Based on measurements of temperatures from Mezar 1, Jordan 1 and 2, Rosh Pina and Kinneret 6 wells among others, they claimed the existence of a heat anomaly in the area of Sea of Galilee -Golan, which is consistent with depth and indicates a deep-seated heat source. Bein and Feinstein (1988) calculated historical geothermal gradients from coalification profiles measured in the DST. The time-temperature calculations that the authors conducted revealed that in order to produce the coalification recorded in the Notera-3 borehole, located at Hulla Valley, an average thermal gradient of approx. 38 - 42°C/km must have existed in the Hulla Valley since the mid-Miocene. They indicated that the mid-Miocene thermal regime in the Hulla Valley and probably also in the Sea of Galilee is considerably higher than that recorded in the Dead Sea Basin. The authors suggested that the mid-Miocene higher thermal regime in the two Northern Basins related to the Golan-Jebel Al-Druze volcanic belt which is apparently not related to crustal thinning in rhomb-shaped grabens or other deep geodynamic processes in the transform system.

Temperature gradient measurements (Levitte and Olshina, 1985) at the previously-discussed deep Notera 3 well (TD-2,786), suggest that currently a low thermal regime prevails in Hulla Valley (when compared with the mid-Miocene elevated thermal regime). Also thermal data reported from the deep Zemah-1 borehole (Eckstein and Mautath, 1995) located on the Southern Shore of Sea of Galilee (approx. 8 km from Hammat Gader), indicates that a low thermal regime prevails in that area (The measurements yield a uniform geothermal gradient of 19.76± 0.01°C/km between a depth of 2,250 m to 3,470 m, and heat flow of 36.47± 1.64 mW/m^2). Summarizing all thorough measurements from the Northern section of the DST (west of the study area), it may be concluded that a relatively high basal heat flow, of 75 mW/m^2, prevails in Sea of Galilee, whereas north and south of the lake the heat flow is much lower, approximately 36 mW/m^2 (Ben-Avraham et al., 1978; Eckstein and Mautath, 1995; Levitte and Olshina, 1985).

Michelson (1983), considering thermal data from springs and wells in the LYG, estimated a gradient of 45°C/km, and suggested the existence of a geothermal anomaly in the Southern GH and that, in addition to the existence of a large groundwater reservoir, this site might be a suitable location for harnessing geothermal energy. Shalev et al. (2008) assessed the geothermal resources in Israel, and concluded that relatively high heat flow exists at the Southern end of the GH, possibly attributable to a magmatic source and groundwater upwelling. Arad Gr. in this area is predicted to have relatively high temperature and high groundwater pressure at shallow depth (<3,000 m). The permeability and porosity of Arad Gr. are high and therefore this location may be a potential geothermal site.

2.2.2. Geothermal data

Heat flow measurements at the Golan-Ajloun area are scarce, mostly since there are very few deep boreholes, where convection effects are small and reliable deep conductive basal heat flow may be calculated. Thermal data in the form of temperature measurements is more abundant and used for model setting and examination of possible scenarios.

In the Northern part, at the GH area, none of the many measured water outlets have abnormal discharge temperatures (15-23^{o}C ;Dafny et al., 2006); those also include some wells of several hundred meters in depth (Table 4). At the Ajloun Ridge two heat flow measurements at the S-18 and S-90 boreholes yield 42 and 62 mW/m^2 respectively, which does not seem to differ from the "background" heat flow. Temperature data from the Ajloun Ridge was reviewed by Bajjali (1994) who studied different hydrological aspects of thermal groundwater in North Jordan. Accordingly, most of the wells (some indicated in Table 4) and springs at the Ajloun Ridge exhibit a normal temperature gradient. Departure from such gradients is associated with convective effects, zones of large tectonic faults, and especially with junctions of intersecting faults, that serve as conduits for deep hot groundwater ascent (Abu-Ajamieh, 1980; Bender, 1974; Myslil, 1988; Truesdell, 1979). The existing geothermal and hydrothermal data concerning the Ajloun Ridge is partial, but implies that normal regional basal heat flow prevails at the Ajloun Ridge. In addition, large basalt outflows found only east and north of the ridge indicate that no significant recent volcanic activity has taken place in that area. More abundant thermal data exists at the LYG and its surroundings. This data includes historical discharging water outflow and temperatures of the springs (Table 3) and wells (Tables 4). Most data shows the existence of a shallow heat anomaly in that area.

Hammat Gader Springs' temperature seems to be stable from 1913 to 1995 (Kafri et al., 2000; Levite et al., 1978). In some of the wells at the LYG a temperature decrease is observed (Bajjali, 1994; Shalev et al., 2008) due to over-pumping.

Table 3-discharge Temperatures and historical out fluxes of Hammat Gader and Mukhebeh springs; based on: 1-Bajjali et al. (1997), 2-Levitte et al. (1978).

<table>
<tr><th>Spring group name</th><th>Spring name</th><th colspan="2">Outflow (MCM/yr)</th><th>Temperature (°C)</th></tr>
<tr><td rowspan="2">Mukhebeh</td><td>Maqla</td><td rowspan="2">22.71[2]</td><td>~40%[1]</td><td>39-43[1]</td></tr>
<tr><td>Balsam</td><td>~60%[1]</td><td>33-34[1]</td></tr>
<tr><td rowspan="5">Hammat Gader[2]</td><td>Shina</td><td colspan="2">9.43</td><td>28</td></tr>
<tr><td>Balsam</td><td colspan="2" rowspan="2">6.14</td><td>42</td></tr>
<tr><td>Bulus</td><td>25</td></tr>
<tr><td>Maqla</td><td colspan="2">4.14</td><td>50</td></tr>
<tr><td>Rieh</td><td colspan="2">3.65</td><td>37</td></tr>
</table>

Table 4- wells temperature and heat-flow data; Based on: 1-Bajjali (1994), 2-Michelson (1981), 3- Mero and Rozner (1984), heat-flow measurements from Galanis et al. (1986).

<table>
<tr><th colspan="13">Temperature data</th></tr>
<tr><th>Well name</th><th>Location area</th><th>waypoint</th><th colspan="2">Source aquifer</th><th colspan="4">Perforation or open hole intervals (depth from ground level in m)</th><th colspan="4">Water temperature (°C; D.T- drilling time temperature)</th></tr>
<tr><td>Birkat Ram 1</td><td>Northern GH</td><td>22285/29370</td><td colspan="2">Basalt</td><td colspan="4">40-295.5</td><td colspan="4">17.0</td></tr>
<tr><td>Mey Eden</td><td>Central GH</td><td>21709/26699</td><td colspan="2">Basalt</td><td colspan="4">Alternately 80-180</td><td colspan="4">21.5</td></tr>
<tr><td>Alone Habashan 4</td><td>Central GH</td><td>22980/27010</td><td colspan="2">Basalt</td><td colspan="4">291-348.5</td><td colspan="4">21.0</td></tr>
<tr><td>Alone Habashan 5</td><td>Central GH</td><td>22775/27315</td><td colspan="2">Basalt</td><td colspan="4">345-360 and 370-386</td><td colspan="4">18.1</td></tr>
<tr><td>Alone Habashan 8</td><td>Central GH</td><td>27166/22823</td><td colspan="2">Basalt</td><td colspan="4">333-369 and 379-393</td><td colspan="4">21.1</td></tr>
<tr><td>Mezar 1[2]</td><td>LYG</td><td>215450/239000</td><td colspan="2">A7</td><td>975</td><td>1170</td><td>1200</td><td>1230</td><td>68.1 (DT)</td><td>77.8 (DT)</td><td>79.0 (DT)</td><td>79.2 (DT)</td></tr>
<tr><td>Mezar 2[3]</td><td>LYG</td><td>215590/23569</td><td>-</td><td>A7</td><td colspan="2">126</td><td colspan="2">448-807, mainly 777-779</td><td colspan="2">43</td><td colspan="2">70</td></tr>
<tr><td>Mezar 3[3]</td><td>LYG</td><td>215590/23569</td><td colspan="2">B2</td><td colspan="4">80-336</td><td colspan="4">45</td></tr>
<tr><td>Mukhebeh 1[1]</td><td>LYG</td><td>216000/235000</td><td colspan="2">B2</td><td colspan="4">14-350</td><td colspan="4">32.0 (D.T)</td></tr>
<tr><td>Mukhebeh 2[1]</td><td>LYG</td><td>215950/235100</td><td colspan="2">B2</td><td colspan="4">284-488</td><td colspan="4">35.0 (D.T)</td></tr>
<tr><td>Mukhebeh 3[1]</td><td>LYG</td><td>216000/235020</td><td colspan="2">B2</td><td colspan="4">173-333</td><td colspan="4">32.4-34.0</td></tr>
<tr><td>Mukhebeh 4[1]</td><td>LYG</td><td>215980/235100</td><td colspan="2">B2/A7, A4</td><td colspan="4">220-892</td><td colspan="4">36.3</td></tr>
<tr><td>Mukhebeh 5[1]</td><td>LYG</td><td>210500/231500</td><td colspan="2">B2/A7</td><td colspan="4">549-896</td><td colspan="4">45.0 (D.T)</td></tr>
<tr><td>Mukhebeh 6[1]</td><td>LYG</td><td>215750/235150</td><td colspan="2">B2</td><td colspan="4">200-475</td><td colspan="4">38.0 (D.T)</td></tr>
<tr><td>Mukhebeh 7[1]</td><td>LYG</td><td>216950/235900</td><td colspan="2">B2</td><td colspan="4">150-500</td><td colspan="4">42.0 (D.T)</td></tr>
<tr><td>JRV1[1]</td><td>LYG</td><td>214700/234500</td><td colspan="2">B2/A7, A4, A1/2</td><td colspan="4">218-1230</td><td colspan="4">42.5 (D.T)</td></tr>
<tr><td>North Shuneh[1]</td><td>Western Ajloun escarpments</td><td>208141/224360</td><td colspan="2">B2/A7</td><td colspan="4">268-840</td><td colspan="4">56.0 (D.T)</td></tr>
<tr><td>Manshieh[1]</td><td>Western Ajloun escarpments</td><td>207700/220700</td><td colspan="2">B2/A7</td><td colspan="4">857-1150</td><td colspan="4">49.8-50</td></tr>
<tr><td>Waqas[1]</td><td>Western Ajloun escarpments</td><td>209160/216200</td><td colspan="2">B2/A7</td><td colspan="4">916-1300</td><td colspan="4">51.0 (D.T)</td></tr>
<tr><td>Abuziad[1]</td><td>Western Ajloun escarpments</td><td>208600/212200</td><td colspan="2">B2/A7</td><td colspan="4">631-1126</td><td colspan="4">51.6</td></tr>
<tr><td>Wadi Arab-1[1]</td><td>Side Wadies</td><td>211947/224188</td><td colspan="2">B2/A7</td><td colspan="4">703 (depth)</td><td colspan="4">30.6</td></tr>
<tr><td>Wadi Arab-4[1]</td><td>Side Wadies</td><td>213300/226500</td><td colspan="2">B2/A7</td><td colspan="4">750 (depth)</td><td colspan="4">28.7</td></tr>
<tr><th colspan="13">Heat-flow measurements</th></tr>
<tr><th>Well name</th><th>Location area</th><th>waypoint</th><th colspan="2">Fm</th><th colspan="2">Depth interval (m)</th><th colspan="2">Temperature gradient (°C/km)</th><th colspan="4">Heat-flow (mW/m²)</th></tr>
<tr><td>S-18</td><td>Northern Ajloun</td><td>248790/211326</td><td colspan="2">A7</td><td colspan="2">314-384</td><td colspan="2">16.62</td><td colspan="4">42</td></tr>
<tr><td>S-90</td><td>Northern Ajloun</td><td>248790/211326</td><td>A7</td><td>A3-6</td><td>30.53</td><td>62</td><td>62</td><td>30.53</td><td colspan="2">62</td><td colspan="2">62</td></tr>
</table>

2.3. Hydrological settings

The described geological structure and sequence comprise a vast regional hydrological system and, excluding the GH Basaltic-cover (unit 11 in Fig. 2 and Table 2), and the aquiclude complex beneath-Avdat and Mount Scopus groups (unit 10), it is assumed to be mostly hydraulically continuous.

The shallow hydrology of the GH was studied by Dafny et al. (2003, 2006). They found that the basaltic sequence of the GH serves as an independent aquifer. In most of the GH the basaltic sequence is bounded at its base by an aquiclude complex of Avdat and Mount Scopus groups (unit 10), and with the exclusion of limited areas in the Northernmost and Southernmost parts of the GH, may be counted as hydraulically detached from the rest of the hydrological system. The lower aquifer sequence beneath the GH is also hydraulically bounded westward by the impermeable clayey section which has filled the Dead Sea Basin. That configuration prevents significant vertical or westward leakage from the deep aquifers, whose groundwater is in all probability highly pressurized (Bein et al., 2003; TAHAL, 1989).

Excluding the basaltic aquifer, the natural groundwater outlets of the entire system are exclusively located at the LYG and southward, and include: the LYG Springs (historical discharge is 45.5 MCM/yr; Levitte et al., 1978), springs spouting out in the Side Wadies (wadies that drain the Ajloun Ridge westward to Dead Sea Valley; Fig. 5), and some springs located in the contact area of the Ajloun Ridge with the Jordan Valley filling (total historical discharge is 90 MCM/yr) (Bein et al., 2003; TAHAL, 1989).

Since the GH basaltic aquifer is detached, most of the replenishment areas of the aquifer system are assumed to be located south, at the Ajloun Ridge and east to it. The climate in the Ajloun Ridge is pronounced Mediterranean, the upper part of the ridge consists mostly of Wadi Sir Fm. and Amman Fm. exposures (units 7 and 9), which cover hundreds of square kilometers (Fig. 2), and comprise the main civilian supply aquifer in North Jordan (Bajjali et al., 1997; Hobler et al., 2001). Wadi Sir Fm. and Amman Fm. at most of the ridge comprise a joint aquifer, but become separate toward the Yarmouk, south of latitude 210, due to facial variations of Wadi Ghudran (B1) aquiclude Fm. (unit 7). Exceptions to groundwater flow in the Wadi Sir Fm. and Amman Fm. aquifers are local drainage of lower aquifer units of the Ajloun Gr. (A1-6; units 5 and 6), in Northern Wadi Zarqa slopes and along the Southern Side Wadies (Ragib and Cofrinja), and possibly deep-origin discharging water at the LYG outlets (Bein et al., 2003). In the Northern part of the ridge young rocks, belonging to the Belqa Gr. (equivalent to Avdat and Mount Scopus groups; Fig. 2), are exposed. This Gr. is composed of aquiclude and aquitard units. An aquiqlude unit (B3) is located at the bottom, and prevents replenishment of the lower units (Hobler et al., 2001), and thus their water balance may be considered separately.

An additional possible replenishment source is the Hermon Ridge where large replenishment occurs in its Jurassic karstic exposures (Fig. 2), but the question of whether there is a flow component originating in the Hermon Ridge southward to the LYG outlets is a source of great debate, with hydrological and geothermal importance. The aquifers of the Hermon discharge in springs that spout out from the ridge margins throughout its flanks, some at very large fluxes (among them Banias and Dan Springs; total discharge is 600 MCM/yr). Water balances conducted both for the Hermon and Ajloun Ridges (Kessler, 2002), showed that large hypothetical leakage from the Hermon Ridge southward to the LYG outlets may be discounted, but the uncertainty of these water balances does not allow us to confirm or discount small leakage in the magnitude of few MCM/yr. This, some 500 m higher than the LYG Springs (also considerably higher than LYG wells' hydraulic head). Replenishment to other exposed aquifer-aquitard units in the Hermon-Northern GH region (Judea, Galil Gr. and Nahal Saa'r and Hatira formations- units 4-7) is negligible since their exposures are very limited (Bein et al., 2003). Extensive replenishment of Judea Gr. exposures occurs in a long, narrow ridge rising above Damascus which discharges mostly in Fija Spring (220 MCM/yr; Lamoreaux et al., 1989), but no leakage from those exposure below the Syrian GH is known to exist.

The Ajloun Ridge tends westward to the Jordan Valley, south east toward the Azraq Depression, northward to the Yarmouk, and north east toward Syria and the Jebel Al-Druze Depression. The fall into the Azraq Depression comprises a hydrological boundary to the Amman and Wadi Sir formations' aquifers, and this boundary separates the flow to the Yarmouk and Jordan Valley from the flow to the Azraq Depression (Margane et al., 2002). A water level map of the Wadi Sir Fm. and Amman Fm. aquifers (Hobler et al., 2001) indicates two main flow components originating in the highlands of the Ajloun Ridge, westward towards the Jordan Valley, and northward- towards the LYG outlets (see Fig. 5), constituting the majority of discharging water. Also shown is a small flow component towards the LYG from the east- originating at Jebel Al-Druze in Syria (ESCWA et al., 1996). East of the Ajloun Ridge the ridge structure dictates rain shadow desert. The 300 mm/yr isohyet is approximately at longitude 245 (Kessler, 2002), and is a desert area with little replenishment. Hydrological data points to the basaltic aquifer of North Jordan as the main source of this water (El-Naser, 1991; ESCWA et al., 1996). Replenishment of the basaltic aquifer occurs in Jebel Al-Druze in Syria, where average precipitation is at 500 mm/yr (ESCWA et al., 1996) and the structural configuration related to the large strike-slip Sirhan Fault allows direct contact between the basalt units and the Wadi Sir and Amman formations (Bein et al., 2003).

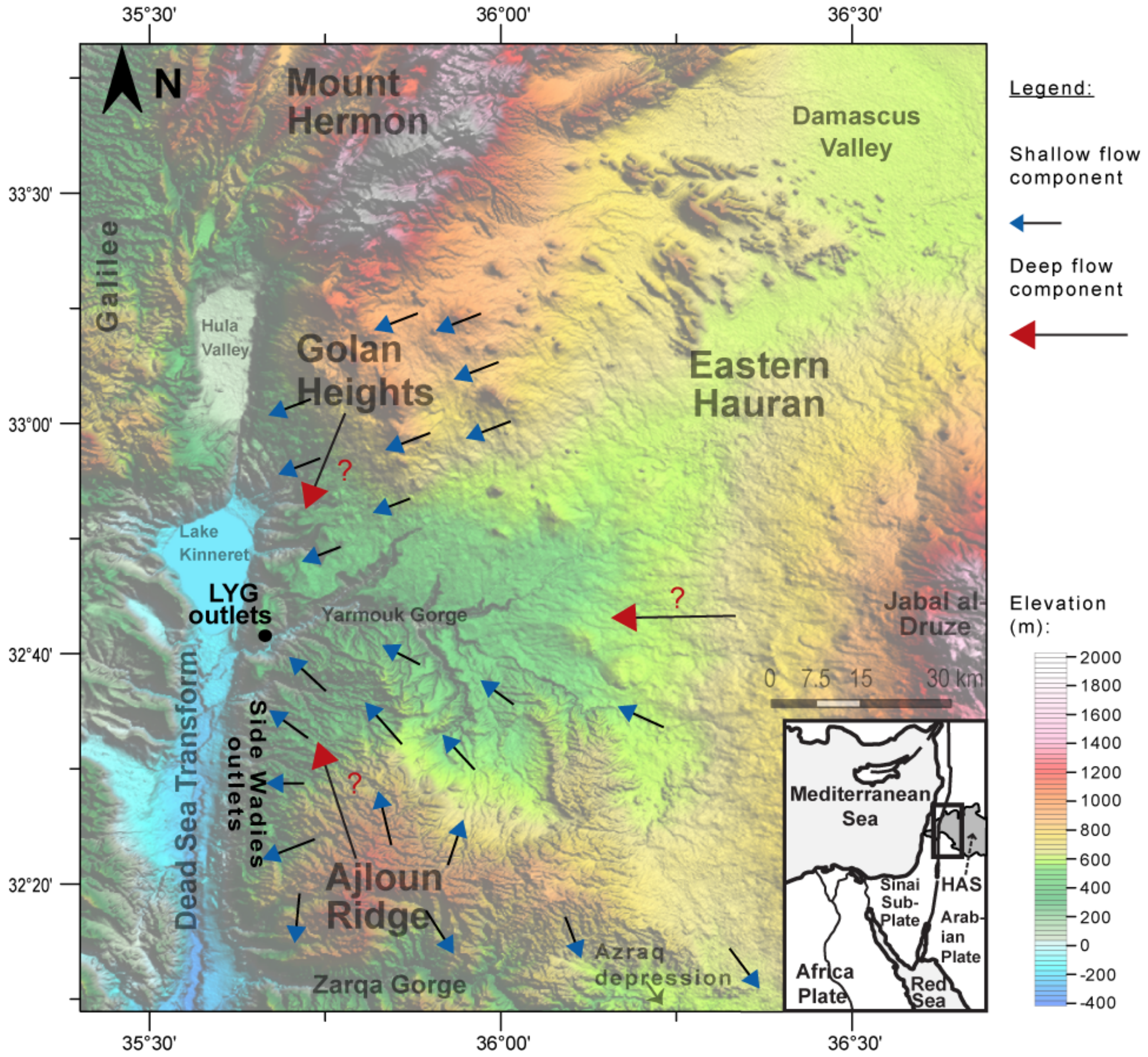

Figure 5. Schematic representation map of flow direction. Blue arrows indicate shallow groundwater flow, mostly referring to flow in the GH basaltic aquifer, Wadi Sir Fm. or Amman Fm. aquifers. Question marks indicate flow directions proposed in literature.

As indicated above most of the discharging water at the Ajloun Ridge is shallow circulating groundwater at the Wadi Sir Fm. and Amman Fm. aquifers. Regarding the deep flow regime, which is of prime importance when the geothermal state is to be examined, data is scarce since deep aquifer units' exposures are limited and very few wells reach them. Previous works have drawn different conclusions as to the possible deep flow path toward the LYG outlets.

The LYG Springs appear in two groups: Mokheibe on the Jordanian side, which includes two springs - Ein Maqla and Ein Balsam, (Bajali et al., 1997), and Hammat Gadder on the Israeli side, which includes five springs- Skhina, Maqla, Riekhe, Balsam and Bolos (Levitte et al., 1978). It is generally agreed by researchers of the area that the majority of discharging water at the LYG originates from the Ajloun Ridge, from Wadi Sir Fm. and Amman Fm. aquifers, and that the temperature and salinity differences among the springs and wells in the LYG is due to different degrees of mixing of a cold-fresh component of shallow origin and more salty hot groundwater of deep origin; however, regarding the hot flow component path and its origin there is little overall agreement. Arad and Bein (1986), analyzing light isotopic composition, ascribe this hot component to the horizons of Judea Gr. or even Jurassic strata and to the replenishment in the Hermon and Northern GH. Gilad (1985) claimed that such a flow component from the Hermon is a major component of discharging water at the LYG outlets, while TAHAL (1989) claimed that it accounts for a few MCM/yr only. In contrast, Bajjali et al. (1997) suggested, based on chemical and isotopic data (from Maqla Spring and JRV1 well at the Jordanian side), that there is a deep flow component originating from the upper reaches of the Ajloun Highlands toward the LYG outlets through the A1-A6 strata (unit 5 and 6). Another explanation (El-Naser, 1991) involves deep flow at the Kurnub aquifer (unit 4) originating east to the LYG, also from the Jebel Al-Druze area (the various suggested deep flow components marked in Fig. 5). As there is no consensus among researchers on this issue, the present work included testing of different flow configurations.

3. Methodology

3.1. Mathematical-physical model

The computational numerical model includes solution of macroscopic partial differential equations (PDEs) for conservation of mass, momentum and energy of hydrogeological-related porous media, including both solid matrix and saturating fluid, where a single saturating fluid is considered- pure liquid water.

The single fluid phase assumption is a consequence of using Darcy's law, and discounting thin, unsaturated niches in small areas at the upper part of the section (<5%), assuming it does not significantly affect the flow pattern. This simplifies numerical calculations significantly. It was also verified that no phase transition (steam occurrence) is expected under the p-T conditions.

Additional major assumption include admissibility of 2-D modeling (consequences discussed in section 5.2), and discounting chemical effects. Water sources exhibit dilute concentrations, rarely exceeding 1,000 mg/l TDS. The hottest and most salty spring in the LYG is Maqla Spring, with salinity of 1,300-1,400 mg/l TDS (Bajjali, 1994; Margane et al., 2002). Even if we consider salinities of 5,000 mg/l TDS in some deep aquifer layers, the impact on water viscosity, density and specific heat capacity is negligible, having essentially no effect on internal energy of the porous media (Philips, 1981; Palliser and Mckbbin, 1998[a] and 1998[b]; Kenneth et al., 1984).

I now present the process of deriving the PDEs, including the main assumptions, phenomenological laws, equations of state and the constitutive equations. The equations' derivation process is based on Diersch and Koldits (2002), including remarks by Bear (1972), Bear and Bachmat (1991), De Marsily (1986), Diersch (2009), Nield and Bejan (2006), (citations indicated in the text) where the various sources are mostly in agreement.

This study involves solutions by two numerical codes: FEFLOW version 5.3 and COMSOL versions 3.5a and 4.2. Scenario testing and actual model results (section 5.2) rely on FEFLOW solutions; later in section 5.5 the two numerical codes' solutions are compared. The solved thermal energy balance equations (Eq. (27)) are identical in all COMSOL versions and FEFLOW. The mass balance equations and density and viscosity correlations solved are not identical for all codes and versions. The balance PDEs are derived first as they appear in FEFLOW, and later, in the relevant section the equations forms solved by COMSOL are indicated and compared.

3.1.1. Derivation of the balance PDEs

Macroscopic conservation equations

The small-scale geometric complexity of geological media dictates that physical-mathematical problems be solved via a macroscopic approach. Transformation from microscopic to macroscopic is achieved by performing spatial averaging over a representative elementary volume (REV), leading to measurable and solvable quantities allowing application of the continuum assumption.

Applying an Eulerian frame of reference with Cartesian coordinates, the macroscopic balance mass and energy conservation PDEs are

Mass conservation

The fluid mass conservation is given by (e.g. Bear, 1972, Diersch, 2009)

$$\frac{\partial}{\partial t}(\theta\rho)+\nabla\cdot(\theta\rho v)=Q \tag{1}$$

where θ is the porosity, ρ the fluid density, v a macroscopic fluid velocity vector, and Q a bulk mass source term. Discounting chemical effects, Q is set to zero.

Momentum conservation (Darcy's law)

$$q=-\frac{k}{\mu}\cdot(\nabla p-\rho g) \tag{2}$$

where k is a permeability tensor of the porous media, μ the fluid phase dynamic viscosity, p the pressure, g gravitational acceleration, and q a volumetric flux density (Darcy's velocity); assuming very slowly deformable media ($v^s \approx 0$), q is given by

$$q=\theta v \tag{3}$$

The Darcy linear momentum balance of Eq. (2) is obtained by neglecting inertial, compression and deformation terms, and further assuming that inertial forces are small compared with viscous forces (porous media Reynolds number- Re <1-10; e.g. Bear, 1972, De Marsily, 1986, Diersch and Koldits, 2002).

By transforming Darcy's law (Eq. (2)) to terms of hydraulic head, h, under consideration of density effects we arrive at (e.g. Diersch, 2009)

$$q=-(k\rho_0 g/\mu)\cdot\left(\nabla h+\frac{\rho-\rho_0}{\rho_0}\nabla z\right) \tag{4}$$

where ρ_0 is a reference density at a reference temperature T_0 and head h_0 conditions $\rho_0=\rho_{0(h_0,T_0)}$, the hydraulic head h is defined as

$$h=\frac{p}{\rho_0 g}+z \tag{5}$$

where z is a vertical coordinate (opposite to the direction of gravity).

The fluid (liquid) density ρ appear in the mass, momentum and energy balance equations (1), (2) and (27) respectively, is regarded as a state function of head h and temperature T

$$\rho = \rho(h,T) \tag{6}$$

The total differential yields

$$d\rho = \underbrace{\left(\frac{1}{\rho}\frac{\partial\rho}{\partial h}\right)}_{\gamma}\rho dh + \underbrace{\left(\frac{1}{\rho}\frac{\partial\rho}{\partial T}\right)}_{-\beta}\rho dT \tag{7}$$

where γ and β are compressibility and thermal expansion coefficients, respectively. Assuming γ and β to be constant, integration of (7) leads to the EOS for the density in the form

$$\rho^f = \rho_0 e^{\gamma(h-h_0)-\beta(T-T_0)} \approx \rho_0[1+\gamma(h-h_0)-\beta(T-T_0)] \tag{8}$$

whereas γ is considered constant, β cannot be regarded constant for geothermal applications where a large temperature range is considered. Perrochet and Tacher (1997) introduced a high accuracy 6th-order polynomial $\rho = \rho(T)$. A Taylor series expansion to a 6th-order polynomial results in a nonlinear variable thermal expansion $\beta=\beta(T)$ which is applied to the state Eq. (8), and is used in FEFLOW numerical code software (Diersch, 2009).

The dynamic viscosity of a fluid phase μ appearing in (2) is regarded as a function of temperature (further at section 3.1.3), namely

$$\mu = \mu(T) \tag{9}$$

according to the following empirical relationship (Diersch, 2009; Mercer and Pinder, 1974)

$$\mu^f(T) = \frac{\mu_0}{1+0.7063\varsigma - 0.04832\varsigma^3}, \quad \varsigma = \frac{(T-150)}{100} \tag{10}$$

where T is in degrees Celsius and μ_0 is the reference viscosity at 150°C.

The correlations set in COMSOL are of Watson et al. (1980), Phillips et al. (1981) and Phillips et al. (1983). These correlations take into account both pressure and temperature conditions for both fluid viscosity and density. Comparison of correlation results to experimental data (Appendix Tables) indicate a good fit.

The geometry dependent porosity θ variable appear in (1), and solid volume fraction θ^s variable, are given by

$$\theta = 1-\theta^s \tag{11}$$

θ variable is influenced by compression work of the solid skeleton (deformation), while temperature effect is considered negligible. Thus, (e.g. Bear, 1972, Diersch, 2009)

$$d\theta = \frac{\partial\theta}{\partial p}dp = \left(\frac{1}{\theta^s}\frac{\partial\theta}{\partial p}\right)\theta^s dp = \Upsilon(1-\theta)dp \tag{12}$$

where Y denotes the coefficient of skeleton compressibility.

Writing the fluid mass conservation Eq. (1) in more detail (Diersch, 2009)

$$\underbrace{\theta\frac{\partial\rho}{\partial t}}_{1}+\underbrace{\rho\frac{\partial\theta}{\partial t}}_{2}+\underbrace{q\nabla\cdot\rho}_{3}+\underbrace{\rho\nabla\cdot q}_{4}=0 \tag{13}$$

The first term can be developed by using the state Eq. (7) as

$$\theta\frac{\partial\rho}{\partial t}=\theta\rho\left(\gamma\frac{\partial h}{\partial t}-\beta\frac{\partial T}{\partial t}\right) \tag{14}$$

The second term is provided by using constitutive Eq. (12)

$$\rho\frac{\partial\theta}{\partial t}=\rho\mathrm{Y}(1-\theta)\frac{\partial h}{\partial t} \tag{15}$$

Analogously to relation (14), the third term yields

$$q\nabla\rho=\theta\rho(\gamma\nabla h-\beta\nabla T) \tag{16}$$

Accordingly, the continuity Eq. (1) leads to the following form

$$S\frac{\partial(h)}{\partial t}+\nabla\cdot q=Q_{EB} \tag{17}$$

where S is the specific storage, defined as

$$S=\theta\gamma+(1-\theta)\mathrm{Y} \tag{18}$$

and

$$Q_{EB}(T)=\theta\beta\frac{\partial T}{\partial t}+q\beta\nabla T \tag{19}$$

where compression work been neglected. Further inserting (4) in to (17), yields

$$S\frac{\partial(h)}{\partial t}+\nabla\cdot\left[-(k\rho_0 g/\mu)\left(\nabla h+\frac{\rho-\rho_0}{\rho_0}\nabla z\right)\right]=Q_{EB} \tag{20}$$

The mass balance in Eq. (20) (solved by FEFLOW) is corresponds to the so-called extended Oberbeck–Boussinesq (OB) approximation. The OB approximation neglects all density dependencies in the balance terms, except for the crucial buoyancy term ρg which is retained in Darcy's law (Eq. (2) and (4)), (exception is fluid compression effect included in the specific storage S, relations (18)), In order to achieve analysis simplification in the system of balance equations, which is coupled by the nonlinearity in ρ, the OB approximation becomes invalid for large density variations; hence an extended form of OB is employed (Diersch, 2009; Diersch and Koldits, 2002).

Regarding the mass balance equations solved using COMSOL (Eq. (21) and (22)), in COMSOL version 3.5a (Eq. (21)) is according to the OB approximation and as stated above may produce result in significant inaccuracy in the solution. The mass balance equation (Eq.(22)) solved by COMSOL version 4.2 does not include the lhs term in Eq. (19) (included in the equation solved by FEFLOW), but since that term is time dependent and the model considered is mostly for steady state, this difference is insignificant in the current case study. Additional small and insignificant difference is the fluid compression work included in Eq. (22) (solved by COMSOL 4.2) in the divergence term applied on fluid density multiplied by Darcy's law, that is neglected in Eq. (20). Summarizing, for steady state the mass balance equations solved in COMSOL version 4.2 and FEFLOW are basically identical, while the equation solved by COMSOL version 3.5a is physically significantly different and may lead to inaccurate solutions (COMSOL, 2008, 2011; Diersch, 2009).

$$S\frac{\partial p}{\partial t}+\nabla\cdot\left[-\frac{k}{\mu}(\nabla p+\rho g\nabla z)\right]=0 \qquad (21)$$

$$\rho S\frac{\partial p}{\partial t}+\nabla\cdot\rho\left[-\frac{k}{\mu}(\nabla p+\rho g\nabla z)\right]=0 \qquad (22)$$

Energy conservation

Neglecting kinetic energy variations (e.g. Bear, 1972, Nield and Bejan, 2006), the energy balance equation for fluid phase is

$$\frac{\partial}{\partial t}(\theta\rho E)+\nabla\cdot(\theta\rho v E)+\nabla\cdot(j)=H_e \qquad (23)$$

and for the solid phase is

$$\frac{\partial}{\partial t}\left(\theta^s\rho^s E^s\right)+\nabla\cdot(j^s)=H_e^s \qquad (24)$$

where E and E^s is the internal (thermal) energies for fluid and solid respectively, j a nonadvective energy flux comprising dispersive and conductive components, j^s conductive energy flux in solid phase, and H_e and H_e^s represents the energy source term comprising internal and external energy supply in solid and fluid phases, respectively.

The internal energies E and E^s, is a thermodynamic state function of the form* (Bear and Bachmat, 1991; Diersch and Koldits, 2002)

$$dE=\left(T\left.\frac{\partial p}{\partial T}\right|_{\upsilon}-p\right)d\upsilon+c\,dT \qquad (25)$$

where $\upsilon=1/\rho$ is the specific volume, and c the specific heat capacity defined by

$$c=\left.\frac{dE}{dT}\right|_{\upsilon} \qquad (26)$$

Neglecting the effect of pressure variation on internal energy, and regarding c as independent of temperature (Bear and Bachmat, 1991; Diersch and Koldits, 2002; see section 3.1.3), the internal energies E and E^s may be given explicitly by

$$E\approx c(T-T_0) \qquad (27)$$

Furthermore, local thermal equilibrium is assumed between all phases (e.g. Bear, 1972, De Marsily, 1986), viz.,

$$T^{\alpha} - T = 0 \qquad \alpha = f, s \tag{28}$$

This enables the introduction of the system temperature T, and *Energy conservation* becomes

$$[\theta \rho c + (1-\theta)\rho^{s} c^{s}]\frac{\partial T}{\partial t} + \rho c q \cdot \nabla T + \nabla \cdot j = H_{e} \tag{29}$$

The convective (or advective) form in (21) and (22) was transformed from the basic divergent form of (27) by inserting (1) (Diersch, 2009; Diersch and Koldits, 2002).

The nonadvective (dispersive) energy flux vector j is expressed by a linear Fourier heat flux, given by

$$j = -\lambda_{td} \cdot \nabla T \tag{30}$$

with the tensor of hydrodynamic thermodispersion λ_{td} defined as (e.g. Diersch and Koldits, 2002):

$$\left.\begin{aligned} \lambda_{td} &= \theta(\lambda_{c} + \lambda_{m}) \\ \lambda_{c} &= \lambda I \\ \lambda_{m} &= c\rho D_{m} \end{aligned}\right\} \tag{31}$$

where T is the temperature, λ_c the conductive part of the thermodispersion tensor, λ the thermal conductivity, I a unit tensor, c a specific heat capacity, λ_m the mechanical part of the thermodispersion tensor, (described by the Scheidegger–Bear relationship; Bear, 1972) and D_m the tensor of mechanical dispersion defined as

$$D_{m} = \beta_{T}\|v\| I + (\beta_{L} - \beta_{T})\frac{v \otimes v}{\|v\|} \tag{32}$$

where β_L and β_T are the longitudinal and transverse dispersivities, respectively, and $\|v\|$ the velocity magnitude. There are differing points of view regarding the magnitude of the thermal dispersivity (mechanical part of the thermodispersion tensor λ_m). Bear (1972) and others concluded that the effects of thermal dispersion are negligible compared to conduction (at Pe<3,000 ~Re<3). De Marsily (1986), however, claims that solute and heat dispersivities are of comparable magnitude. Herein, the lower velocity amplitudes indicate negligible contribution of the thermal dispersion mechanism to the total heat transfer according to both estimations.

Specific heat capacity c and Thermal conductivities λ are regarded as constant in the present study (further in section 3.1.3).

***The use of the internal energy E state function (8), assumes negligible compression work effects. If pressure effects are important, the enthalpy state function is used (Diersch and Koldits, 2002).**

Relevant boundary conditions

On the boundary *Γ* enclosing the domain's disjoint portions, defined as $\Gamma = \Gamma_1 \cup \Gamma_2 = \Gamma_3 \cup \Gamma_4$, boundary conditions are separately specified.

For equations (20), (21) and (22) (fluid mass conservation):

$$\left.\begin{aligned} h(x_i,t) &= h^R \quad on \quad \Gamma_1 \\ q_n(x_i,t) &= q^R \quad on \quad \Gamma_2 \end{aligned}\right\} \tag{33}$$

For Eq. (29) (thermal energy conservation):

$$\left.\begin{aligned} T(x_i,t) &= T^R \quad on \quad \Gamma_3 \\ j_n(x_i,t) &= j^R \quad on \quad \Gamma_4 \end{aligned}\right\} \tag{34}$$

where h^R and T^R are prescribed boundary values of hydraulic head and temperature respectively, and q_n and j_n are the Darcy and heat normal fluxes, respectively.

3.1.2. Physical properties of water and rock

Following are detailed main characteristics and dependencies of the physical properties appearing in the mathematical models, and the guidelines for determination of values for the computational model.

In the physical problem at hand, pressure and temperature ranges are of 0.1-45 MPA and 20-200^{o}C respectively, where the significant temperature range is 20-150^{o}C (scenario 1, 3 and 4388). In these ranges rock and water properties are often variables and *p*-*T*-dependent, usually affected more by temperature than pressure. High non-linearity of the equations dictates considering only the essentials dependencies.

Properties of water

dynamic viscosity, *μ*: in the temperature range 20-200^{o}C dynamic viscosity temperature affect is most pronounced, entailing a change of nearly an order of magnitude in *μ* an order decrease with increasing temperature (see Fig. 6 and Table 12 in the appendix), while pressure variation shows little effect. The commercial code FEFLOW regards viscosity as temperature dependent only (relation 10).

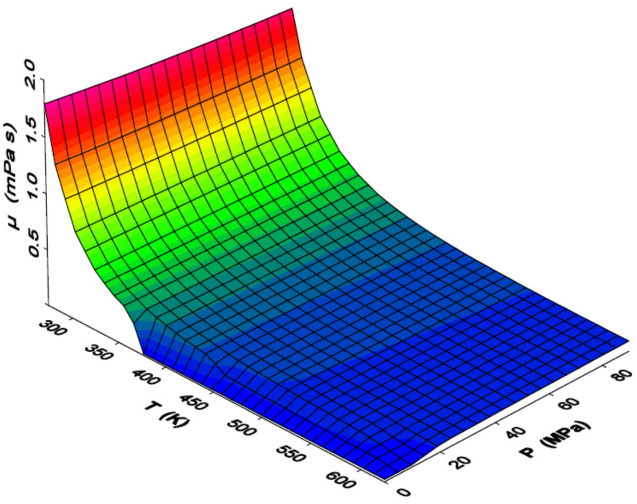

Figure 6. Water viscosity *μ* vs. pressure *p* and temperature *T*, diagram based on Clauser (2006).

Density, ρ: in the relevant ranges, the effect of temperature variation on density is more pronounced (~10%) than that of pressure (~3%, see Fig 7 and Table 11 in the appendix). Water density was regarded as temperature and pressure-dependent as further detailed in section 3.1.1

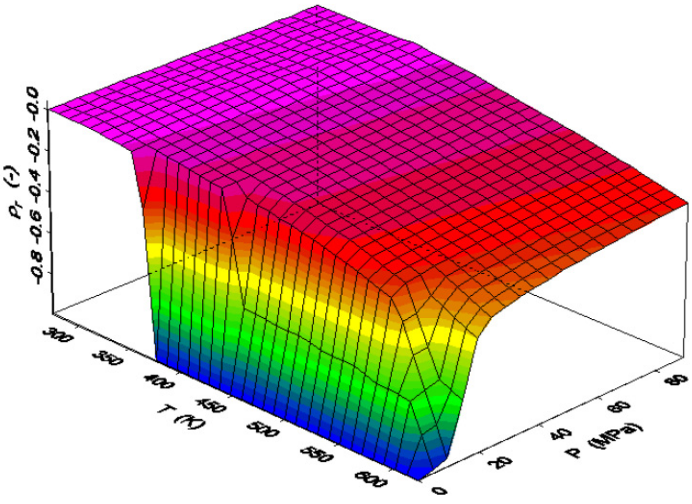

Figure 7. Water relative density ρ_r ((ρ-ρ_0)/ρ_0) vs. pressure *p* and temperature *T*, diagram based on Clauser (2006).

Thermal conductivity, λ: Water thermal conductivity changes non-linearly with temperature (~20%), and moderately with pressure (~4%, see Table 14 in the appendix). Water comprises only a relatively small portion of the saturated rock, which only can generally be estimated (to be discussed further in this section). Effective thermal conductivity (overall thermal conductivity, of the combined phases) was treated as a parameter whose value is known to a limited accuracy.

Specific heat capacity, c: specific heat capacity is moderately influenced by temperature and pressure (see Table 13 in the appendix) but in a roughly opposed way. This means that, in general, fluctuations of specific heat capacity due to temperature variation are mostly masked by fluctuations due to pressure variation. The actual maximum expected fluctuations are approximately 4%, usually much lower, and so effects of temperature and pressure on specific heat capacity may be discounted.

Properties of rock

Effective Porosity, θ: rock porosity in the study area composed mostly from first and secondary porosity. Secondary porosity is due to diagenetic pores (Dolomite rocks), microfractures and karstic voids. Although in the present study porosity determination is involved in calculating effective thermal conductivity, bulk specific heat capacity and specific storage, its main significance is in regard of effect on permeability, most notably in deep groundwater flow.

Effective porosity and hence permeability are considerably reduced with lithostatic load and rising temperature, occurring with increasing depth (Bundschuh and Suárez, 2010). Empirical relations accounting for lithostatic load and burial depth, indicate that porosity of carbonate rock tends to decrease by half for a burial depth of 1750 m, and by two thirds for burial depth of 3000 m (Athy, 1930; Schmoker and Halley, 1982), an effect that is more pronounced for dolomite rock than for limestone (Schmoker and Halley, 1982). Temperature variations also considerably affect porosity, as a rise in temperature causes dilatation of the solid phase and increase of thermo-mechanical stress. Experiments show a 65% reduction in porosity between 21°C and 163°C. Fluid-rock geochemical interactions may also affect absolute permeability by accumulation of minerals in pores and fractures (Bundschuh and Suárez, 2010).

Intrinsic permeability, k: rock permeability is defined as the rock's ability to transmit fluids through interconnected pores and fractures. Permeability associated with flow in intergranular pores and microfractures (<1 mm) obeys Darcy's law of laminar flow, while permeability in fractures and faults is often turbulent and a non-linear momentum balance should be applied (Bundschuh and Suárez, 2010). Developed karst in the Hermon Ridge may result in local inaccuracy of flow patterns in model results.

As discussed above, rock permeability tends to decrease most considerably with burial depth, due to the poroelastic effect and thermo-solid dilation. That effect is expected to considerably reduce permeability of deep layers (<3 km), limiting the possible depth of groundwater flow and with it heat convection from very deep horizons.

Another aspect of permeability to be considered is that stratification often leads to anisotropy of permeability in sedimentary rock. Its value parallel to the bedding tends to be much higher than normal to the bedding, usually by a full order of magnitude (Bear, 1972).

Table 5. Permeability and hydraulic conductivity values, modified from Bear (1972).

<table>
<tr><th colspan="5">Impervious</th><th colspan="4">Semi-Pervious</th><th colspan="4">Pervious</th><th>Permeability</th></tr>
<tr><td colspan="4"></td><td colspan="4">Very Fine Sand, Silt, Loess, Loam</td><td colspan="3">Well Sorted Sand or Sand & Gravel</td><td colspan="2">Well Sorted Gravel</td><td>Unconsolidated Sand & Gravel</td></tr>
<tr><td colspan="4">Unweathered Clay</td><td colspan="3">Layered Clay</td><td colspan="2">Peat</td><td colspan="4"></td><td>Unconsolidated Clay & Organic</td></tr>
<tr><td colspan="2">Fresh Granite</td><td colspan="2">Fresh Limestone, Dolomite</td><td colspan="2">Fresh Sandstone</td><td colspan="3">Oil Reservoir Rocks</td><td colspan="4">Highly Fractured Rocks</td><td>Consolidated Rocks</td></tr>
<tr><td>10^{-19}</td><td>10^{-18}</td><td>10^{-17}</td><td>10^{-16}</td><td>10^{-15}</td><td>10^{-14}</td><td>10^{-13}</td><td>10^{-12}</td><td>10^{-11}</td><td>10^{-10}</td><td>10^{-9}</td><td>10^{-8}</td><td>10^{-7}</td><td>κ (m^2)</td></tr>
<tr><td>10^{-12}</td><td>10^{-11}</td><td>10^{-10}</td><td>10^{-9}</td><td>10^{-8}</td><td>10^{-7}</td><td>10^{-6}</td><td>10^{-5}</td><td>10^{-4}</td><td>10^{-3}</td><td>0.01</td><td>0.1</td><td>1</td><td>k (m/s; at 25°C)</td></tr>
</table>

Heat generation- bulk heat source, H_e: The significant contributing radioactive isotopes are of the decay series of ^{238}U, ^{235}U,^{232}Th and of the isotope ^{40}K (Turcotte and Schubert., 2002; Rybach,1988). Considering mainly limestone and dolomite rocks, and estimating heat production rate from radioactive decay of 0.5 μWm^{-3} (Table 6), the expected contribution to total basal heat flow from a section of 4,000 m is 2 mW/m^2, indicating negligible heat contribution from that source.

Table 6. Heat production rate of common sedimentary rocks (Rybach, 1988).

Rock type	Heat production rate (μWm^{-3})
limestone	0.62
Dolomite	0.36
Anhydrite	0.090
Shales and siltstone	1.8
Sandstone	0.32-0.99

Effective thermal conductivity, λ_e: For the physical problem under consideration, thermal conductivity is of considerable importance. This parameter, combined with flow conditions, determine the partitioning of basal heat flow transferred to the surface and to water outlets, and significantly affecting estimated basal heat flow.

The thermal conductivity coefficient accounts mostly for lattice or phonon heat conductivity, where radiation heat transfer is negligible at the crust conditions and is included in the heat conductivity coefficient (Clauser and Huenges, 1995). Thermal conductivity measured on rock samples (e.g. cores or cuttings), in-situ in boreholes or with marine heat flow probes show large variability for each rock type (e.g. Fig. 8; Clark, 1966; Čermák and Rybach, 1982). This variability is attributed to the heterogeneity in mineral composition, microstructure, porosity, saturation and experimental conditions (Clauser and Huenges, 1995).

In cases of porous rock (θ □1%), saturating fluids significantly affect bulk thermal conductivity of the saturated rock, due to reduction in contact resistance between grains by saturating fluid (Clauser and Huenges, 1995). Effective thermal conductivity (overall thermal conductivity, of the combined fluid and solid phases) is estimated by different mixing law models, where the parallel and series conduction models lead to the arithmetic and harmonic means, respectively, and define upper and lower limits for all other models. The geometric mean mixing law (Eq. (35)) fits, in most cases, experimental results and field data (Clauser and Huenges, 1995; Drury and Jessop, 1983; Seikiguchi, 1984; Woodside and Messmer, 1961):

$$\lambda_e = \Pi(\lambda^{\alpha})^{\theta^{\alpha}} \tag{35}$$

where λ_e is the effective thermal conductivity, λ^{α} the thermal conductivity of phase α (fluid or solid) and θ^{α} the volume fraction of phase α.

Stratification in sedimentary rock may produce some anisotropy, where thermal conductivity parallel to the bedding (λ□) is often slightly larger than that normal to it ($\lambda^{\perp}$). Average anisotropic factor $\bar{a}$ (λ□$/\lambda^{\perp}$) in water-saturated rock is ~1.1. An exception is highly lithified argillites, where $\bar{a}$ is ~2 (Brigaud and Vasseur, 1989; Clauser, 2006).

Rocks thermal conductivity usually varies inversely with temperature, as a rise in temperature is accompanied by thermal expansion, which varies from mineral to mineral, resulting in "thermal cracking" and increase in contact resistance between minerals grains. This effect is more moderate in water-saturated rock than in dry rock. Up to 200°C there is a reduction by 15-30%, both for clastic and carbonaceous sediments (Brigaud and Vasseur, 1989; Clauser and Huenges, 1995; Abdulagatov et al., 2006).

Somerton correction is considered reliable for describing sedimentary rock thermal conductivity variation with temperature (Lee and Deming, 1998; Somerton, 1992):

$$\lambda(T) = \lambda_{RT} - 10^{-3}(T-293)(\lambda_{RT} - 1.38)\left[\lambda_{RT}(1.8*10^{-3}T)^{-0.25\lambda_{RT}} + 1.28\right]\lambda_{RT}^{-0.64} \tag{36}$$

where λ_{RT} is rock thermal conductivity at 20 °C. Pressure effect on thermal conductivity is more modest than that of temperature. Generally, rock thermal conductivity increases with pressure, but differently for distinct pressure ranges. When a sample is brought to the surface, the drop in stress causes fractures and microcracks to develop. This in turn increases contact thermal resistance. Upon artificial pressure increase in the lab, cracks are closed once more and internal thermal resistance decreases. (Čermák and Rybach, 1982; Clauser and Huenges, 1995; Abdulagatov et al., 2006). At an overburden pressure of about 15 MPa, an increase in pressure no longer appreciably alters thermal conductivity. This effect accounts for an increase of about 10-15 % relative to thermal conductivity at ambient conditions. A further pressure increase to 40 MPa does not affect thermal conductivity significantly (Clauser and Huenges, 1995).

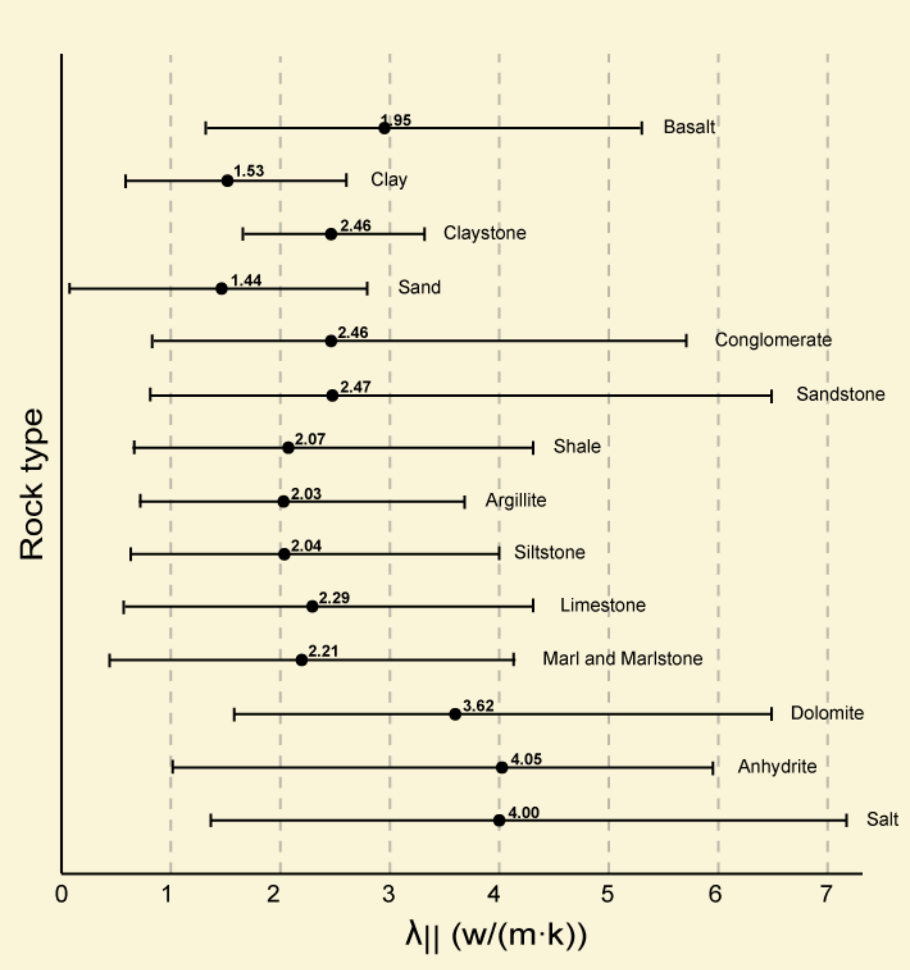

Figure 8. Thermal conductivity of different rocks at room temperature, modified according to Zoth and Haenel (1988) (bars indicate range of measurements).

Determination of thermal conductivity for the computational model was done according to each model unit rocks types. Anisotropy was discounted in accordance with literature measurements performed on dry samples extracted from depth, and considering high temperatures prevail in the lower units.

<u>Additional physical properties</u>: As simulations are mostly for steady state, coefficients derived with respect to time or multiplied by a time derivative are of low importance. These properties include: specific storage S, porosity θ, rock (solid) specific heat capacity c^s and density ρ^s where a single value was set to all model units.

4. Conceptual model and model formulation

4.1. Conceptual model

The conceptual model illustrated in Fig. 9 synthesizes the significant geological and hydrothermal aspects and hypothesies presented in section 2, including division to aquifers, aquitards, aquicludes, enhanced vertical permeability zone, water table location, types of boundary conditions, and schematic non-isothermal groundwater flow pattern.

In accordance with section (2.3) large scale shallow cold groundwater flow occurs at the Ajloun Ridge in Amman Fm. and Wadi Sir Fm. aquifers (units 7 and 9) toward the LYG and Wadi Zarqa (2-D limitations). Detached shallow groundwater flow circulation is present at the GH basaltic aquifer (unit 11).

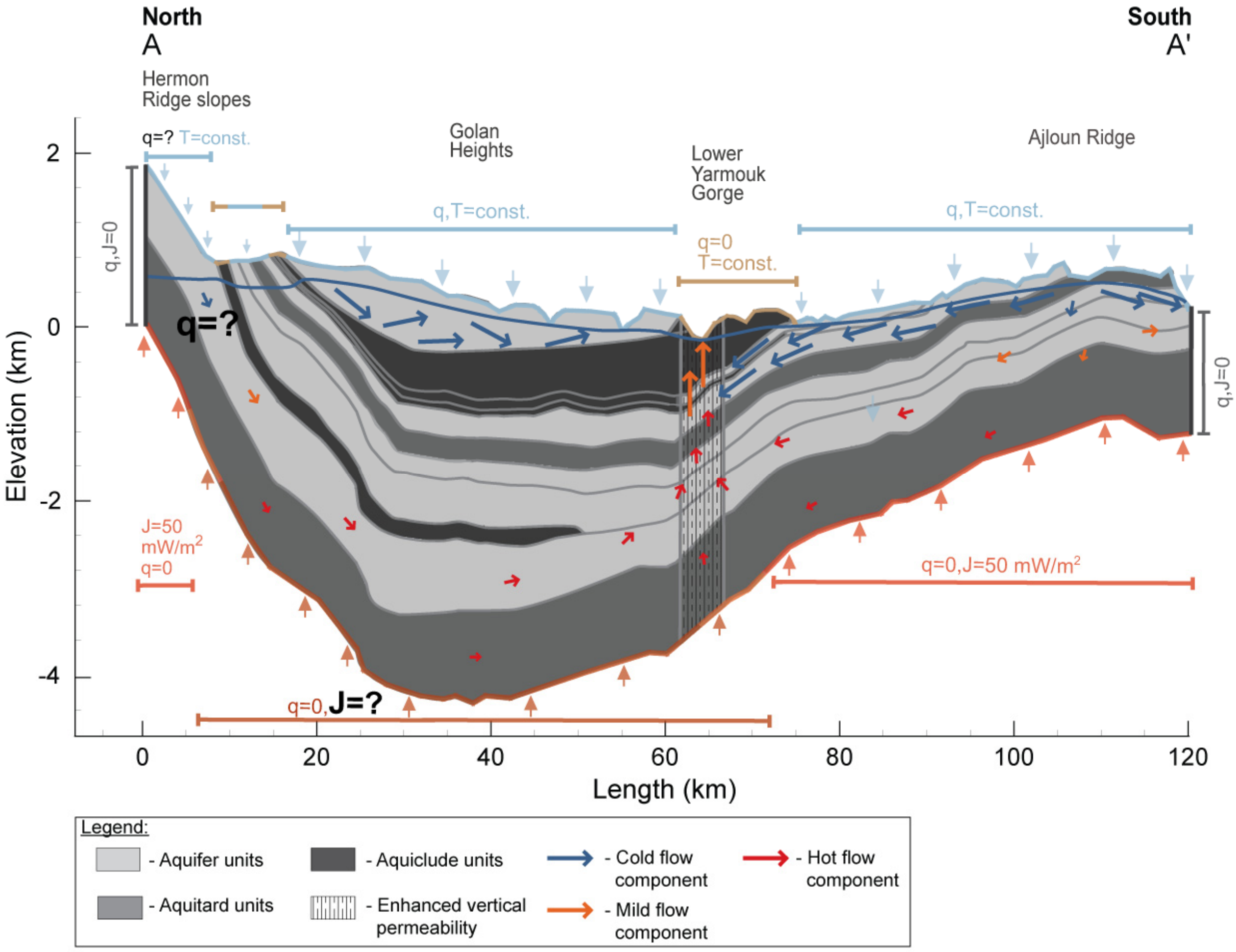

Figure 9. Conceptual model sketch; *q* and *J* are mass and energy fluxes respectively, *T* is temperature.

Deep groundwater flow occurs at the Ajloun Ridge from limited water percolation through aquitard unit 6 (units A3-6 or Dir Hanna Fm.), flowing downward and later northward, toward LYG. While simultaneously being heated, they ascend through an enhanced vertical permeability zone below LYG.

Northward below GH, as indicated, it is questionable whether deep groundwater flow occurs and of what magnitude, and this will later be tested by different model scenarios. If such deep groundwater flow does occur, due to the syncline structure and the aquiclude nature of Kidod Fm. (unit 3) that overlies the Hermon Fm. Aquifer (unit 2), a winding deep flow path is expected. Somewhere in the section beneath the Yarmouk, Kidod Fm. is expected to terminate and Enhanced vertical permeability, brought on by faulting, allows groundwater to ascend from north and south toward the LYG outlets (or instead through permeable sections alone). Below LYG, at shallow depth, the cold and warm flow components mix and create a mild-temperature flow component which discharges to the surface. A deep groundwater flow may also exist and is accounted for by the aquitard permeability of the Jurassic-Triassic unit 1 (further at section 5.1).

On the upper boundary a steady-state surface temperature and constant mass flux are mostly assumed (further in section 5.1). Heat-insulation and impermeable conditions are assumed on vertical boundaries. Constant basal heat flow is assumed on the bottom boundary, assuming negligible groundwater flow occurs below. Below Ajloun Ridge and Hermon Ridge Slopes normal region heat flow is assumed, while at GH the heat-flux condition is unknown.

The objective of the numerical simulation is to deduce the unknown conditions base on sufficient known conditions (a form of reverse engineering). The two unknowns are boundary conditions of mass flux originating from the Hermon, and heat-flux beneath GH, while all other boundary conditions are assumed to be known. Additionally, there is available temperature and head data of the domain itself; this allows us to properly deduce the two missing boundary conditions.

4.2. Model formulation

The cross section used for the simulation and model units, are presented in Fig. 4, Table 2, respectively. The equations are solved with Feflow 5.3 numerical Finite Element Method (FEM) commercial software package. Extensively verified, benchmarked and validated (according to analytical solutions, numerical solutions, and experimental data respectively) including regarding groundwater heat transport problems including the thermohaline 3-D Elder problem and the thermohaline Salt Dome problem (Diersch, 2009; Diersch and Koldits, 2002). The FEFLOW package is also surveyed and recommended in several leading books, e.g. Bear et al., (2010), Holzbecher (1999), Huenges (2010) Kolditz (2002), Sorek and Pinder (1999).

4.2.1. Parameter values

Permeability, *k*: permeabilities and recharge values are based on previous hydrological studies (Bein et al., 2003; Dafny et al., 2003; Hobler et al., 2001; TAHAL, 1989) where a large volume of hydraulic parameter data was collected or, in the case of deeper units, estimated.

Special attention is given to permeability values of the Jurassic and Triassic section (units 1 and 2), since these constitute the maximal depth where flow and convection can occur. Hermon Fm. (J4) is composed of massive karstic limestone and dolomite, its thickness is 950 m and in the Hermon Ridge and Northern GH comprises a good quality aquifer. Likewise, there is no reason to assume that farther south; below the GH its hydraulic nature would change considerably.

Hermon Fm. overlies Beqassem (J3) Fm. which is composed of 170 m of medium to fine bedded limestone, considered impermeable and to comprise an aquiclude unit (Bein et al., 2003). Further below are Kalat Jandal (J2), Arne Fm. (J1), Asher volcanic. (Triassic) which are mainly composed of carbonates and mostly of dolomite (Hirsch et al., 2002). The hydraulic nature of these is not known, but if we consider the overlying aquiclode Beqassem Fm. and large burial depth (usually >3.5 km) in conjunction with high lithostatic pressure and the effect of high temperatures (discussed in section 3.1.3), it's not likely that considerable flow occurs in these formations.

Southward, beneath the Ajloun Ridge, the Triassic strata is much more shallow (<2 km below surface). The Triassic section is highly heterogeneous and, among other layers, contains thick beds of shale, clay, marl and anhydrite (Bandel and Khoury, 1981) which are usually known to be impermeable strata. As a rigorous assumption it was decided to assign aquitard permeability values and allow some extent of groundwater flow in that section.

Effective thermal conductivity was assigned according to section 3.1.3, specific storage and specific heat capacity values, as well as solid density values, indicated in Table 7.

Table 7. Values of parameters assigned to model units; *south to latitude 210; 2, 4- values refer to scenarios 2 and 4.

<table>
<tr><th colspan="9">Parameters values</th></tr>
<tr><th rowspan="2">Unit no.</th><th colspan="3">Hydraulic conductivity K (m/s)</th><th colspan="3">Anisotropy factor (k_y/k_x)</th><th colspan="2">Effective thermal conductivity λ_c (W/m°C)</th></tr>
<tr><th>North</th><th colspan="2">South</th><th>North</th><th>Yarmouk</th><th>South</th><th>North</th><th>South</th></tr>
<tr><td>1</td><td>3e-8</td><td colspan="2">3e-8</td><td>0.1</td><td>0.1</td><td>0.1</td><td>3.6</td><td>3.6</td></tr>
<tr><td>2</td><td>7e-7/1.5e-6^{2}/4.5e-6^{4}</td><td colspan="2">2e-6</td><td>0.1</td><td>0.1</td><td>0.1</td><td>3.5</td><td>3.5</td></tr>
<tr><td>3</td><td>1e-9</td><td colspan="2">-</td><td>0.1</td><td>-</td><td>-</td><td>1.9</td><td>-</td></tr>
<tr><td>4</td><td>1e-6</td><td colspan="2">5e-6</td><td>0.1</td><td>0.1</td><td>0.1</td><td>2.8</td><td>2.8</td></tr>
<tr><td>5</td><td>1.7e-6</td><td colspan="2">1.7e-6</td><td>0.1</td><td>0.1</td><td>0.1</td><td>3.5</td><td>3.5</td></tr>
<tr><td>6</td><td>7e-9</td><td colspan="2">7e-9</td><td>0.1</td><td>1</td><td>0.1</td><td>3.5</td><td>3.5</td></tr>
<tr><td>7</td><td>1.5e-6</td><td colspan="2">1e-5</td><td>0.1</td><td>0.1</td><td>0.1</td><td>3.5</td><td>3.5</td></tr>
<tr><td>8</td><td>1e-9</td><td colspan="2">1e-9 and 1e-5*</td><td>0.1</td><td>50</td><td>0.1</td><td>2.8</td><td>2.8</td></tr>
<tr><td>9</td><td>1e-9</td><td colspan="2">1e-5</td><td>0.1</td><td>0.1</td><td>0.1</td><td>2.8</td><td>2.8</td></tr>
<tr><td>10</td><td>1e-9</td><td>1e-6 (Yarmouk)</td><td>1e-9</td><td>0.1</td><td>1</td><td>0.1</td><td>2.8</td><td>-</td></tr>
<tr><td>11</td><td>3e-5</td><td colspan="2">-</td><td>0.1</td><td>-</td><td>-</td><td>2.2</td><td>-</td></tr>
<tr><td colspan="2">Specific storage S (m^{-1})</td><td colspan="2">1e-6</td><td colspan="3">Fluid specific heat capacity c (m^2/s^oC)</td><td colspan="2">4200</td></tr>
<tr><td colspan="2">Rock density ρ^s (kg/m^3)</td><td colspan="2">2600</td><td colspan="3">rock specific heat capacity c^s (m^2/s^oC)</td><td colspan="2">950</td></tr>
</table>

4.2.2. Boundary conditions

Flow boundary conditions

Boundary conditions are assigned according to hydrological data presented in section 2.3. Locations and values of boundary conditions for the fluid mass balance equation (equations (20), (21) and (22)) presented in Table 8 and fig. 10.

- Impermeable conditions are assigned at the base of the model and its vertical boundaries.
- On most of the upper boundary, constant mass flux is assigned. An exception is the upper boundaries belonging to aquiclude units, mostly unit 10 (Avdat, Mount Scopus and Balqa groups), which is considered impermeable and detached, and impermeable conditions are assigned.
- Zero gauge pressure (representing natural discharge) was assigned as follows: one point at GH accounting for natural outlets of the shallow basaltic aquifer, one point accounting for all LYG Springs, and to the far South partially accounting for the Side Streams and Wadi Zarqa Stream (2-D limitations).

- As indicated, it is unknown whether there is any groundwater leakage of Hermon origin towards LYG outlets, or the extent of such leakage. Likewise, flux was treated as unknown, and its effect was tested according to thermal field data in the different scenarios.
- Small scale flux is assigned to Northern GH, accounting for Judea Gr. exposures where minor water contribution may exist.
- In the GH mass flux is calculated according to average precipitation and the percolation coefficient.
- At the Ajloun Ridge, beyond the aforementioned considerations of average precipitation and percolation coefficients, further 2-D limitations exist. As indicated (section 2.3), only a portion of recharging water at the ridge is discharged at the LYG outlets, estimated at 25-35% of all replenishment at the ridge, depending, among others, on unknown amounts of groundwater originating at Hermon Ridge. This framework was kept maintained consistently, in order to represent correctly the south flow towards LYG outlets in the different scenarios.

Table 8. Values and locations of flow boundary conditions of model scenarios;1- Kessler (2002), 2-Dafny et al. (2003), 3- Margane et al. (2002), 4-Israel Meteorological Service (2010), 5-Bajjali et al. (1997).

Flow boundary conditions					
Scenario 4	**Scenario 2**	**Scenario 1 and 3**	**Constant Mass flux q_n^R (m/day)**		
			Average precipitation (mm/yr)	**Percolation coefficient (%)**	**Boundary location**
3e-4	0	7e-5	>1300[4]	>70[1]	Hermon slops (0-8.5 km)
3e-5	3e-5	3e-5	1200[4]	-	Judea Gr. GH (9-14 km)
4e-4	4e-4	4e-4	800[4]	20[2]	GH (15-61 km)
0	0	0	-	0	Boundaries of Units 10,3,8 and 9
5e-5	1.5e-4	1e-4	400[5]	15-30[3]	lower Ajloun (75-90 km)
1e-4	1.5e-4	1.5e-4	500[5]	15-30[3]	middle Ajloun (90-105 km)
2.5e-4	2.5e-4	2.5e-4	700[5]	15-30[3]	Upper Ajloun (105-120 km)
Scenario 4	**Scenario 2**	**Scenario 1 and 3**	**Constant Pressure p^R (gauge; bar)**		
			Boundary location		
0	0	0	GH (54.5 km)		
0	0	0	LYG (63.5 km)		
0	0	0	Ajloun (119.5 km)		

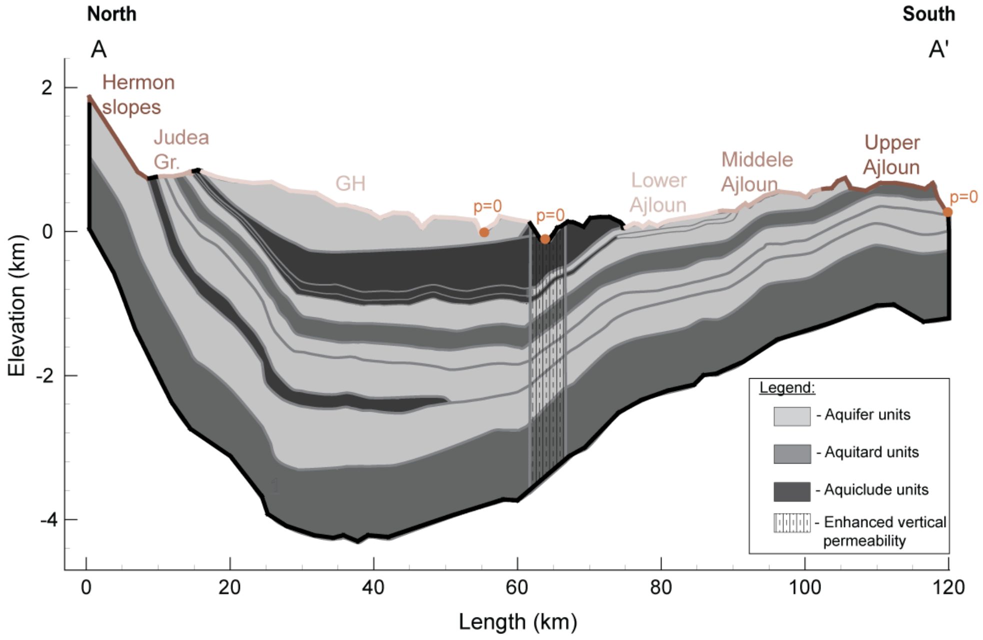

Figure 10. Locations of flow boundary conditions.

Thermal boundary conditions

Boundary conditions were assigned according to considerations detailed in section 2.2.2. Locations and values of boundary conditions for the thermal energy balance equation (Eq. (29)) presented in Table 9 and Fig. 11.

- Vertical boundaries are assigned as insulated.
- On the upper boundary the steady-state surface temperature (mean annual ground surface temperature) is considered to be linearly dependent on topographic elevation, as recommended by Powell et al. (1988).
- A value of 50 mW/m^2 is set beneath the ridge, as well as in a short strip beneath the slopes of Hermon.
- Under the GH the heat flux value is different for each scenario and it value, as well as different flow configurations of Hermon origin, is tested.

Table 9. Values and location of heat boundary conditions of model scenarios; surface temperature values are based on Israel Meteorological Service (2010) and Levitte et al. (1978).

Heat boundary conditions			
Scenario 3 and 4	**Scenario 2**	**Scenario 1**	**Constant temperature T^R (°C)**
			Boundary location
mean- 22°C	mean- 22°C	mean- 22°C	All Upper boundary besides outlets, elevation dependent
Scenario 3 and 4	**Scenario 2**	**Scenario 1**	**Constant Heat-flux j_{en}^R (mW/m^2)**
			Boundary location
50	50	50	bottom boundary, beneath Ajloun (70-120 km) and Hermon (0-7 km)
100	220	50	bottom boundary, beneath GH (10-65 km)
70	70 and 110	50	bottom boundary, transition (7-10 and 65-70 km)
0	0	0	vertical boundaries (0 and 120 km)

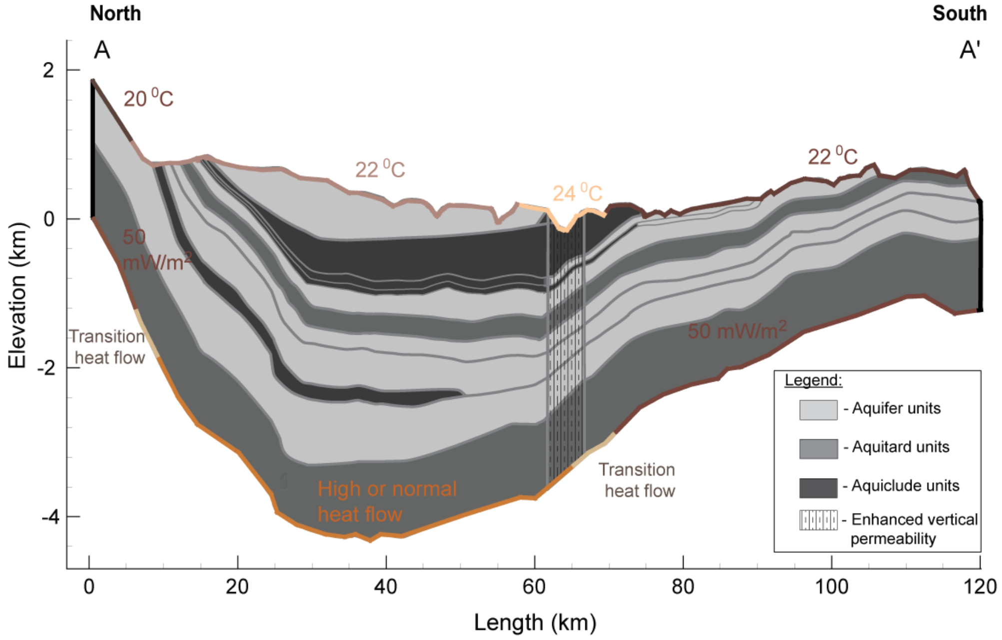

Figure 11. thermal boundary conditions locations.

4.2.3. Mesh construction

Several triangular meshes, of different node densities, were tested in order to achieve mesh-independent solutions; final mesh consisted of 60,000 elements and 31,000 nodes (fig. 12). Mesh density was increased in all areas of water and heat inlets (mainly upper and lower boundaries) as well as in the bottom unit domain (unit-1) where a large temperature gradient is expected. Extra mesh refinement was introduced at the fluid outlets and at the upwelling area beneath the LYG.

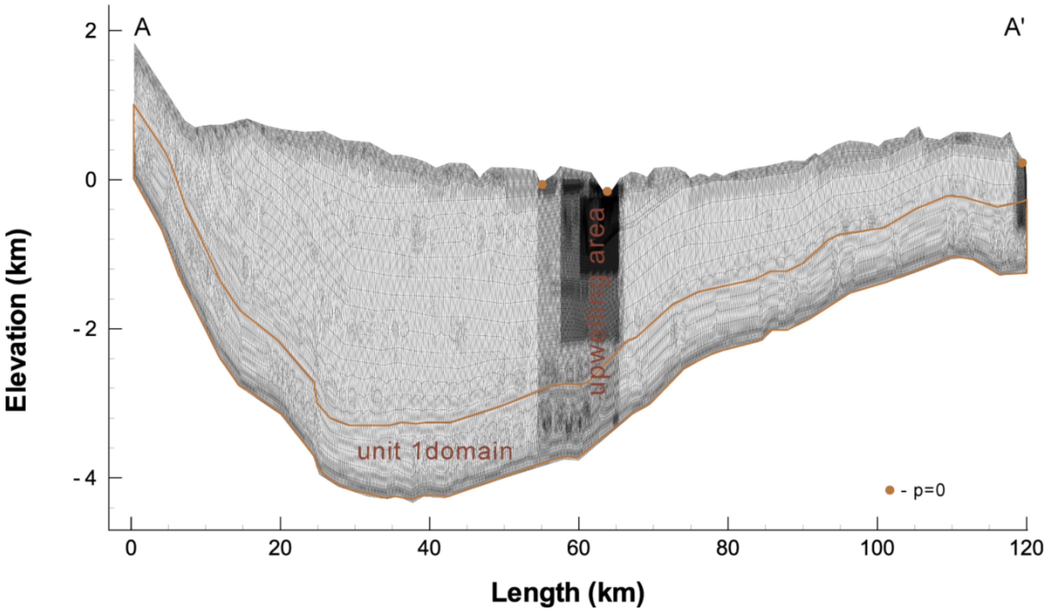

Figure 12. The mesh.

4.2.4. Calibration

Model permeability values were calibrated according to water level maps (Bein et al., 2003; Hobler et al., 2001) and temperature-depth data (Table 4 & 10), through conservation of the known geological structure and hydrogeological information. The known main faults were tested for various hydrological and thermal influences.

5. Results and discussion

5.1. Preliminary calculation- Integral thermal energy balance

The historical rate of thermal energy release (power) by the LYG Springs, *U*, is:

$$U = \rho Q_T c\Delta T \qquad (37)$$

where ρ is water density (taken as 1,000 kg/m^3), Q_T historical discharge of the LYG Springs, 1.44 m^3/s; *c* specific heat capacity,4,200 j/kg °C; and ΔT= 37°C-22°C= 15°C the difference between recharge and volume average discharge temperatures (Table 3). Setting these values yields

$$U = 1000\,(kg/m^3)*1.44\,(m^3/s)*4200\,(j/kg*^o\,\mathrm{C})*15\,(^o\,\mathrm{C}) = 90.72*10^6\,(W) \qquad (38)$$

The geothermal Peclet number (Pe) is often used in order to roughly evaluate heat conduction and convection of geothermal systems based on characteristic dimensions and physical attributes (Anderson, 2005; Phillips, 2009; van der Kamp and Bachu, 1989). It is defined as

$$Pe = \frac{\rho c q Z^2}{\lambda_c L} \qquad (39)$$

where λ_c is the effective thermal conductivity (~3 W/m°C), *Z* a characteristic vertical scale (~3,000 m), and *L* a characteristic flow path length of 65,000 m. *q* is the surface-averaged velocity, that is calculated assuming half of the water discharging at the LYG is of Hermon origin (0.72 m^3/s), and dividing it by the product of the basin width (assuming northwestern boundary is Hermon Ridge southwestern margins and northeastern boundary is Damascus Valley) of 30,000 m and the average depth of 3,000 m, yielding an average velocity of ~8e-9 m/s. Using these values, Eq. (39) yields Pe=1.6.

Pe>>1 indicates convection dominant, and Pe<<1 conduction is dominant. Peclet number values of ~1 indicates similar contribution of the two mechanism of heat transfer. Accordingly, a Pe value of 1.6 indicates that convective and conductive heat transfers are of similar magnitudes.

The maximal theoretical area available for heat transport beneath the GH and the Ajloun Ridge, *A*, is 2,000 km^2. With Pe=1.6, approximately half of the basin basal heat flow *J* is being transferred by convection to the LYG outlets while the other half is being conducted. The overall heat flux is thus:

$$2*U/A = J \qquad (40)$$

Setting values, yields:

$$J = 90.72*10^6\,(W)*2/2000\,(km^2) = 91\,(mW/m^2) \qquad (41)$$

The resulting value of 90 mW/m^2 is exceptionally high for this region and is attributed to an exceptional geothermal heat source and/or vast deep groundwater circulation.

5.2. Scenarios tested

The first scenario considered was meant to test whether the heat anomaly of the LYG can be explained by a deep forced convection component originating in the Hermon, under normal heat flux (50 mW/m^2). That flow component originates in the slopes of Hermon Ridge (described by the three bottom streamlines beneath the GH in figures 13 and 14), from which water percolates into the Hermon Fm. aquifer (unit 2), and flows southward. Due to the syncline structure and the aquiclude nature of Kidod Fm. (unit 3; dashed red line in Fig. 13), that overlies the Hermon Fm. aquifer, a winding deep flow path is dictated. Somewhere in the section beneath the Yarmouk, Kidod Fm. Is expected to terminate (Hirsch et al., 2002; TAHAL, 1989), allowing water to ascend to the LYG outlets through permeable sections. Because of this special lithological configuration, this flow component is expected to be at considerable depth- greater than 3 km. At such depths temperatures are high, and the water is heated. Beneath the Yarmouk, at shallow horizons (mostly at Wadi Sir-A7 and Amman-B2 formations aquifers) this hot flow component mixes with a shallow cooled flow component originating from the South, before discharging at the outlets.

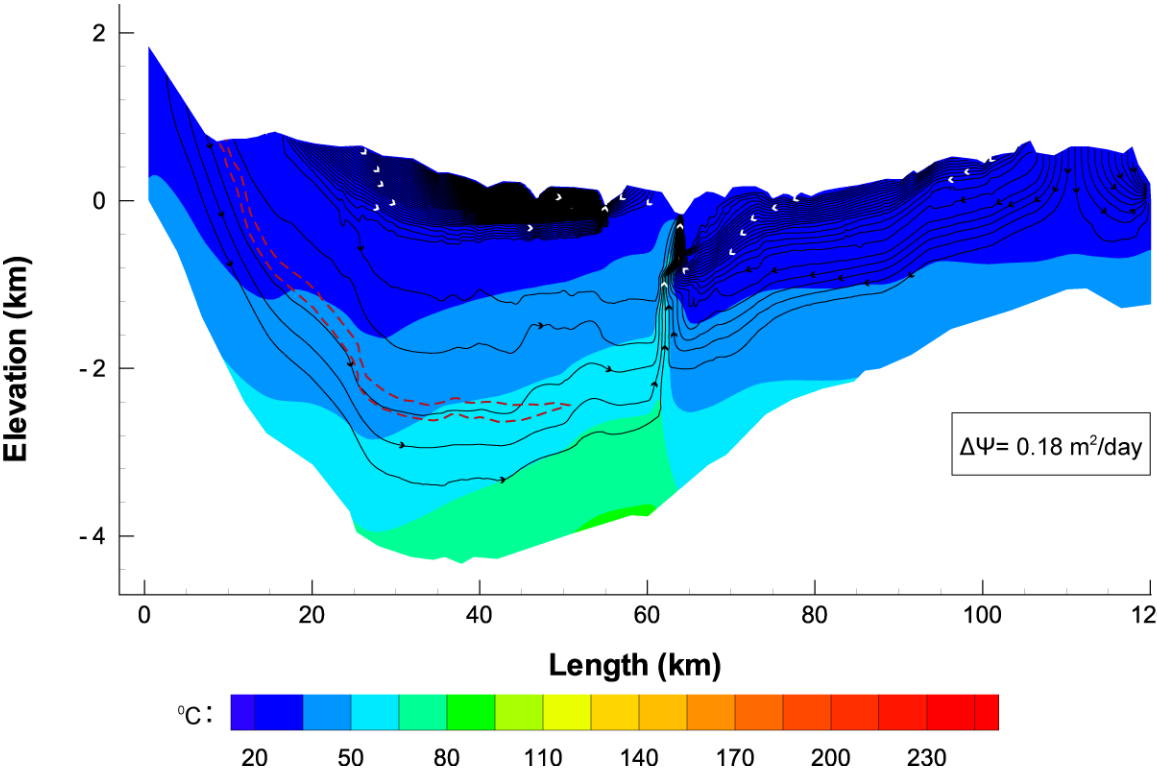

Figure 13. Temperature map and streamlines for scenario 1; Δψ represents volumetric flux between streamlines; dashed red line marks Kidod Fm. position.

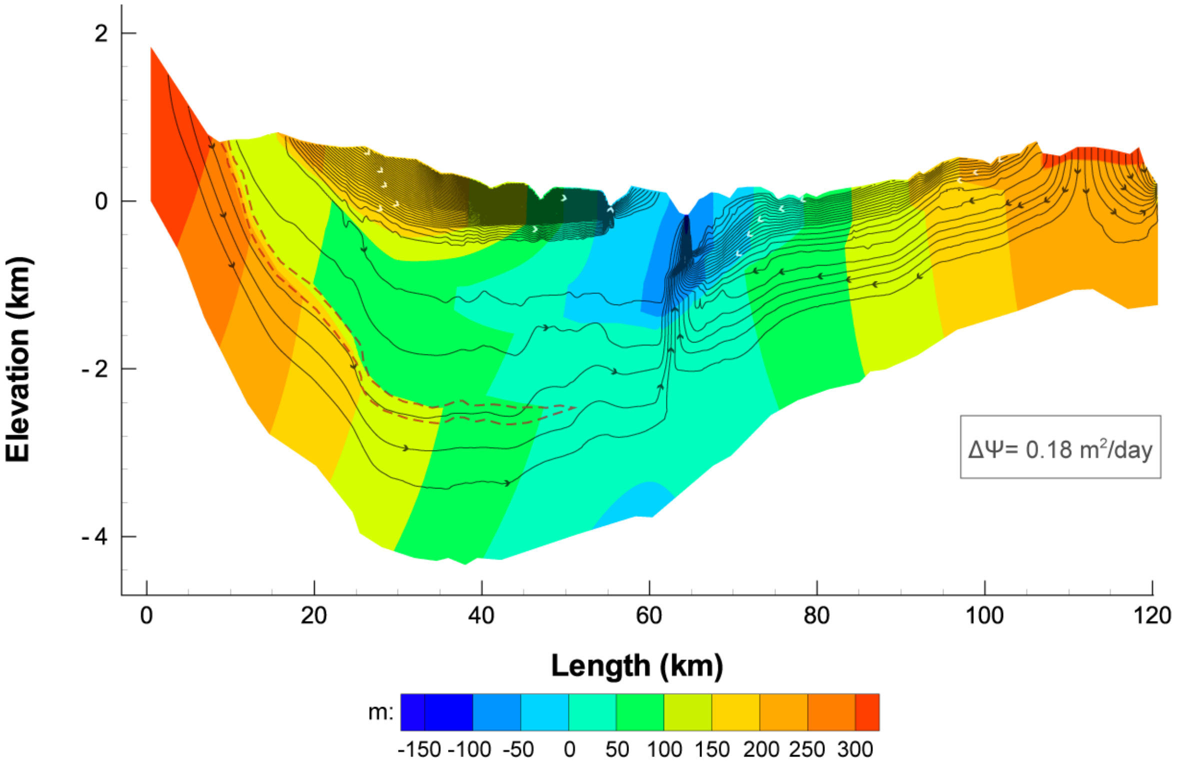

Figure 14. Head map and streamlines for scenario 1; Δψ represents volumetric flux between streamlines; dashed red line marks Kidod Fm. position.

As shown in Fig. 15 (purple line), temperatures are significantly lower and inconsistent with depth-temperature field measurements below the LYG (black squares). Results for this scenario undermine the hypothesis that encountered heat at the LYG may be explained solely by a deep forced convection flow component originating in the Hermon, under normal regional basal heat flow.

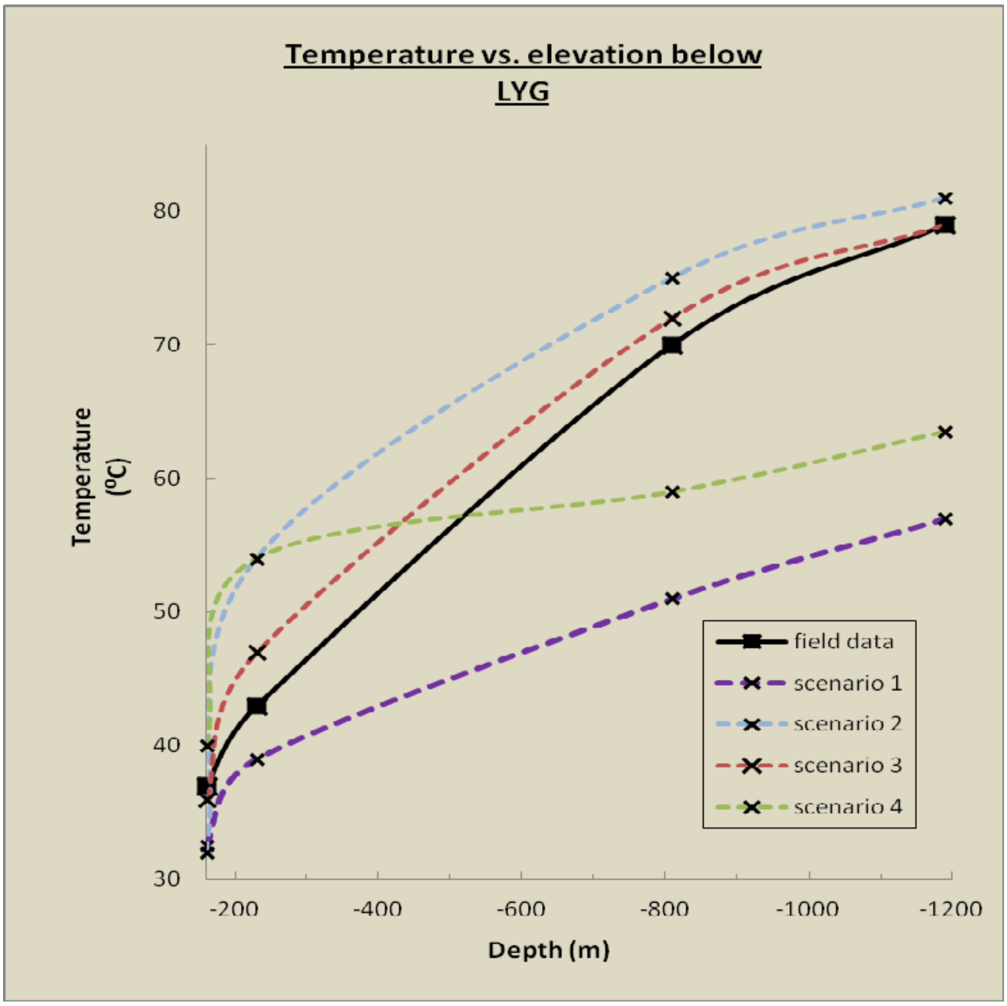

Figure 15. Temperature vs. elevation of the section below LYG, field data and model scenarios; field data presented in Table 10.

Table 10. Temperature-depth field data from LYG; ¹- outflow mean temperatures of the LYG Springs, see Table 3, ²-Mero and Rozner (1984), ³- Michelson (1981).

no. of point	**elevation asl (m)**	**Temperature (^{o}C)**	**Head (m)**
1[1]	-160	36-38	-160
2[2]	-230	43	-2.4-35
3[2]	-810	Above 70	-32—52
4[3]	-1190	79	0

The second scenario was set to test the second hypothesis- that the heat anomaly of the LYG may be explained by a high basal heat flow value at the GH without any significant deep forced convection in that area. As expected, the high heat flow induces evolution of free convection cells (figures 16 and 17; closed streamlines beneath the GH), which are mostly separated by aquiclude Kidod Fm. (the 3-D nature of the convection cells is neglected).

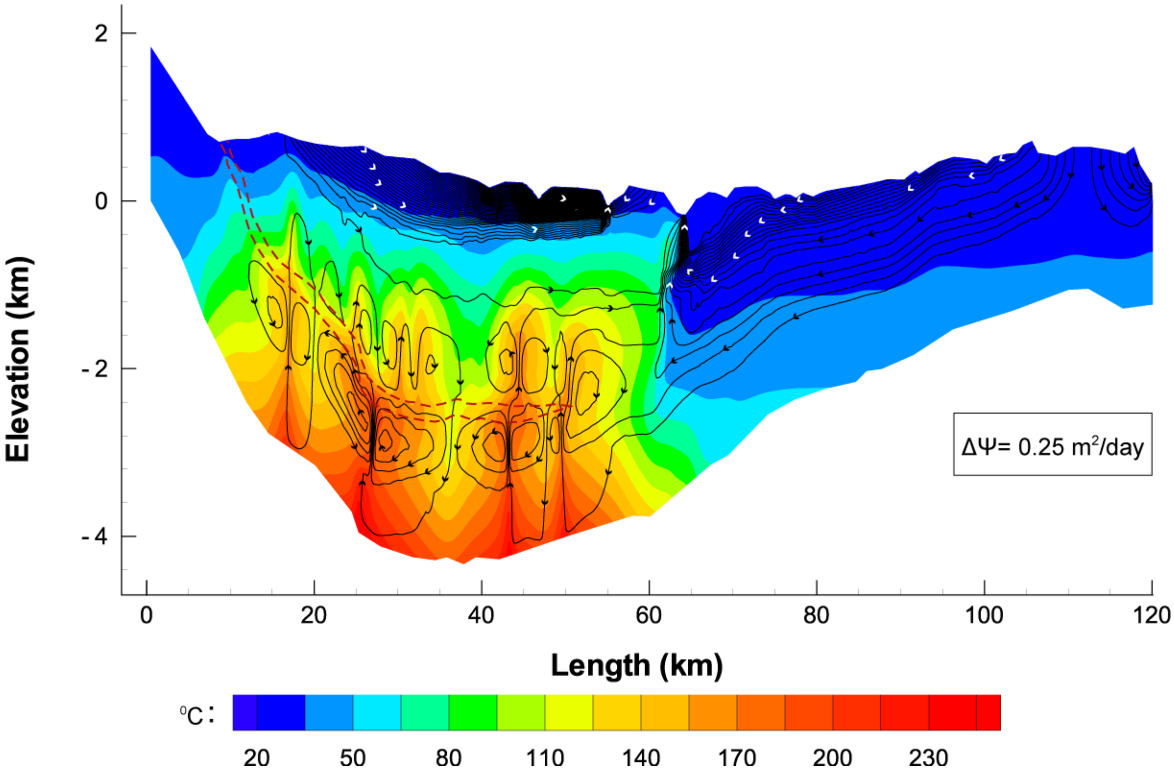

Figure. 16. Temperature map and streamlines for scenario 2; Δψ represents volumetric flux between streamlines; dashed red line marks Kidod Fm. position.

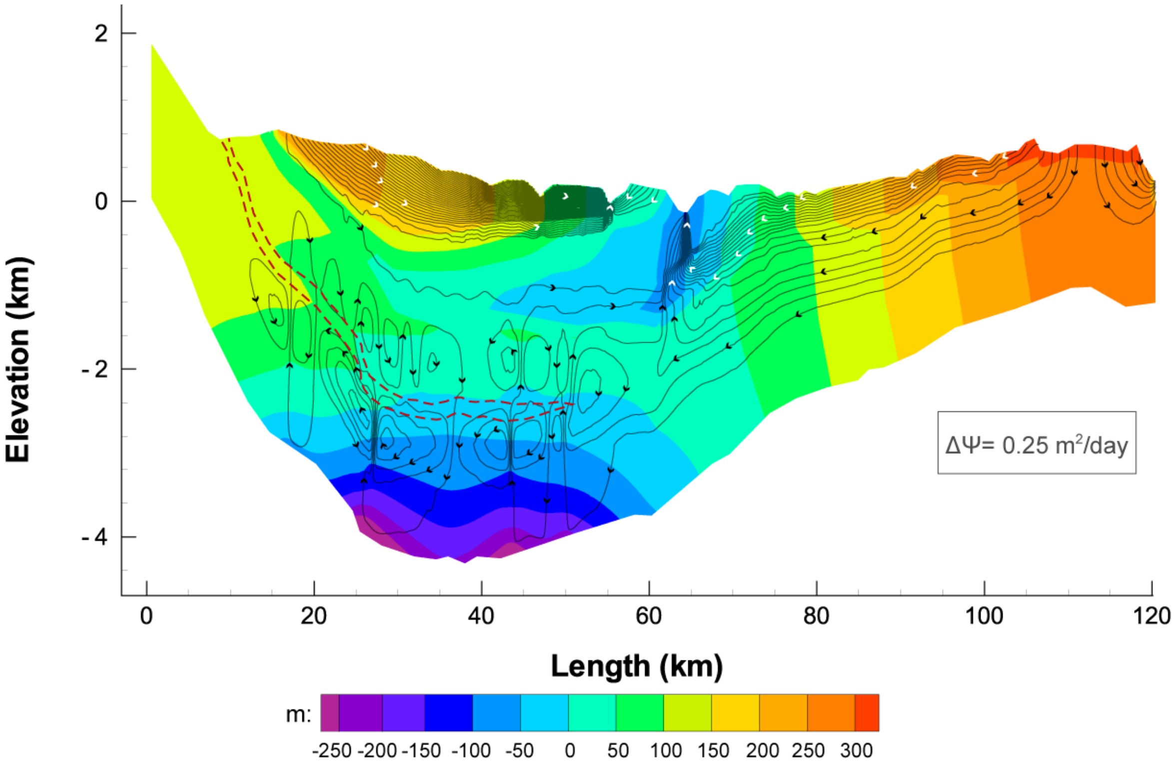

Figure 17. Head map and streamlines for scenario 2; Δψ represents volumetric flux between streamlines; dashed red line marks Kidod Fm. position.

Results of this scenario indicate that such a hydrothermal configuration does not exist, mostly since simulation results show shallow thermal expression beneath the GH (isotherm of 30°C typically at a depth of 250 m), which does not exist (Table 4). Also, the very high heat flow value required to satisfy thermal observations below the LYG- above 200 mW/m^2- appears unlikely to exist in this area.

An oscillatory convection regime is observed in the solution (Fig.18), compatible with convection regime identified in Horton–Rogers–Lapwood linear stability analysis, when reaching the second critical value of thermal Rayleigh-Darcy (Ra) number (further in section 5.4) (Nield and Bejan, 2006).

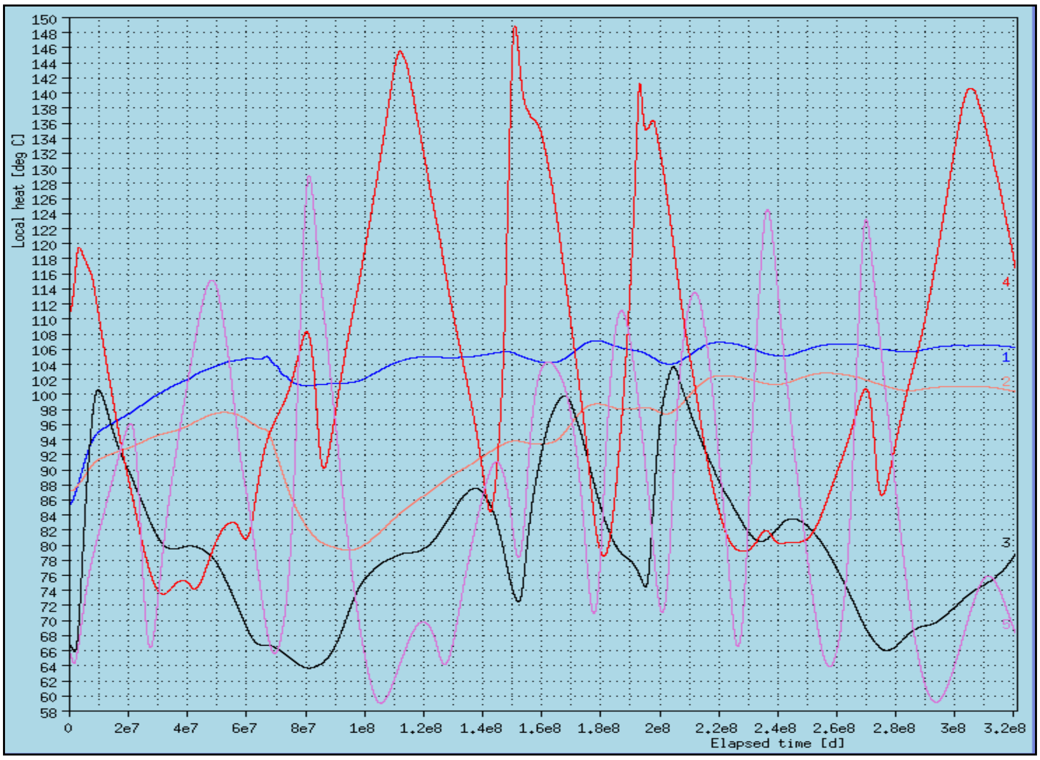

Figure 18. Temperature vs. time of arbitrary points below the GH (below unit 10) of scenario 2, oscillatory regime is being observed.

The third scenario considers a combination of the conditions: a flow component originating in the Hermon (as in scenario one) and an elevated basal heat flow value beneath the GH. For this scenario the heat flow value at the lower boundary beneath the GH was modified until a good fit to temperature data was achieved (Fig. 15). A minimal value of 100 mW/m^2 was required. Results for this scenario present a good fit to all existing thermal data of the study area.

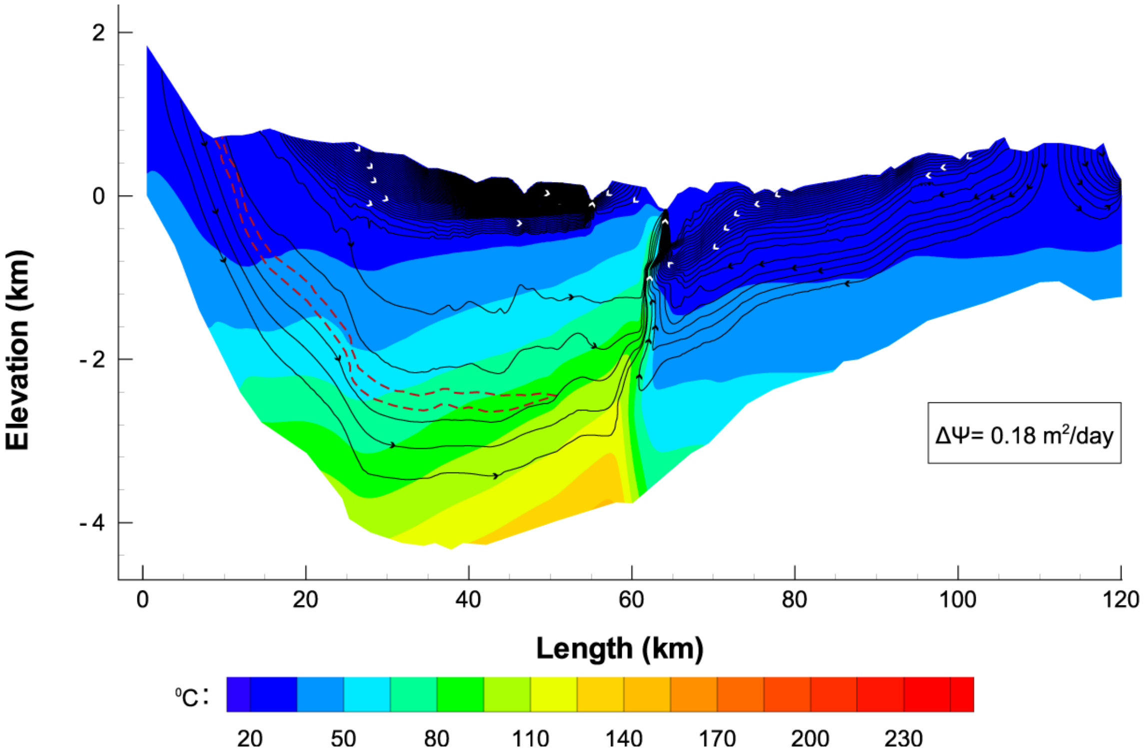

Figure. 19. Temperature map and streamlines for scenario 3; Δψ represents volumetric flux between streamlines; dashed red line marks Kidod Fm. position.

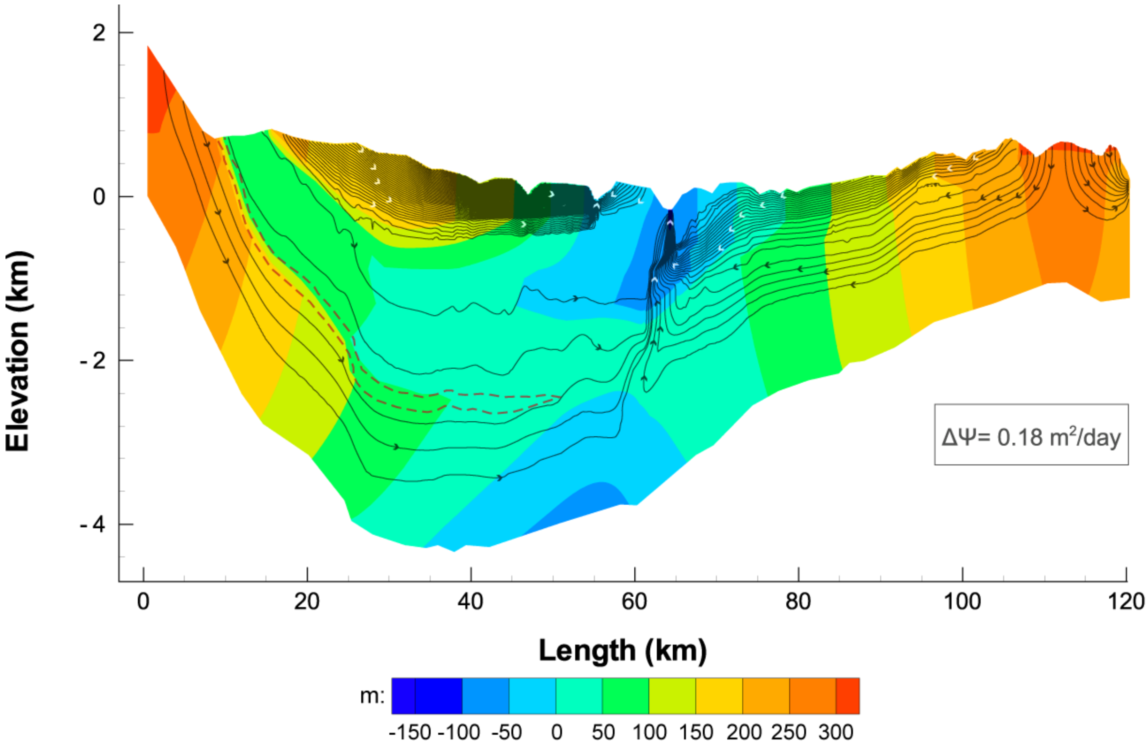

Figure 20. Head map and streamlines for scenario 3; Δψ represents volumetric flux between streamlines; dashed red line marks Kidod Fm. position.

The hydrothermal configuration in this scenario causes a considerable part (~45% according to numerical energy calculation) of basal heat flow to be transported by convection to the LYG outlets and the remaining elevated basal heat flow is transferred (mostly through conduction) to more shallow layers and to the surface. In addition, the constant percolation of cool water and massive groundwater replacement in the basaltic aquifer also cause temperatures to be low at the shallow depth. Similar geothermal behavior was described by Eckstein and Simmons (1978) for regions in Israel affected by groundwater movement and recharge.

In this scenario the southward flow component originating in the Hermon is large enough to suppress any free convection, except in the upwelling area beneath the Yarmouk, where a mixed convection mechanism prevails (to be discussed further). The high basal heat flow value deduced- 100 mW/m^2 - is higher by a factor of 2-2.5 than the estimated mean basal heat flow value in the region, and is also high compared to the estimated world mean terrestrial basal heat flow value (60 mW/m^2).

The fourth scenario demonstrates that very high recharge in the Hermon would cause a deep forced convection flow component that would cool the deep section (Fig. 21). In this case, simulation results fit field data very poorly (green line in Fig. 15). At greater depths (-500 to -1,170 m) temperatures are considerably lower than field data and at shallow depth temperatures are considerably higher. This behavior may be attributed to pronounce cooling of a smaller flow component by conduction heat loss to the surrounding lithology, during upwelling (scenario 3).

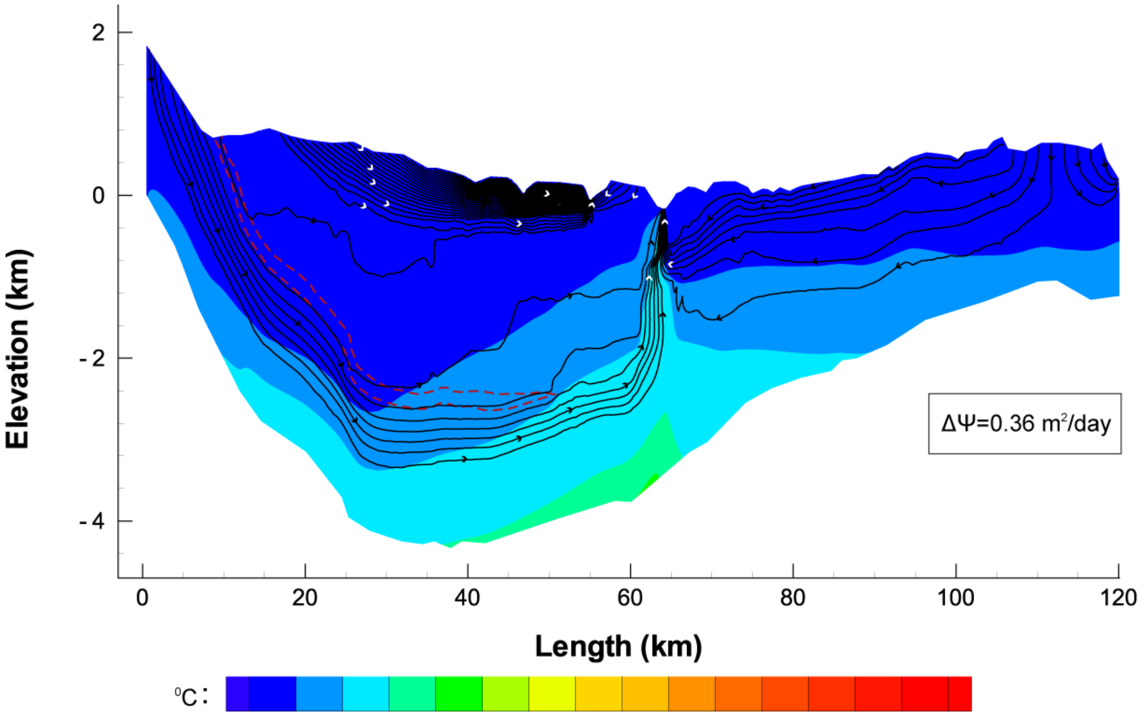

Figure 21. Temperature map and streamlines for scenario 4; Δψ represents volumetric flux between streamlines; dashed red line marks Kidod Fm. position.

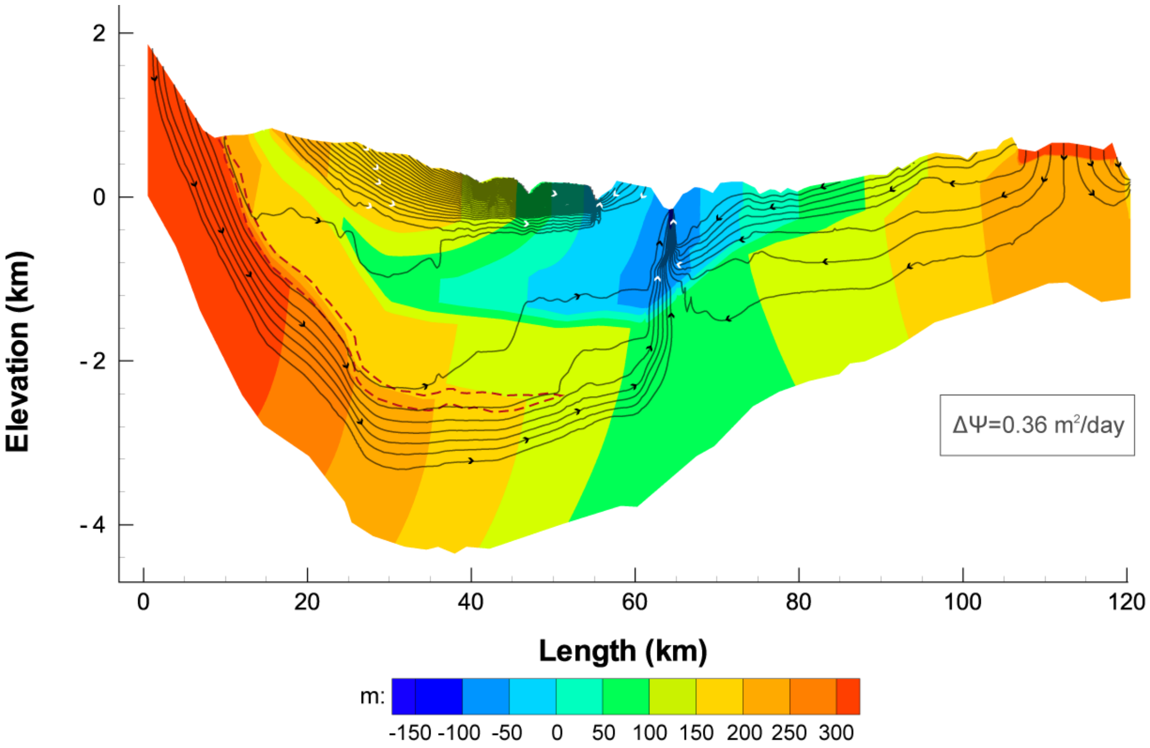

Figure 22. Head map and streamlines for scenario 4; Δψ represents volumetric flux between streamlines; dashed red line marks Kidod Fm. position.

Comparison of the scenarios tested indicates that only the configuration combining deep transportation of heat by Hermon origin flow component with elevated basal heat flow beneath GH as in scenario 3 can satisfy thermal field observations. As such, further analysis and discussion will focus on scenario 3.

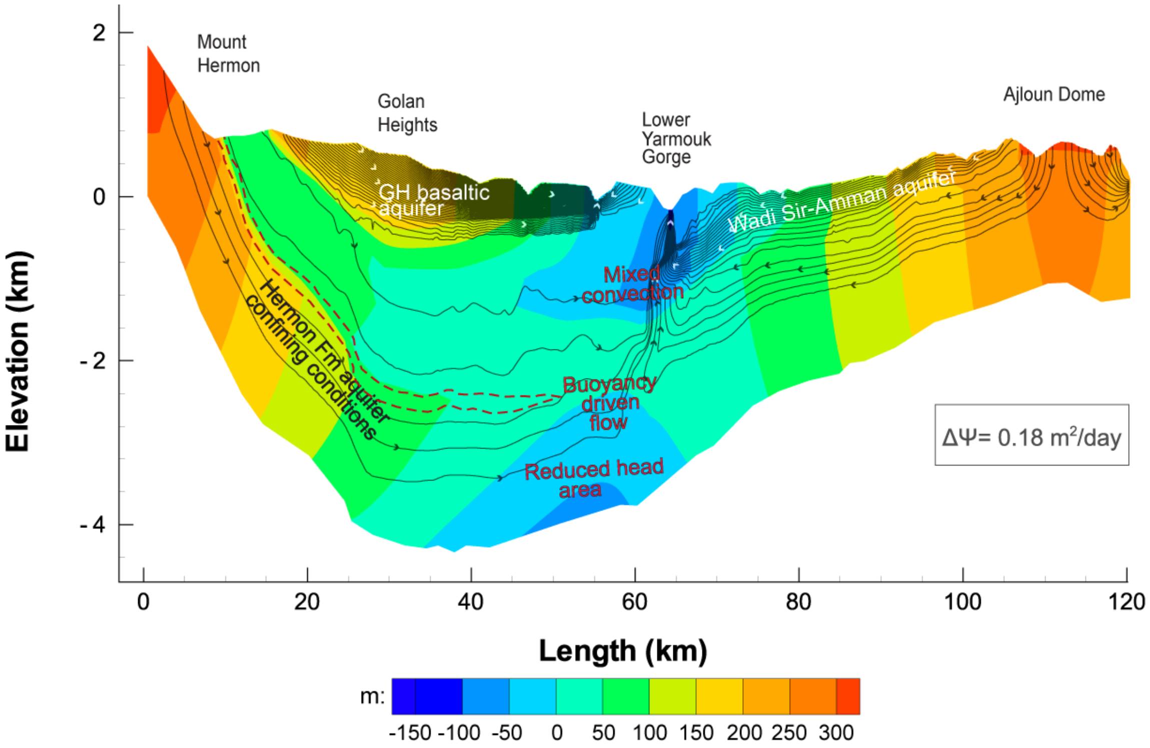

Figure 23. Head map and streamlines for scenario 3, with remarks; Δψ represents volumetric flux between streamlines; dashed red line marks Kidod Fm. position.

Streamlines and Head map (Fig. 23) are in agreement with the known hydrological field data described in section 2.3. At the Ajloun Ridge the nature of Wadi Sir Fm. and Amman Fm. aquifers (units 7 and 9) and the aquitard unit 6 (Ajloun Gr., units 3-6), dictates that the majority of groundwater flow in the ridge concentrates in Wadi Sir Fm. and Amman Fm. aquifers (units 7 and 9). Though some extent of deeper flow is expected (Bajjali et al., 1997) and may be observed mostly at Kurnub Gr. (unit 4) and Naur Fm. (unit 5). Further north, toward the LYG, the deep and shallow flows (Wadi Sir Fm. and Amman Fm. aquifers) at the Ajloun Ridge become completely confined by Wadi Ghudran Fm. (unit 8) and Belqa Gr. (unit 10). As evident in most of the wells at the LYG, beneath the LYG artesian conditions are observed.

Northward in the shallow section of the GH, the dense streamlines exhibit extensive shallow detached circulation at the basaltic aquifer. At Hermon Fm. aquifer (unit 2) and the aquitard beneath (unit 1), groundwater head is indicative of confining conditions and is considerably higher than at the aquifer units above aquiclude Kidod Fm. (unit 3). Southward, beneath the LYG, in the upwelling area where Kidod Fm. terminates, there is extremely low head conditions attributed to low pressure resulting from elevated temperatures and a lower density of the groundwater column above.

The upwelling flow path through that reduced - head area, indicates that groundwater flow there is strongly buoyancy driven (natural convection). Further upward beneath the LYG head increases and then decreases toward LYG outlets, where a mixed convection mechanism prevails- involving both gravity driven (forced or head-driven convection) and buoyancy driven flow*.

More hydrological and geological insight is given by model calibration and the field observation that the hot spring water of the LYG is discharged from formations known to be aquitards and aquicludes in other areas, implies that the section below the LYG is permeable and highly fractured. Results of the current model’s calibration to flow and heat data indicates that the aquiclude or aquitard units beneath the LYG have vertical permeability 1-3 orders of magnitude greater than in other areas.

***In Darcy's law (Eq. 2) buoyancy forces are represented by the buoyancy term and gravitational forces are expressed by the head gradient term.**

$$q = (k\rho_0 g / \mu)(\underbrace{\nabla h}_{\substack{hydraulic \\ gradient}} + \underbrace{\frac{\rho - \rho_0}{\rho_0} \nabla z}_{\substack{bouyancy \\ term}}) \qquad (42)$$

Another possible explanation for the heat anomaly could be deep heat transportation from larger areas, under standard basal heat flow conditions (50 mW/m^2). The area (A) of standard heat flux (J=50 mW/m^2) required to produce the amount of energy released at the LYG (U=90.72 MW) if 50% of heat is transported to the LYG outlets is (45% according to scenario 3):

$$A = U * 2 / J = 90.72 * 10^6\,(W) * 2 / 0.05 (W/m^2) = 3630\,(km^2) \qquad (43)$$

This calculation reveals that in order to transport heat under normal basal heat flow values and deep circulation (2-3 km), groundwater flow from an area of ~3,600 km^2 is required. The Eastern part of the area known as Eastern Huaran region (the Huaran region includes the GH), similarly to the GH, is mostly a volcanic plateau. In the Southern part of the Huaran is Jebel Al-Druze Ridge (1,800 m, ~100 km from the LYG), which is contained within a large tectonic depression. In that area extensive Neogene-Quaternary volcanic activity took place, including considerable Holocenean activity (Razvalyaev et al., 2005). This would make the Eastern Huaran a potential candidate for a heat source for the anomaly of the LYG, both by deep transportation of heat from a large area, and also as a potential source of exceptional geothermal heat. Unfortunately, lack of basic structural, stratigraphycal and hydrological data precludes testing of this possibility.

We must also consider the validity of our 2-D treatment of the problem. As the shallow groundwater flow has very little impact on heat distribution, the tested deep convection is approximately in the plane of the model's cross section, and the obvious accepted trends between model scenarios, model results concerning trends should be regarded as applicable, but less so regarding exact value estimations. For better estimation of basal heat flow and volumetric flow rate components, 3-D modeling is required.

5.3. Sensitivity analysis

Considerable uncertainties, regarding the values of some parameters, appear in the mathematical model, indicating the need for sensitivity analysis, for the purpose of assessing the possible effect of parameter variations on model results (scenario 3).

As model simulations were mostly for steady state, parameters which appear in non-steady terms are of essentially no importance. Properties of water are also fairly well estimated. Thus, the parameters that must be analyzed for sensitivity are thermal conductivity (λ) and intrinsic permeability (k).

Based on experimental data of thermal conductivity (Čermák and Rybach, 1982; Clark, 1966), the effect of increasing and reducing thermal conductivity by 20% of the primary value was tested. The permeability parameter was generally calibrated according to groundwater level maps, but still poses some uncertenty, mostly due to the 2-D nature of the model. Model sensitivity to permeability values was tested by increasing and reducing it 5 fold from the calibrated value. Effect of parameter variation was tested for each parameter separately, as well as in conjunction. The following was inferred:

i. increasing thermal conductivity value by 20% required setting heat flow of 120 mW/m^2 beneath the GH in order to satisfy temperature data.

ii. reducing thermal conductivity value by 20% required setting heat flow of 85 mW/m^2 beneath the GH in order to satisfy temperature data.

iii. Reducing permeability of the lower model units (1-6) by a factor of 5 required setting slightly elevated heat flow beneath the GH (~5 mW/m^2) to satisfy temperature data.

iv. Increasing permeability of lower model units (1-6) resulted in the appearance of convection cells (Fig. 24) with cosequent high heat conduction to the surface. One possible way to avoid this increased conduction to the surface is to increase the flow component from the Hermon Ridge in order to supress the convection cells (by the cooling effect). However, this configuration would eventually result in poor fit to known temperature data, as well as an increased heat flow value beneath the GH (~150 mW/m^2).

v. Increasing both permeability and thermal conductivity resulted, similarly to results when only permeability was varied, in poor fit to known temperature data, as well as an increased heat flow value beneath the GH.

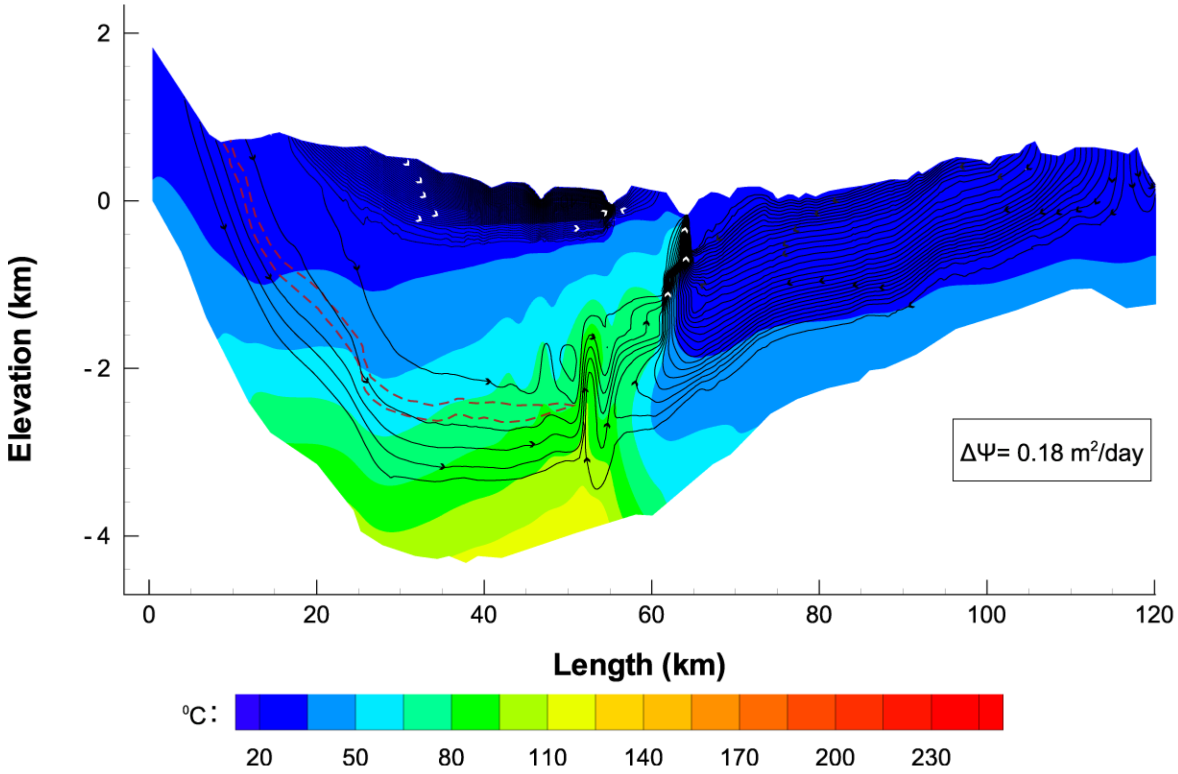

Figure 24. Temperature map and streamlines of sensitivity analysis of scenario 3; units 1-6 permeability increased by a factor of 5; Δψ represents volumetric flux between streamlines; dashed red line marks Kidod Fm. position.

Thermal conductivity determines the partitioning of heat transferred to the surface, and to the LYG outlets. Increasing thermal conductivity results in more heat being transferred by conduction to shallow layers and to the surface, resulting in a higher estimated heat flow required to satisfy temperature data. Reducing thermal conductivity results in the opposite effect and lower estimated heat flow.

Permeability value estimation of the lower model units mostly affects on the appearance of natural convection and also on larger deep flow extent beneath Ajloun Ridge (Fig. 24). Reduced permeability value in scenario 3 results in the appearance of convection cells. The convection cells result in a larger amount of heat being transported by conduction to shallow layers and to the surface and a reduced amount of heat to be transferred to the LYG outlets, resulting in high estimated basal heat flow beneath the GH. If a larger Hermon origin flow component is set, convection cells are supressed (by the cooling effect), but again greater heat flow is required to heat this larger flow component, once again resulting in higher heat flow and bad fit temperature data.

Summarizing, the most important effect is thermal conductivity value, reducing thermal conductivity by 20% results in heat flow of 85 mW/m^2 instead of 100 mW/m^2. Additional possible reducing heat flow effect is reduced permeability of the lower units in the southern side (beneath the Ajloun), such a reduction in permeability results in larger extent of deep flow and more transportation of heat to the LYG outlets from south (Fig. 24), but that effect is small and results in lower estimated basal heat flow value beneath the GH of ~5 mW/m^2. Combining both effects the sensitvity analysis results indicate on lower limit basal heat flow value beneath the GH of 80 mW/m^2 and most of all that simulation results are independent of arbitrary chosen parameters. As expected Reduced permeability beaneath GH results in appearens of natural convection and transportation of heat to shallow layers resulting in higher estimation of the basal heat flow beneath the GH (~150 mW/m^2) and poor fit to known temperature data.

5.4. Natural convection analysis

Insight into the nature of free convection is given by results of the extensively analyzed Horton–Rogers–Lapwood problem. The problem is the Porous-medium analog of the Rayleigh-Benard cellular convection problem, including linear stability analysis of an infinite horizontal porous layer uniformly heated from below. Main assumptions include: homogeneous and isotropic porous media, validity of Darcy's law and the OB approximation, as well as constant thermal expansion coefficient β and viscosity μ.

The analysis leads to the dimensionless thermal Rayleigh-Darcy (Ra) number, whose critical value determines onset of convection and transition from a conductive to a convective regime. Ra defined as (Nield and Bejan, 2006):

$$Ra = \frac{\rho_0 g \beta \Delta T k Z}{\mu D_\lambda} \quad with\ D_\lambda = \|\lambda_e\| / \rho_0 c \tag{44}$$

Where ΔT is the vertical temperature difference, k permeability and Z vertical length.

Few major convection regimes have been identified in later studies (Caltagirone et al., 1981; Straus, 1974; Nield and Bejan, 2006): pure conduction $<Ra_{c1}=4\pi^2<$ stable natural convection $<Ra_{c2}\approx 240$-390*$<$ unstable (oscillatory) natural convection.

Extensions of the problem include more realistic physical assumptions considering geothermal systems, e.g. anisotropic and layered porous media, non OB fluid and viscosity and thermal expansivity dependence, 3-D analysis, different boundary conditions, and also a modified Ra criterion-effective Ra (Nield, 1994; Beck, 1972; Straus and Schubert, 1977; Nield and Bejan, 2006). However, due to the complex flow pattern, the geometric complexity, the multi layering, orders variation by orders of magnitude in permeability values of the different layers and additional complexities it is doubtful whether analysis based on Ra number (or effective Ra number) will result in any contribution here.

Nevertheless, it appears that the different convection regimes accepted in the numerical analysis correspond to the regimes identified in the Horton–Rogers–Lapwood analysis in the following way: in scenarios 1 and 4 we deal mostly with the first range of Ra ($<Ra_{c1}$- conduction), in scenario 3 Ra is within the second range ($>Ra_{c1}$- stable convection) and the oscillations in scenario 2 (Fig.17) are attributed to the third range of Ra ($>Ra_{c2}$- unstable convection) (a rough estimation of orders of magnitude does not contradict the identified regimes).

---

*

Perturbation approach solutions (390) and numerical solutions (240-300) showing different results (Nield and Bejan, 2006).

5.5. Numerical software comparison

Initially, COMSOL Multiphysics software was used for simulations. Similar to FEFLOW, COMSOL is also a commercial numerical FEM software package, seemingly equipped to solve hydrological and geothermal related problems (among other physical and engineering problems). Through work stages it was revealed to be unreliable for the analysis required here, and its solutions were inaccurate. Versions 3.5a and 4.2 (newest up to date) of COMSOL were tested.

- *The solved equations*- as indicated in sections 3.1 and 3.11, the thermal energy balance equation (Eq. (29)) solved by all COMSOL versions as well as FEFLOW is identical. The mass balance equation solved by COMSOL version 3.5a involves the OB approximation and may be inadequate in the context of the current case study (results of this version are not presented here). Concerning mass balance equations solved by FEFLOW and COMSOL version 4.2, as indicated, there are insignificant differences concerning current case study. Following, in that section the differences that may be attributed to viscosity and density correlations are discussed.

- *Convergence problem*- convergence problems arose during model construction and heat addition. The convergence problems were finally solved by limiting the time step and solving the model in three steps, each time increasing the maximum time step.
- *Inaccurate solution*- After a solution was reached it was revealed to be unreliable by different criteria:
  1. Unreasonably high basal heat flow at the GH was required to satisfy the temperature data- 140 mW/m^2 (Fig. 27). Such a high value is inconsistent with observations in geothermal systems studied at other locations worldwide, meaning that the expected shallow and surface expression is much more pronounced, for such high heat flow value.
  2. Instabilities appeared (e.g. in the bottom right corner of Figs. 26 and 27).
  3. Results of numerical total balances for mass and energy were mostly poor, yielding deficits of ~40% for thermal energy and ~20% for mass, whereas for FEFLOW results yielded <1% deficit for mass balance. This indicates poor quality of numerical calculations and a large numerical error.
- *Results comparison*- Comparison between temperature maps of scenario 3 solutions by FEFLOW (Fig. 25) and COMSOL (Fig. 26 for 100 mW/m^2 and Fig. 27 for 140 mW/m^2 beneath the GH) reveals that the general temperature trend of the solution is similar but quantitatively results are very different. The accepted solution by COMSOL satisfied the temperature data only when setting a heat flow value of 140 mW/m^2 beneath the GH, a 40% increase in basal heat flow value

estimation compared to the accepted estimation by FEFLOW. Note also the instability which appears at the lower right corner of fgures 26 and 27.

Comparison between head maps of scenario 3 solutions accepted by FEFLOW (Fig. 28) and COMSOL (Fig. 29 for 100 mW/m^2 and Fig. 30 for 140 mW/m^2 beneath the GH) also reveals, as the temperature maps did, similar trends but a large quantitative difference.

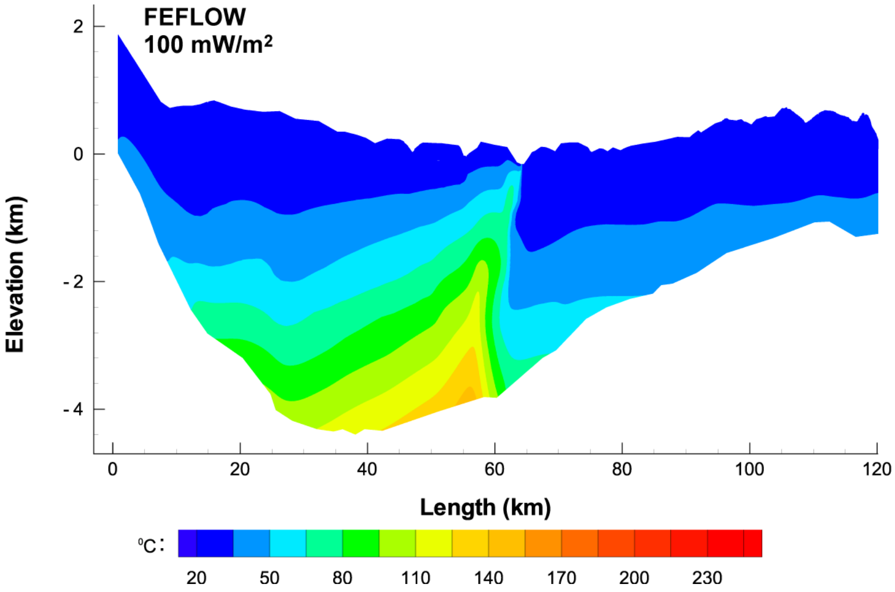

Figure 25. Temperature map for scenario 3, heat flow beneath the GH is 100 mW/m^2; solution by FEFLOW.

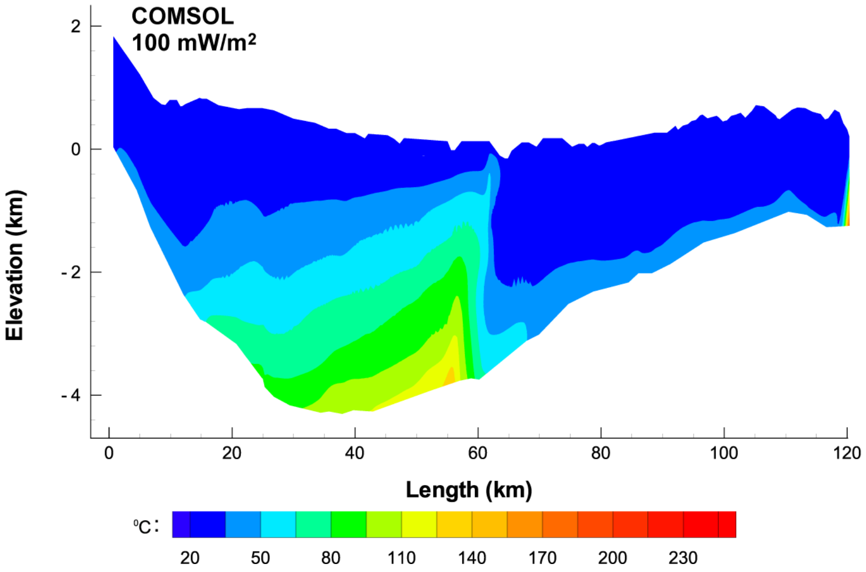

Figure 26. Temperature map for scenario 3, heat flow beneath the GH is 100 mW/m^2; solution by COMSOL. The small scale peaks are related to the presentation software rather than COMSOL.

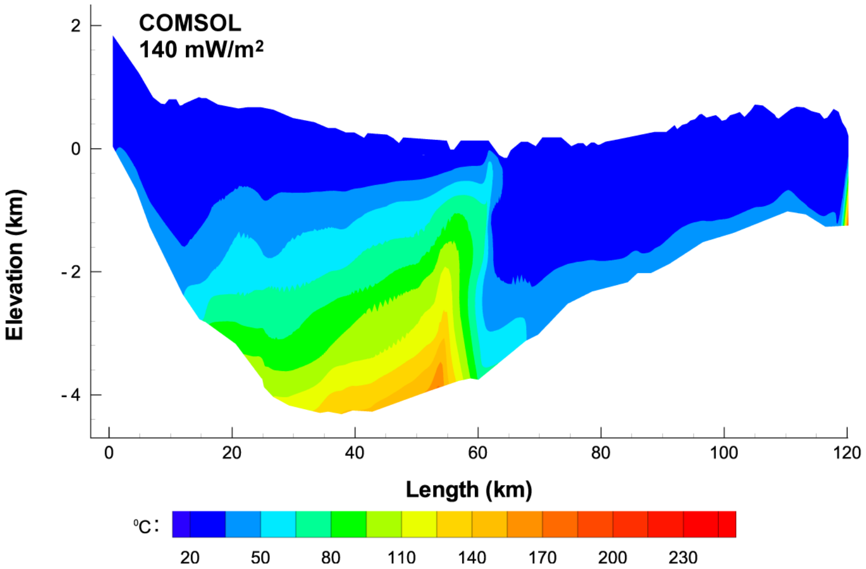

Figure 27. Temperature map for scenario 3, heat flow beneath the GH is 140 mW/m^2; solution by COMSOL. The small scale peaks are related to the presentation software rather than COMSOL.

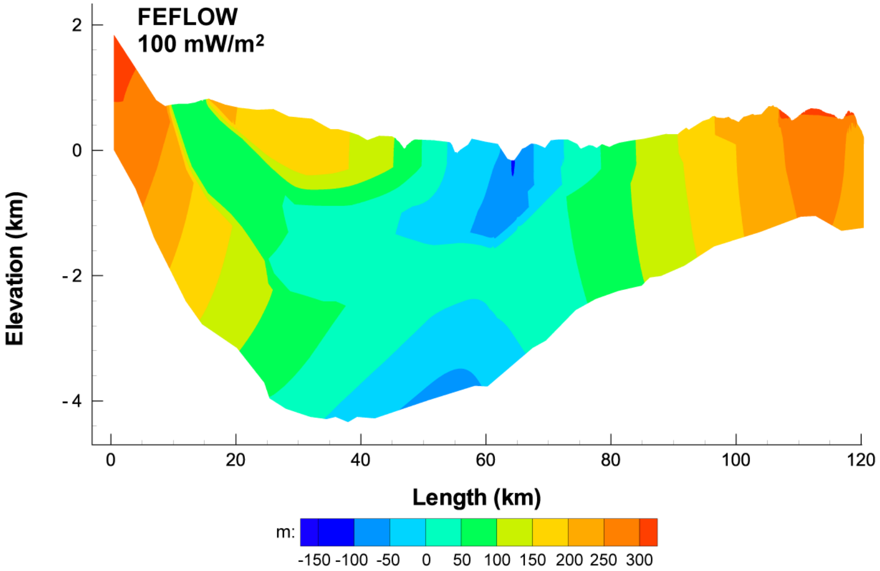

Figure 28. Head map for scenario 3, heat flow beneath the GH is 140 mW/m^2; solution by FEFLOW.

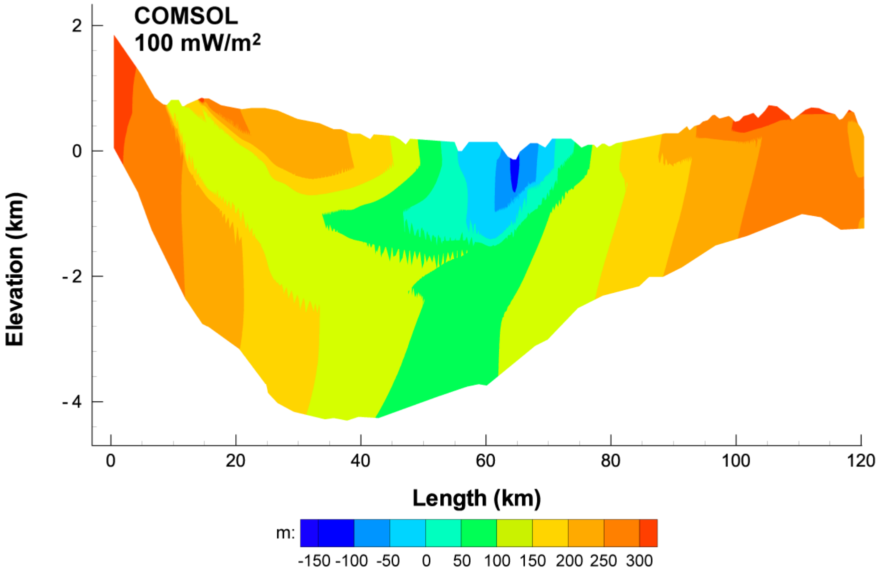

Figure 29. Head map for scenario 3, heat flow beneath the GH is 100 mW/m^2; solution by COMSOL. The small scale peaks are related to the presentation software rather than COMSOL.

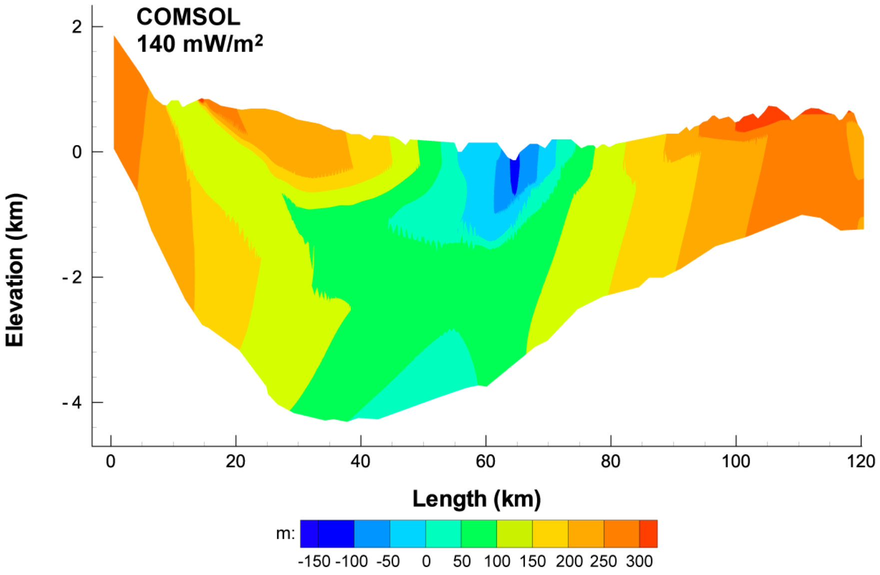

Figure 30. Head map for scenario 3, heat flow beneath the GH is 140 mW/m^2; solution by COMSOL. The small scale peaks are related to the presentation software rather than COMSOL.

- *Testing effect of mesh quality*- Mesh refinement at different configurations did not improve the solution or balance results. The presented results include 95,000 elements (the FEFLOW model was solved with 60,000 and showed consistent solutions even at lower mesh densities).
- *Viscosity and density correlations*- some possible differences attributed to viscosity and density correlations were tested. The correlations set in COMSOL are of Watson et al. (1980), Philips et al. (1981) and Philips et al. (1983). These correlations take into account both pressure and temperature conditions. Comparison of correlation results to experimental data (Appendix Tables) yields a maximum deviation at the relevant pressure, temperature range of a few percentage points at most (<4%). Also, setting different correlations in COMSOL showed that the maximum deviation in heat flow estimation that can be attributed to the correlation errors is no more than 10 mW/m^2 at most.
- *Interface and model setting*- Model geometry, parameter values and boundary conditions are in proximity identical for both software packages. Only negligible differences related to different software interfaces, and methods of parameter and boundary condition assignments exist, but such minor differences cannot explain the large difference in results.

6. Summary and conclusions

Combining existing geological, hydrological and thermal data of the Golan-Ajloun area in numerical simulations and thermal energy balance, reveals that satisfying the hydrothermal field observations in the area requires: a) existence of an exceptional source of geothermal heat in the GH area, and b) existence of a deep (~3 km) small forced convection flow component originating at Hermon Ridge and discharges at the LYG outlets.

Other tested configurations of flow and heat were rejected base on pronounced incompatibility to field data:

I. Considering only deep heat transportation of Hermon origin resulted in a substantially cooled heat anomaly at the LYG, as indicated both by simulation and energy balance calculation results, and it was determined to be an insufficient factor by itself to produce the shallow heat anomaly of the LYG.

II. Considering an exceptional heat source alone has been ruled out for the following reasons: 1) The exceptional heat source would also manifest itself in shallow thermal expression, such expression not in evidence at the GH, and 2) the extreme heat flow required (>200 mW/m^2) is unlikely to exist in that area.

III. Simulation results indicating that the involved deep flow component is only a minor part of the discharging groundwater at LYG. Simulations involving a large flow component of Hermon origin are inconsistent with field thermal data, as the thermal gradient is very mild in comparison with the field measurements of the gradient below the LYG, indicating that the deep flow component is expected to be small- only a few MCM/yr, compared with the overall groundwater discharge through the LYG outlets (45 MCM/yr), where the main water sources of the LYG outlets are the shallow (A7 and B2) flow components of Ajloun origin, as also suggested by most previous hydrological studies.

The small deep flow component serves as a fundamental heat convection component, and transports heat from a great depth (~3 km) and a vast area beneath the GH, and significantly affects hydrothermal patterns. This deep circulation is causing a considerable part of the basin's elevated basal heat flow to be discharged through the LYG outlets, and prevents significant shallow thermal expression at the GH.

The accepted basal heat flow value of the GH is 100 mW/m^2. This value is higher by a factor of 2-2.5 than the estimated mean basal heat flow value of the region, indicating that the shallow thermal anomaly of the LYG is an expression of a deep crust geothermal anomaly. Performed sensitivity analysis resulted in a lower limit estimation of the basal heat flow beneath the GH to be 80 mW/m^2. That value is attributable less to existing conditions, including reduced thermal conductivity and reduced permeability of the lower units beneath the Ajloun Ridge, but mostly indicating that simulation results are independent of arbitrary chosen parameter values.

Doubts over model results may be raised due to its 2-D nature. However, considering that the tested deep convection regime is approximately in the model's cross section plane, and the obvious resulting trends between model scenarios, model results should be regarded as applicable for qualitative analysis of trends.

Regarding the area east to the Golan-Ajloun, Eastern Huaran, unfortunately lack of basic geological and hydrothermal data precludes meaningfully detailed analysis. However, the elevated Jebel Al-Druze Ridge and the involved Holocenean activity there would make the Eastern Huaran a potential candidate for explaining the hydrothermal anomaly of the LYG, both by deep transportation of heat from a large area, and also as a potential source of exceptional geothermal heat, as a similar configuration to that suggested in the Golan-Ajloun region may be involved. Thermal energy balance calculations assisted by the simulation outcome involving indicates that combining all available areas for deep heat transportation from Eastern Hauran, the GH and the Ajloun Ridge (~3,600 km^2) the heat anomaly of the LYG may be explained by deep heat transportation under average basal heat flow (50 mW/m^2).

Despite the different geothermal configurations, and possibile flow components' origins, the combination of high temperatures at relatively shallow depth (~130^{o}C at 3 km depth) and a large artesian groundwater reservoir existing below the LYG may be adequate for geothermal utilization, which can also take place within the green line.

Analysis of the geothermal system of the Golan-Ajloun area indicates conclusively that deep groundwater transportation takes place. While this transport collects heat from a vast area, it constitutes a rather minor component of overall flow flux. As in other studies, analysis of heat patterns proved to be a good groundwater tracer (Anderson, 2005).

Comparison to numerical results shows that the geothermal Pe number is a good measure for rough estimation of conduction and convection mechanisms ratio and evaluation of hydrological basins' thermal state, but only as long as the velocity can be estimated without relying on hydraulic conductivity estimations. The Rayleigh-Darcy (also effective Rayleigh-Darcy) number was found to be impractical here for a rough estimation of convection regimes, mostly due to multi layering, flow pattern complexity, and large uncertainty of hydraulic conductivity. Having said that, note that the various natural convection regimes indicated in literature were identified in model scenarios.

COMSOL multyphysics commercial software package was tested, and found to be inadequate for analyzing basin-scale geothermal systems, while the FEFLOW software package, as indicated in previous studies, exemplified greater stability and solution consistency throughout all work stages.

7. References

Abdulagatov, I.M., Emirov, S.N., Abdulagatova, Z.Z., Askerov, S.Ya. (2006). Effect of pressure and temperature on the thermal conductivity of rocks. *J. Chem. Eng. Dat*a. 51, 22–33.

Abu-Ajamieh, M. (1980). The Geothermal Resources of Zarqa Ma'in and Zara. NRA-Jordan, Amman-Jordan, pp. 82.

Anderson, M.P. (2005). Heat as a ground water tracer. *Ground water* 43, 951–968.

Arad, A., Bein, A. (1986). Saline-versus freshwater contribution to the thermal waters of the northern Jordan Rift Valley. *Israel. J. Hydrol.* 83, 49-66.

Arad, A., Kafri, U., Halics, L., Brenner, I. (1986). Genetic identification of the saline origins of groundwaters in Israel by means of minor elements. *Chem. Geol.* 54, 251-270.

Athy, L.F. (1930). Density, porosity and compaction of sedimentary rocks. *AAPG Bull* 14, 1-24.

Bajjali, W. (1994). Recharge and regional circulation of thermal groundwater in northern Jordan using isotop geochemistry. Ph.D. diss., university of Ottawa, Canada, pp. 211.

Bajjali, W., Clarck, I.D., Fritz, P. (1997). The artesian thermal ground waters of northern Jordan: insights into their recharge history and age. *J. Hydrol.* 192, 355-382.

Bandel, K., Khoury, H. (1981). Lithostratigraphy of the Triassic in Jordan. *Facies* 4, 1-26.

Bartov, Y. (1974). A Structural and Paleogeographic Study of the Central Sinai Faults and Domes. Ph.D. diss., Hebrew Univ., Jerusalem, pp. 143 (in Hebrew, English abstr.).

Bear, J. (1972). Dynamics of Fluids in Porous Media. American Elsevier Publishing Company Inc., New York.

Bear, J., and A.H.-D. Cheng. (2010). Modeling Groundwater Flow and Contaminant Transport, Springer, Dordrecht.

Bear, J., Bachmat, Y. (1991). Introduction to modeling of transport phenomena in porous media. Kluwer Publishers, Dordrecht.

Beck, J.L. (1972). Convection in a box of porous material saturated with fluid. *Phys. Fluids* 15, 1377–83.

Bein, A., Burg, A., Ben-Sabbath, J. (2003). GSI Rep. GSI/13/2001, Jerusalem, pp. 42 (in Hebrew).

Bein, A., Feinstein, S. (1988). Late Cenozoic thermal gradients in the Dead Sea transform system Basins. *J. Pet. Geol.* 11, 185-192.

Ben-Avraham, Z., Hänel, R., Villinger, H. (1978). Heat-flow through the Dead Sea rift. *Mar. Geol.* 28, 253–269.

Bender, F. (1974). Geology of Jordan. Gebmder Borntraeger, Berlin-Stuttgart.

Brew, G.E., Litak, R.K., Seber, D., Barazangi, M., Al-Imam, A., Sawaf, T. (1997). Basement depth and sedimentaray velocity structure in the Northern Arabian platform, Eastern Syria. *Geophys. J.Int.* 128, 617-631.

Brigaud, F., Vasseur, G. (1989). Mineralogy, porosity and fluid control on thermal conductivity of sedimentary rocks. *Geophys. J. Int.* 98, 525–542.

Bundschuh, J., Suárez, M.C. (2010). Introduction to the Numerical Modeling of Groundwater and

Geothermal Systems: Fundamentals of Mass, Energy and Solute Transport in Poroelastic Rocks. CRC Press/Balkema, Leiden.

Caltagirone, J.P., Meyer, G., Mojtabi, A. (1981). Structurations thermoconvectives tridimensionnelles dans une couche poreuse horizontale. *J. mécanique* 20, 219–232.

Čermák, V,. Rybach, L. (1982). thermal conductivity and specific heat of minerals and rocks, in : Angenheister G., (Ed.) Landolt-Börnstein: Numerical Data and Functional Relationships in Science and Technology, New Series, Gr. V (Geophysics and Space Research), Volume l a (Physical Properties of Rocks). Springer Verlag, Berlin-Heidelberg, pp. 305-343.

Clark, S.P., Jr. (1966). Thermal conductivity, In: Clark, S.P., Jr. (Ed.), Handbook of Physical Constants, revised ed, vol. 97. GSA Memoir, New York, pp. 459-482.

Clauser, C. (2006). Geothermal Energy, In: Heinloth, K., (Ed), Landolt-Börnstein, Gr.VIII: Advanced Materials and Technologies, Vol. 3: Energy Technologies, Subvol. C: Renewable Energies. Springer Verlag, Berlin-Heidelberg, pp. 493-604 (Pre print).

Clauser, C., Huenges, E. (1995). Thermal conductivity of rocks and minerals, In: Ahrens,T.J. (Ed.), A Handbook of Physical Constants: Rock Physics and Phase Relations, vol. 3. American Geophysical Union, Washington, pp. 105–126.

COMSOL AB. (2008). COMSOL Multiphysics, Earth Science Module User's Guide (Version 3.5a), Stockholm-Sweden.

COMSOL AB. (2011). COMSOL Multiphysics 4.2, Earth Science Module User's Guide (Version 4.2), Stockholm-Sweden.

Dafny, E., Burg, A., Gvirtzman, H. (2006). Deduction of groundwater flow regime in a basaltic aquifer using geochemical and isotopic data: The Golan Heights, Israel case study. *J. Hydrol.* 330, 506– 524.

Dafny, E., Gvirtzman, H., Burg, A., Fleischer, L. (2003). The Hydrogeology of the Golan Basalt Aquifer, Israel. *Isr. J. Earth Sci.* 52, 139-153.

De Marsily, G. (1986). Quantitative Hydrogeology. Academic Press, San Diego-California.

Diersch, H.-J.G. (2009). finite element subsurface flow and transport simulation system—user's manual/reference manual/white papers. Wasy, Berlin.

Diersch, H.-J.G., Kolditz, O. (2002). Variable-density flow and transport in porous media: approaches and challenges. Adv. *Water Resour.* 25, 899–944.

Drury, M.J., Jessop, A.M. (1983). The estimation of rock thermal conductivity from mineral content-An assessment of techniques. *Zbl. Geol. Paleont.* Teil I, H1/2, 35-48.

Eckstein, Y. (1976). The application of chemical geothermometers to aground waters in Israel; Proc. Int. congr. On thermal waters, geothermics and volcanisms of the Mediterranean area, oct. 1967, Athens, Greece, 2, 81-96.

Eckstein, Y., Maurath, G. (1995). Terrestrial heat-flow density and geothermal regime in Israel, in: Gupta, M.L., Yamano, M., (Eds.), Terrestrial Heat-flow and Geothermal Energy in Asia. Oxford & IBH, New Delhi, pp. 1–21.

Eckstein, Y., Simmons, G. (1978). Measurements and interpretation of terrestrial heat-flow in Israel. *Geothermics* 6, 117–142.

El-Naser, H. (1991). Groundwater resources of the deep aquifer systems in NW-Jordan: hydrogeological and hydro chemical quasi 3-dimentional modeling. *Hydrogeologie und umwelt* 3, 1-144.

Erickson, A.J., simmons, G., Ryan, W.B.F. (1977). Review of heat-flow data from the Mediterranean and Aegean Seas, in: Biju-Duval, B., and Montadert, L. (Eds.), Structural history of the Mediterranean Basins. Edition Technip, Paris, pp. 263-280.

ESCWA (U.N, Economic and Social Commission for Western Asia), Ministry of water and irrigation – Jordan, Ministry of irrigation-Syria. (1996). Investigation of the regional basalt aquifer system in Jordan and Syrian Arab Republic. Issued without formal editing, Amman, pp. 178.

Feinstein, S. (1985). Constraints on the thermal history of the Dead Sea Graben as revealed by a study of coal ranks in the Ami'az I, Zuk Tamrur 1 and Zohar 8 boreholes. International workshop on sedimentary basins along the Dead Sea Rift zones. Ramot-Israel, Abstr., pp. 17-18.

Fleischer, L. (2002). Stratigraphic table of Israel, outcrops and subsurface. geophysical institute of Israel, in: Hall J.K., Krasheninnikov, V.A., Hirsch, F., Benjamini, C., Flexer, A., (Eds.), Geological framework of the Levant, volume I: Cyprus and Syria. Historical Productions-Hall, Jerusalem, pp. 733.

Folkman, Y. (1980). Magnetic and gravity invastigations of the Dead Sea rift and the adjacent areas in northern Israel. *J. Geophys.* 48, 34-39.

Förster, A., Förster, H.-J., Masarweh, R., Masri, A., Tarawneh, K., DESERT Group. (2007). The surface heat-flow of the Arabian Shield in Jordan. *J. Asian Earth Sci.* 30, 271-284.

Förster, H.-J., Förster, A., Oberhänsli, R., Stromeyer, D. (2010). Lithospheric composition and thermal structure of the Arabian Shield in Jordan. *Tectonophysics* 481, 29–37.

Freund, R. (1965). A model of the structural development of Israel and adjacent areas since Upper Cretaceous times. *Geol. Mag.* 102, 189–205.

Freund, R. (1980). Creation processes of Hermon and Lebanon mountains. In: Shimda, A. (Ed.), Mt. Hermon: Nature and Landscape. Hakibbutz HaMeuhad, Tel-Aviv, pp. 28–32 (in Hebrew).

Freund, R., Garfunkel, Z., Zak, I., Goldberg, M., Wessbrod, T., Derin, B. (1970). The shear along the Dead Sea Rift. *Philos. Trans. R. Soc. Lond.* 267, 107-130.

Galaktionov, A.B. (1989). Map of identification of space images (and explanatory notes), scale 1:500,000. Syrian Petroleum Company, Damascus (unpublished).

Galanis, S.P., Sass, J.H., Munroe, R.J., Abu-Ajamieh, M. (1986). Heat-flow at Zerqa Ma'in and Zara and a geothermal reconnaissance of Jordan. USGS open-file rep. 86-631, California, pp. 110.

Garfunkel, Z., Zak, I., Freund, R. (1981). Active faulting in the Dead-Sea rift. *Tectonophysics* 80, 1–26.

Gilad, D. (1985). Hydrological model of the Hammat Gadder aquifer. Hydro rep. HYDRO/2/1985, Jerusalem, pp. 27 (in Hebrew).

Girdler, R.W., Evans, T.R. (1977). Red Sea heat-flow. Geophys. *J. of the royal astron. Soc.* 51, 245-251.

Heimann, A. (1990). The development of the Dead Sea Rift and its margins in Northern Israel in the Pliocene and Pleistocene. GSI rep. GSI/28/90, Jerusalem, pp. 83 (in Hebrew, English abstr.).

Hirsch, F., Fleischer, L., Roded, R., Rosensaft, M. (2002). The structural maps of Mount Hermon, Golan Heights and NE Jordan: stratigraphy and tectonics. GSI rep. GSI/19/2001, Jerusalem, pp. 29.

Hobler, M., Margane, A., Almomani, M., Subah, A. (2001). Groundwater resources of northern Jordan, vol-4: Contribution to the hydrogeology to the northern and central Jordan. By the BGR-WAJ technical corporation project, project no.89.2105.8, Amman, pp. 84.

Holzbecher, E. (1999). Modeling density-driven flow in porous media. Springer, Berlin.

Huenges, E. (2010). Geothermal Energy Systems – Exploration, Development, and Utilization (in chapter 5- Geothermal Reservoir Simulation). Wiley-VCH, Weinheim.

IAPWS. (2008). Revised Release on the IAPS Formulation 1985 for the Thermal Conductivity of Ordinary Water Substance. Int. Association for the Properties of Water and Steam. Berlin, pp. 23.

Israel meteorological service. (2011). Min and max Ground surface temperature at Avnei Eitan and Zemah measurements stations, from 1996-2005. Israel Meteorological Service, Beit Dagan. Available online: http://www.ims.gov.il/ims/Meteorologika/evaporation%20tub/daily%20data/

Kafri, U., Lang, B., Vulkan, U. (2000). Radon in groundwaters of northern Israel. *GSI curr. Res.* 12, 41-49.

Keller, G.V. (1977). The Geothermal Potential of Israel. Report submitted to the Institute for Petroleum Research and Geophysics.

Kenneth, S.P., Peiper C.J., Busey R.H. (1984). Thermodynamic Properties of Aqueous Sodium Chloride Solutions. *J. Phys. Chem. Ref. Data* 13, 1-102.

Kessler, A. (2002). GSI Tech Rep. TR-GSI/9/200, Jerusalem, pp. 47 (in Hebrew).

Kolditz, O. (2002). Computational methods in environmental fluid mechanics. Springer, Berlin.

Lamoreaux, P.E., Hughes, T.H., Memon, B.A. (1989). Hydrogeologic assessment, Figeh Spring, Damascus, Syria. *Environ. Geol. Water Sci.* 13, 73-127.

Lee, Y., Deming, D. (1998). Evaluation of thermal conductivity temperature correlations applied in terrestrial heat flow studies. *J Geophys Res.* 103, 2447–54.

Levitte, D., Eckstein, Y. (1978). Correlation between the silica concentration and the orifice temperature in the warm springs along the Jordan-dead Sea Rift Valley. *Geothermic.* 7, 1-8.

Levitte, D., Olshina, A. (1985). Isotherm and Geothermal Gradient Maps of Israel. GSI rep.GSI/60/85, Jerusalem, pp. 94.

Levitte, D., Olshina, A., Wachs, D. (1978). Geological and geophysical investigation in the Hammat Gadder hot Springs area. GSI rep. HYDRO/4/1978, Jerusalem, pp. 59.

Margane, A., Hobler, M., Almomani, M., Subah, A. (2002). Contribution to the hydrogeology to the northern and central Jordan. Geologisches Jahrbuch, Amman, Reihe C, Heft 68, pp. 52.

Mazor, E., Kaufman, A., Carmi, I. (1973). Hammat Gadder (Israel): Geochimestry of a mixed thermal spring complex. *J. Hydrol.* 18, 289-303.

Mazor, E., Levitte, D., Truesdell, A.H., Healy, J., Nissenbaum, A. (1980). Mixing models and ionic geothermometers applied to warm (up to 60 0C) springs: Jordan rift valley, Israel. *J. Hydrol.* 45, 1–19.

Mckenzie, D. (1978). Some remarks on the development of sedimentary Basins. *J. Earth and Planet. sci. Lett.* 40, 25-32.

Meiler, M. (2011). The deep geological structure of the Golan Heights and the evolution of the adjacent Dead Sea Fault System. Ph.D. diss., Tel-Aviv university, Tel-Aviv, pp. 143.

Meiler, M., Reshef, M., Shulman, H. (2011). Seismic depth-domain stratigraphic classification of the Golan Heights, central Dead Sea Fault. *Tectonophysics* 510, 354–369.

Mercer, J.W., Pinder, G.F. (1974). Finite element methods in flow problems, In: Oden, J.T. (Ed.) Finite Element Analysis of Hydrothermal Systems. University of Alabama Press, Proc. 1st Symp, Swansea, pp. 401–414.

Mero, P., Rosner, R. (1984). Mezar 2 and 3 water wells: summary of drilling. Water Planning for Israel rep. 01/84/68, Tel Aviv, pp. 17 (in Hebrew).

Michelson, H. (1981). Ein Said 1 Well-summery of activities. Water Planning for Israel rep. 01/81/93, Tel Aviv, pp. 14 (in Hebrew).

Michelson, H. (1982). Geological survey of the Golan Heights (with some remarks on exploration for hydrocarbons). Water Planning for Israel rep., Tel Aviv, pp. 48.

Michelson, H. (1983). Locating waters and steam in the southern Golan Heights. Water Planning for Israel rep., Tel Aviv, pp. 21 (in Hebrew).

Mor, D. (1993). A time-table for the Levant volcanic province, according to K-Ar dating in the Golan Heights, Israel. *J. Afr. Earth Sci.* 16, 223–234.

Myslil, V. (1988). Report on the evaluation of geothermal potential of Jordan. N.R.A. rep., Amman, pp. 21.

Nield, D.A. (1994). Estimation of an effective Rayleigh number for convection in a vertically inhomogeneous porous medium or clear fluid. *Int. J. Heat Fluid Flow* 15, 337–40.

Nield, D.A., Bejan, A. (2006). Convection in Porous Media, third Ed. Springer, New York.

NIST. (2010). Table 3 Compressed Water and Superheated Steam enthalpy, entropy, volume, density. NIST database. Available on line: http://www.nist.gov/srd/upload/NISTIR5078-Tab3.pdf

Palliser and Mckbbin, R. (1998a). A Model for Deep Geothermal Brines, II: Thermodynamic Properties – Density. *Transport in Porous Media* 33, 129–154.

Palliser, C., Mckbbin, R. (1998b). A Model for Deep Geothermal Brines, III: Thermodynamic Properties – Enthalpy and Viscosity. *Transport in Porous Media* 33, 155–171.

Philips, S.L., Igbene, A., Fair, J.A., Ozbek, H., Tavana, M. (1981). A technical data book for geothermal energy utilization. NTIS. DE81-029868. pp. 14.

Phillips, S.L., Ozbek, H., Silvester, L.F. (1983). Density of sodium chloride solutions at high temperatures and pressures. NTIS. DE84-004883. pp. 51.

Phillips, O.M. (2009). Geological Fluid Dynamics: Sub-surface Flow and Reactions, first ed. Cambridge University Press, Cambridge.

Picard, L. (1943). Structure and evolution of Palestine. *Geol. Dep. Heb. Univ. Bull.* 4, 1–134.

Ponikarov, V.P. (1967). The Geology of Syria. Explanatory Notes on the Geological Map of Syria. Part I, Stratigraphy, Igneous Rocks and Tectonics. Ministry of Industry, Damascus, p. 229.

Powell, W.G., Chapman, D.S., Balling, N., Beck, A.E. (1988). Continental heat-flow density, In: Haenel, R., Rybach, L., Stegena, L., (Eds.), Handbook of Terrestrial Heat-Flow Density Determination. Kluwer, Dordrecht, pp. 167–222.

Perrochet, P., Tacher, L. (1997). Mathematical modeling of hydro-thermal processes in Mururoa Atoll. Research Report GEOLEP-EPFLDGC, Univ. Lausanne, Switzerland.

Quennell, A.M. (1958). The structure and the geomorphic evolution of the Dead Sea rift. *Q. J. Geol. Soc. London* 64, 1-24

Razvalyaev, A.V., Kazmin, V.G., Galaktionov, A.B. (2005). Volcanism, In: Krasheninnikov, V.A., Hall J.K., Hirsch, F., Benjamini, C., Flexer, A., (Eds.), Geological framework of the Levant, volume I: Cyprus and Syria. Historical Productions-Hall, Jerusalem, pp. 417-463.

Rotstein, Y., Goldberg, S., Klang, A. (1978). Geothermal Project: Electrical Resistivity Survey in the Northeastern Golan Heights. Inst. Pet. Res. Geophys. Rep. GE/380/77, Holon, pp. 10.

Rotstein,Y., Klang, A., Levanon, A. (1977). Geothermal Project: Electrical Resistivity Surveys of Bet Shean – Jordan Valleys and Lake Kinneret. Inst. Pet. Res. Geophys. Rep. GT/149/74 (3), Holon, pp. 28.

Rybach, L. (1988). Determination of heat production rate, In: Haenel, R., Rybach, L., Stegena, L., (Eds.), Handbook of Terrestrial Heat-Flow Density Determination. Kluwer, Dordrecht, pp. 125–143.

Schmoker, J.W., Halley, R.B. (1982). Carbonate porosity versus depth: a predictable relation for south Florida. *Am. Assoc. Pter. Geol. Bull.* 66, 2561-2570.

Sekiguchi, K. (1984). A method for determining terrestrial heat-flow in oil basins areas. *Tectonophysics* 103, 67-69.

Sengers, J.V.,Watson, J.T.R. (1986). Improved international formulations for the viscosity and thermal conductivity of water substance. *J. Phys. Chem. Ref. Data* 15, 1291–1314.

Shalev, E., Levitte, D., Gabay, R., Zemach, E. (2008). Assessment of Geothermal Resources in Israel. GSI rep. GSI /29/ 2008, Jerusalem, pp. 26.

Sneh, A., Bartov, Y., Rosensaft, M., Weissbrod, T. (1998). Geological Map of Israel, 1:200,000. GSI rep. GSI/8/2001, Jerusalem, 4 sheets.

Somerton, W.H. (1992). Thermal properties and temperature related behavior of rock/fluid system. Elsevier, New York.

Sorek., S., Pinder, G.F. (1999). Survey of computer codes and case histories, in: Bear, J., Cheng, A. H.-D., Sorek, S., Ouazar, D., and Herrera, I., (Eds.), Seawater Intrusion in Coastal Aquifers -Concepts, Methods and Practices. Kluwer Academic, Dordrecht.

S.P.C. (Syrian Petroleum Company). (1986). Depth scheme map of the crystalline basement scale 1:500,000. (Compiled by T.Sawaf). Damascus (unpublished).

Starinsky, A., Kats, A., Levite, D. (1979). Temperature-composition-depth relation in rift Valley hot springs Hamat Gadder, northern Israel. *Chem. Geol.* 27, 233-244.

Straus, J.M. (1974). Large amplitude convection in porous media. *J. Fluid Mech.* 64, 51–63.

Straus, J.M., Schubert, G. (1977). Thermal convection of water in a porous medium: effects of temperature and pressure dependent thermodynamic and transport processes. *Z Geophys. Res.* 82, 325-333.

TAHAL. (1989). Hydrogeological and hydrometeorological model of the Yarmouk Basin. Water Planning for Israel rep. 01/89/62, Tel Aviv, pp. 53 (in Hebrew).

Truesdell, A. (1979). Report on the chemistry and geothermal energy possibilities of the Zarqa Ma'in-Zara hot Springs, Jordan. USGS rep. California, pp. 28.

Turcotte, D.L., Schubert, G. (2002). Geodynamics. Cambridge University Press., Cambridge.

Van der Kamp, G., Bachu, S. (1989). Use of dimensional analysis in the study of thermal effects of various hydrogeological regimes, In: Beck, A.E., Garven, G., Stegena, L., (Eds.), Hydrogeological Regimes and Their Subsurface Thermal Effects. Geophys. Monogr. 47, IUGG. 2, AGU, Washington, pp. 23–28.

Wagnera, W., Pruß, A. (2002). The IAPWS Formulation 1995 for the Thermodynamic Properties of Ordinary Water Substance for General and Scientific Use. *J. Phys. Chem. Ref. Data* 31, 387-484.

Walley, C.D. (1988). A Braided Strike-Slip Model for the Northern Continuation of the Dead-Sea Fault and Its Implications for Levantine Tectonics. *Tectonophysics* 145, 63-72.

Walley, C.D. (1998). Some outstanding issues in the geology of Lebanon and their importance in the tectonic evolution of the Levantine region. *Tectonophysics* 298, 37-62.

Watson, J.T.R., Basu, R.S., Sengers, J.V. (1980). An improved representative eqution for the dynamic viscosity of water substance. *J. Phys. Chem. Ref. Data* 9, 1255-1290.

Woodside, W., Messmer, J.H. (1961). Thermal conductivity of porous media. I. Unconsolidated sands. I1 Consolidated rocks. *J. appl. Phys.* 32, 1688–1706.

Zoth, G., and Haenel, R. (1988). Appendix, In: Haenel, R., Rybach, L., Stegena, L., (Eds.), Handbook of Terrestrial Heat-Flow Density Determination. Kluwer, Dordrecht, pp. 167–222.

8. Appendix- pure water and steam properties

Table 11. H_2O density ρ (kg/m^3) at different pressure p and temperature T conditions; modified after NIST (2010).

P (Mpa) T (°C)	25	50	75	100	125	150	175	200
0.1	997.05	988.03	974.84	0.589 67	0.550 28	0.516 36	0.486 64	0.460 31
0.5	997.23	988.21	975.02	958.54	939.16	917.02	2.5033	2.3528
1	997.45	988.43	975.24	958.77	939.42	917.31	892.35	4.8539
2.5	998.13	989.08	975.91	959.47	940.18	918.15	893.32	865.38
5	999.25	990.16	977.01	960.63	941.44	919.56	894.93	867.26
7.5	1000.36	991.24	978.1	961.79	942.69	920.95	896.51	869.11
10	1001.47	992.31	979.19	962.93	943.93	922.32	898.07	870.94
15	1003.66	994.43	981.35	965.2	946.38	925.03	901.14	874.5
20	1005.84	996.53	983.48	967.44	948.79	927.69	904.14	877.97
25	1007.99	998.61	985.59	969.65	951.16	930.3	907.07	881.33
30	1010.12	1000.67	987.67	971.82	953.5	932.86	909.94	884.62
35	1012.23	1002.7	989.73	973.97	955.8	935.38	912.75	887.82
40	1014.32	1004.72	991.76	976.1	958.07	937.86	915.51	890.94
45	1016.39	1006.71	993.77	978.2	960.31	940.3	918.21	893.99

Table 12. H_2O viscosity μ (10^6 pa*s) at different pressure p and temperature T conditions; modified after Sengers and Watson (1986).

p (Mpa) T (°C)	25	50	75	100	150	200
0.1	890.9	547.1	377.3	12.42	14.29	16.26
0.5	891.2	546.7	378	281.7	182.3	16.05
1	891.1	546.8	378.2	281.9	182.4	15.92
2.5	890.8	547.1	378.5	282.3	182.8	134.6
5	890.3	547.7	379.2	283.1	183.4	135.2
7.5	889.8	548.3	379.8	283.8	184.1	135.9
10	889.4	548.7	380.4	284.7	184.7	136.4
12.5	889.1	549.1	381	285.3	185.3	137
15	888.7	549.5	381.6	286	186	137.6
17.5	888.5	550	382.3	286.7	186.6	138.2
20	888.2	550.4	382.9	287.4	187.3	138.8
22.5	887.9	550.9	383.5	288	187.9	139.4
25	887.6	551.3	384.2	288.7	189.5	140
27.5	887.4	551.8	384.8	289.4	189.1	140.6
30	887.2	552.3	385.5	290	189.8	141.2
35	886.8	553.3	386.7	291.4	191	142.3
40	886.6	554.3	388	292.7	192.2	143.5
45	886.5	555.3	389.3	294	193.4	144.6

Table 13. H_2O specific heat capacities c_v and c_p, at different pressure p and temperature T conditions, upper value is c_v (j/l°C) and lower c_p (j/kg°C); modified after IAPWS (2002).

p (Mpa) / T (K)	295	325	350	375	420	580
0.1	4.1498 4.1829	4.0172 4.1819	3.8894 4.1945	1.5479 2.0686	1.4968 1.9868	1.5484 2.0160
0.5	4.1484 4.1817	4.0161 4.1810	3.8886 4.1936	3.7580 4.2169	3.5375 4.2988	1.5741 2.0674
1	4.1466 4.1802	4.0149 4.1798	3.8876 4.1925	3.7572 4.2158	3.5370 4.2972	1.6090 2.1380
5	4.1329 4.1683	4.0050 4.1708	3.8799 4.1839	3.7512 4.2066	3.5331 4.2848	2.0178 3.0649
10	4.1161 4.1539	3.9928 4.1599	3.8705 4.1734	3.7438 4.1955	3.5283 4.2699	3.0445 5.9333
15	4.0998 4.1401	3.9809 4.1493	3.8612 4.1632	3.7365 4.1847	3.5236 4.2556	3.0304 5.6647
20	4.0840 4.1268	3.9693 4.1389	3.8520 4.1533	3.7294 4.1742	3.5189 4.2419	3.0201 5.4654
25	4.0686 4.1140	3.9579 4.1289	3.8431 4.1437	3.7223 4.1641	3.5143 4.2287	3.0122 5.3093
30	4.0537 4.1017	3.9468 4.1192	3.8343 4.1343	3.7154 4.1542	3.5098 4.2159	3.0059 5.1825
40	4.0250 4.0784	3.9252 4.1005	3.8172 4.1162	3.7018 4.1352	3.5009 4.1918	2.9966 4.9863
50	3.9860 4.0622	3.9046 4.0829	3.8007 4.0991	3.6887 4.1172	3.4922 4.1692	2.9899 4.8392

Table 14. H_2O thermal conductivity λ_f (W/m°C) at different pressure p and temperature T conditions; modified after IAPWS (2008).

p (Mpa) / T (°C)	25	50	75	100	150	0
0.1	610	643	664	25	28.8	33.3
0.5	610	643	664	680	688	34.1
1	611	643	666	681	689	35.9
2.5	611	644	666	682	690	668
5	613	645	668	683	691	671
7.5	614	647	669	685	694	673
10	615	648	669	686	695	675
15	617	650	673	689	700	680
20	619	653	676	691	703	684
25	621	655	679	694	707	689
30	623	658	681	697	710	692
35	625	660	684	700	714	696
40	626	662	686	702	717	700
45	629	664	690	705	721	704

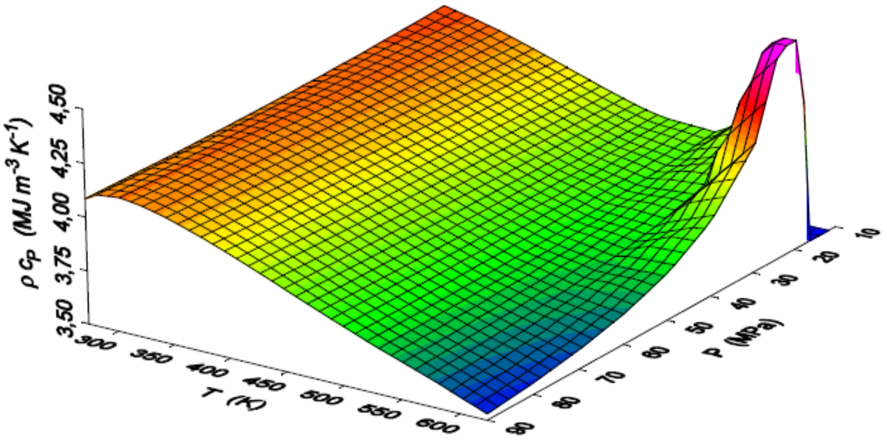

Figure 31. H_2O specific heat capacity c_p vs. pressure *p* and temperature *T* conditions (Clauser, 2006).

תקציר

אנומליה גיאותרמית רדודה, המצויה בחלקו התחתון של אגן הירמוך, בצפון מדינת ישראל וירדן, מאופיינת בשפיעה ניכרת של מי תהום חמים במעיינות ובקידוחים. אנליזה נומרית דו-ממדית, הכוללת חישובי מאזן של זרימת מי תהום ומעבר חום, נעשתה על האגנים הגיאו-הידרולוגיים במרחב גולן-עג'לון. תוצאות האנליזה הנומרית לאור נתוני השדה מצביעות על קיומו של מקור חום גיאותרמי חריג מתחת לרמת הגולן ועל רכיב זרימה מונע גרביטציה שנתיב זרימתו עמוק (~3 ק"מ). מקורו של רכיב זרימה זה במורדות החרמון, ומוצאו במעיינות נהר הירמוך התחתון. ספיקתו מוערכת במלמ"ק ספורים בשנה, מתוך כלל 45.5 המלמ"ק של הספיקה ההיסטורית של המעיינות.

רכיב זרימה והסעה זה מסיע חום ניכר מעומק רב ומשפיע על משרעת הטמפרטורה באגן. חלק ניכר משטף החום הגבוה נובע במעיינות הירמוך, והוא גם הגורם להעדר ביטוי תרמי רדוד מתחת לרמת הגולן. רכיב זה הוא מקור משני בלבד למעיינות הירמוך, שכן הם ניזונים בעיקר ממי תהום שמגיעים מדרום, מרכס עג'לון, שם הם זורמים באקוויפרים הרדודים של עמן ושל ואדי סיר, כפי שכבר נטען במחקרים הידרוגיאולוגיים. תוצאות האנליזה הנומרית מראות ששטף החום הממוצע מעומק הקרום שמתחת לרמת הגולן הוא 100 מיליוואט למ"ר, כך שלמעשה אנומליית החום הרדודה היא ביטוי לאנומליה גיאותרמית מעומק הקרום.

מתווים הידרותרמלים אפשריים נוספים הם מקור חום ממזרח לרמת הגולן, ממזרח החורן, או הסעה נרחבת ועמוקה של חום המנקזת גם שטחים נרחבים ממזרח (בשטח כולל של כ-3600 קמ"ר) בעלי שטף חום אזורי נורמלי (50 מיליוואט למ"ר). אך חוסר בנתונים גיאולוגיים, הידרולוגיים ותרמיים בסיסיים מאזור זה מונע בחינה מעמיקה של אפשרויות אלו.

מכלול התנאים יוצאי הדופן בתת-הקרקע שמתחת לאגן הירמוך התחתון, קרי טמפרטורה גבוהה בעומק רדוד (~130^0C בעומק של כ-3 ק"מ) ומאגר מי תהום גדול וארטזי, מעודדים המשך בחינת התאמתו של אזור זה להפקת חשמל באמצעות תחנה גיאותרמית. הפקה שכזו יכולה גם להתבצע בתחום הקו הירוק.

ניתוח המערכת הגיאותרמית במרחב עג'לון-גולן מצביעה באופן חד-משמעי על קיומה של הסעת חום עמוקה משטח נרחב באמצעות זרימת מי תהום, המהווה רק מרכיב משני מכלל זרימת מי התהום במערכת. וכפי שכבר הודגם במחקרים קודמים, ניתוח תרמי הוא עוקב (tracer) יעיל לזרימת מי התהום.

לאור תוצאות המודל הנומרי, נמצא כי מספר חסר המימד פקלה, Pe, הגיאותרמי הוא אמצעי טוב להערכה גסה של יחס מנגנוני מעבר החום- הסעה וההולכה. המסקנה הזאת נכונה כל עוד חישובו אינו מסתמך על הערכת המוליכות ההידראולית. לעומת זאת, מספר חסר המימד- ריילי-דרסי, Ra, נמצא בלתי מתאים להערכה גסה של משטר הקונבקציה באגן, אף על פי שמשטרי הקונבקציה המתוארים בספרות זוהו בתרחישי המודל השונים.

האנליזה מביאה למסקנה כי תוכנת האלמנטים הסופיים - COMSOL multyphysics היא בלתי מתאימה לאנליזה נומרית של מערכות גיאותרמיות בקנה מידה אגני. לעומתה FEFLOW הדגימה יציבות ועקביות בפיתרון במהלך כל שלבי העבודה.

משרד האנרגיה והמים

המכון הגיאולוגי

שטף החום העמוק והמתווה ההידרותרמלי באגנים ההידרולוגיים במרחב גולן-עג'לון

רועי רודד

עבודה זו הוגשה כחיבור לקבלת תואר ״מגיסטר בהנדסה״ לסינאט אוניברסיטת בן גוריון בנגב

העבודה נעשתה בהדרכתם של:

דר׳ שלו אייל, המכון הגיאולוגי, ירושלים.

פרופ׳ קטושבסקי דוד, היחידה להנדסה סביבתית, אוניברסיטת בן גוריון בנגב.

דוח מס׳ GSI/22/2012

ירושלים, אב תשע״ב, יולי 2012